Astronomy Reports, Vol. 47, No. 3, 2003, pp. 169–175. Translated from Astronomicheskiĭ Zhurnal, Vol. 80, No. 3, 2003, pp. 195–201.

Identifying Compact Moving Groups Based on Stellar Kinematics Data

A. A. Myullyari[1], C. Flynn[1], and V. V. Orlov[2]

[1] *Tuorla Observatory, Turku University, Vaäisäläntie 20, FIN-21500, Piikkiö, Finland*

[2] *Astronomical Institute, St. Petersburg State University, Universitetskiĭ pr. 28, St. Petersburg, Peterhof, 198504 Russia*

Received January 28, 2002; in final form, October 10, 2002

Abstract—We investigate the possibility of identifying substructures in velocity space in three well-known stellar streams (the Hyades, the Pleiades, and Ursa Major) using a cluster-analysis method (the maximum-density method). Only compact groups in velocity space with radii no greater than 5 km/s and containing at least 10 members were considered. As an example, we analyzed a sample of 5377 stars from the HIPPARCOS catalog with known radial velocities located within 75 pc of the Sun. We identified a total of 24 groups of stars. Monte Carlo simulations show that most (about 80%) of these groups could be the results of Poisson noise and observational errors. Bona fide identification (at a significance level greater than 90%) of compact moving groups based on kinematic data requires higher accuracy of the stellar spatial velocities (with errors no greater than 1–2 km/s in each component).

1. INTRODUCTION

Moving stellar groups have been known for more than one and a half centuries, since the pioneering works of Mädler [1] and Proctor [2]. Despite the rather low accuracy of the proper motions determined in early papers, three stellar streams—the Hyades, the Pleiades, and Ursa Major (the Sirius group)—were identified. These streams are kinematically associated with known open star clusters. The authors of subsequent studies found a number of other moving stellar groups in the solar neighborhood. Important progress in the field has been achieved since the publication of the Hipparcos star catalogue [3]. A number of authors [4–7] have searched for substructures in velocity space.

As a rule, moving groups are identified using methods based on:

(1) proper-motion and/or radial-velocity data,

(2) spatial velocities of stars, or

(3) proper-motion and parallax data.

Methods of the first type include the classical method of radiants (see, e.g., [8]) and the method of Ratnatunga [9]. In the former, points with a greater than average number of intersections of stellar proper-motion vectors are identified. In the latter, the radial velocities and position angles of the proper-motion vectors are transformed into two new parameters that both vanish for moving-group members. This approach enables searches for extended groups of stars with common proper motions.

Methods of the second type (see, e.g., [5, 10–13]) have been used to analyze the distribution of stars in velocity space. To identify probable nonrandom groupings of stars, the observed distribution of residual stellar velocities is compared to a random distribution (usually a superposition of three independent Gaussians). Groupings are then searched for using the method of "principal stars" [10, 11], cluster analyses [11], nonparametric (kernel) density estimators [12], or wavelet analyses [5, 13].

In methods of the third type [4, 6] the three-dimensional velocity distribution is reconstructed from parallax and proper-motion data. Dehnen [4] uses the maximum likelihood method to this end. Chereul *et al.* [6] developed the so-called "spaghetti" method, in which each star is assigned a cylinder ("piece of spaghetti") in velocity space. The spaghetti is orthogonal to the tangential-velocity vector and parallel to the line of sight. The thickness of the spaghetti depends on the errors in the astrometric data. The spaghettis corresponding to stars having

Table 1. Velocities of the centroids of known moving clusters (in km/s)

Name of the group	U	V	W
Pleiades	−7	−25	−6
Hyades	−42	−20	−9
Ursa Major	+11	+2	−8

1063-7729/03/4703-0169$24.00

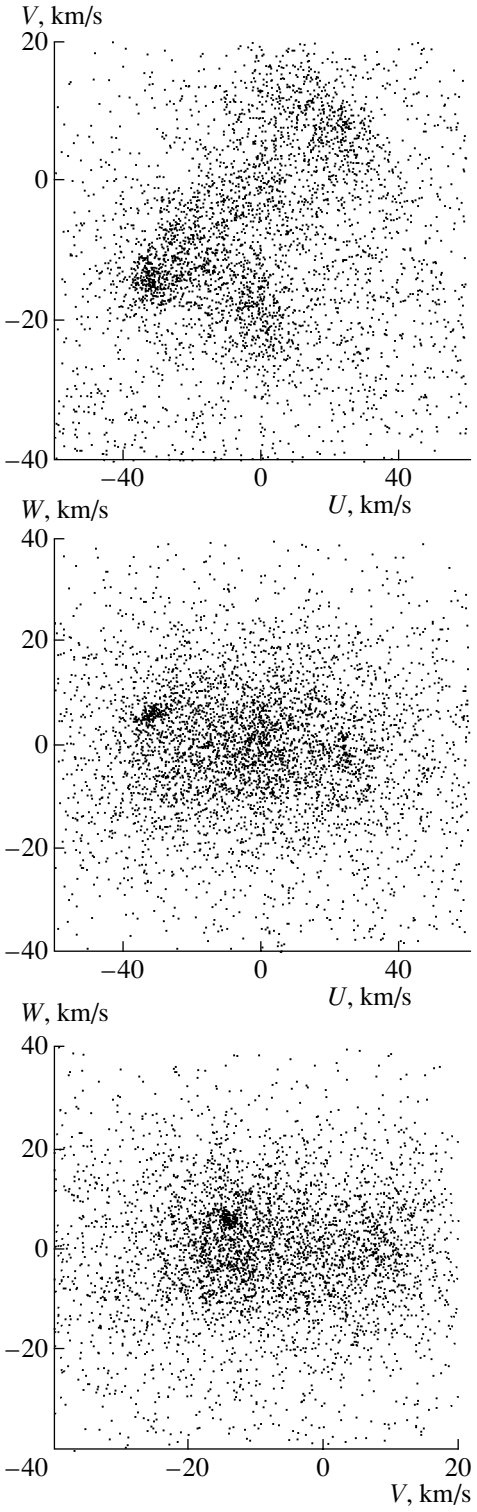

Fig. 1. Distribution of the sample stars in velocity space.

the same spatial velocities should all cross at one point, which is the centroid of the group.

All the above methods can be used to search for either group radiants on the celestial sphere or group centroids in the three-dimensional velocity space.

Table 1 summarizes the data on the three most well-known moving groups in the solar neighborhood (the Pleiades, the Hyades, and Ursa Major) from [12]. Similar centroid velocities have been obtained in other studies. Here, we use a heliocentric coordinate system with the U, V, and W axes pointing toward the Galactic center, in the direction of the Galactic rotation, and toward the North Galactic Pole, respectively. The results obtained for other moving groups in different studies do not agree as nicely, and can differ rather strongly in some cases. These discrepancies must be due to the different observational data and different methods used to identify the groups.

In this paper, we analyze the distribution of spatial velocities of nearby stars in order to identify moving groups. Section 2 describes the method used to identify groups and presents the parameters of the groupings that are found. In Section 3, we use Monte Carlo simulations to analyze the dependence of the reliability of the identification on the accuracy of the stellar spatial velocities and the richness of the group. Section 4 discusses the results.

2. METHOD

We use the data of the HIPPARCOS catalog [3] for stars with known radial velocities within $d = 75$ pc of the Sun. We chose this distance d as a compromise between the required sample size (decreasing d substantially decreases the number of stars and increases the errors due to the small sample size) and the required accuracy of the data (increasing d decreases the accuracy of the derived tangential velocities of the stars, since the relative parallax and proper-motion errors increase with heliocentric distance). The solar neighborhood considered contains a total of 5377 stars in the catalog [3] with known spatial velocities. We supplement this sample with stars from the Hipparcos Input Catalog, whose radial velocities are listed in [14, 15].

Figure 1 shows the distribution of the components of the stellar velocity vectors projected onto the UV, UW, and VW planes. The coordinate origin is located at the point corresponding to the local centroid. We adopted for the solar motion relative to the local centroid the components $U_\odot = 10$, $V_\odot = 5$, and $W_\odot = 7$ km/s [16]. We can see in Fig. 1 three large stellar streams that correspond approximately to the Hyades, the Pleiades, and Ursa Major streams (Table 1). These streams are especially conspicuous in the UV projection.

A number of authors have pointed out substructures in these streams (see, e.g., [17], [5] and references therein). Here, we search for compact stellar

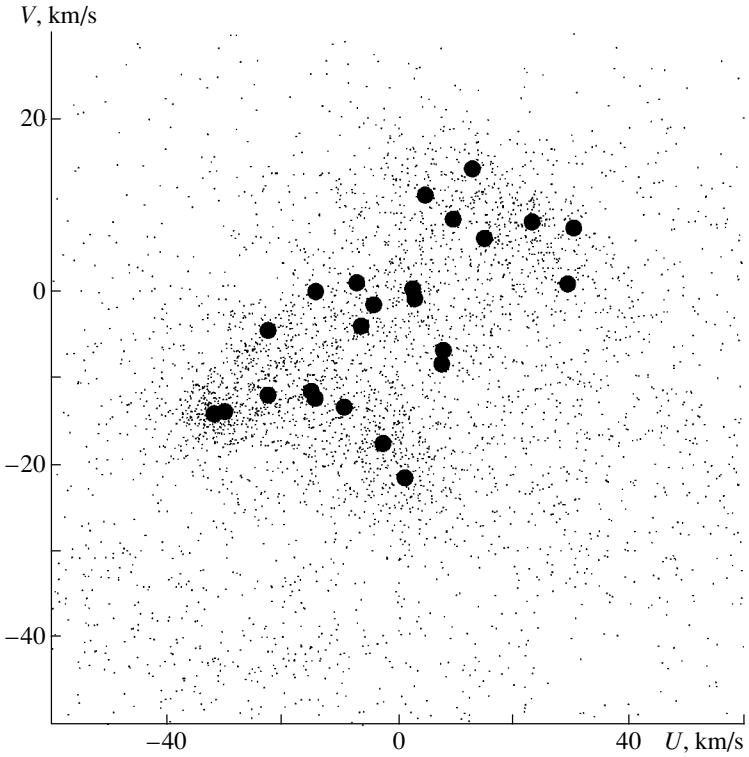

Fig. 2. Locations of the 24 groups (circles) identified projected onto the UV plane.

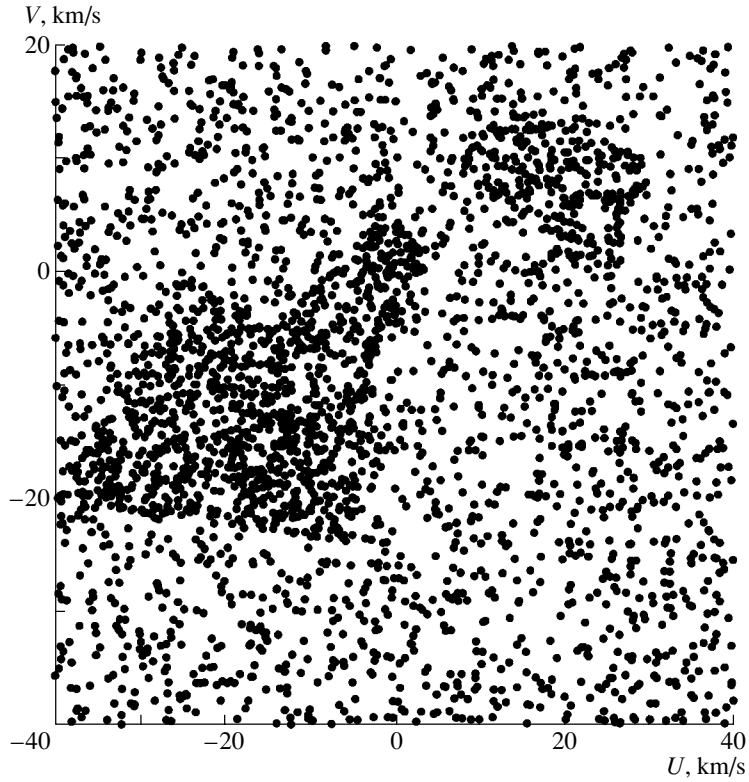

Fig. 3. Example of a simulated distribution of stars in the UV plane: three streams superimposed in a uniform field. The bounds of the streams are shown by the tetragons.

Table 2. List of identified moving groups

No.	U_c	V_c	W_c	n	Chereul *et al.* [5]			
1	−42	−18	−1	120	−83	−18	−2	Hyades Ocl
2	14	3	−8	45	12	1	−8	Sirius Scl
3	−12	−22	−6	18	−12	−22	−5	Pleiades Scl
4	−72	−17	−9	26	−33	−15	−6	Hyades Scl
5	−25	−16	−3	12	−21	−14	−5	IC 4391 Scl
6	−19	−26	−14	19		–		
7	−16	−9	−1	12		–		
8	−69	−49	−14	13		–		
9	−24	−17	−11	10	−27	−18	−5	2–7
10	−7	−6	−14	25	−8	−4	−13	1–34
11	0	5	−3	14	1	3	−4	New Scl (4)
12	−14	−6	−7	61	−13	−8	−9	Cen–Crux
13	−32	−9	−13	10	−33	−12	−9	Hyades Scl (3)
14	−7	−5	−9	25		–		
29	3	9	1	13	6	6	0	New Scl (5)
16	−19	−38	−5	12	−19	−19	−7	1–11
17	−54	−5	−6	92		–		
18	−5	6	1	14		–		
49	5	1	−15	10	3	−1	−15	1–87
20	−67	−4	−65	02		–		
21	−2	−12	−9	10		–		
22	19	−4	−16	13	20	−3	−16	2–33
23	21	2	−7	11		–		
24	−2	−13	−3	10	−3	−11	−5	2–13

Table 3. Efficiency of the identification of groups

l	σ, km/s	$\overline{m}$	σ_m	Efficiency, %
30	6	29.6	3.2	102 ± 0
	3	30.0	3.5	68 ± 13
	5	30.6	3.8	21 ± 12
50	1	10.7	0.8	141 ± 0
	3	25.4	3.4	87 ± 11
	5	30.8	3.4	27 ± 14

groups in UVW space and estimate the probability that they represent real groups.

To locate moving groups in velocity space, we performed a hierarchical cluster analysis based on the "maximum density" method [18], using the corresponding procedure of the SAS system for Windows V8.1. We chose the version of this method that uses kernel density estimates, with the smoothing parameter $R = 2.5$ km/s. This R corresponds approximately to the typical errors in the spatial velocity. Test computations performed with $R = 2$ and $R = 3$ km/s showed that small variations of R do not significantly effect the results obtained. Below, we use the term "cluster" in the sense usually adopted in cluster analysis.

We give a list of compact moving groups with radii no greater than $r_{\max} = 5$ km/s containing no fewer than $n_{\min} = 10$ stars. In principle, the adopted method enables the identification of clusters of objects on any scale lengths, and our choice of $r_{\max}$ is determined by the velocity errors, which are usually several km/s, and the sizes of streams, which reach several tens of km/s.

In the clustering process, we identify every cluster containing at least $n_{\min}$ objects. We consider a cluster to be a moving group if it is identified one step before either (1) the radius of the cluster exceeds $r_{\max}$ or (2) the cluster merges with another cluster.

We identified a total of 24 moving groups in this way. The data for these groups are summarized in Table 2, arranged in order of their identification. Figure 2 shows the locations of the group centroids projected onto the UV plane in a coordinate system fixed to the local centroid. The groups identified are located mainly within the three large streams.

Table 2 lists the heliocentric velocities U_c, V_c, and W_c of the group centroid and the number of objects n in the group. The last columns give the heliocentric velocities and names of groups that have spatial motions similar to our groups identified by Chereul *et al.* [5] using wavelet analysis. Fifteen of our 24 groups have counterparts in [5], indicating that the results of the two studies agree fairly well. The discrepancies may be associated with the different samples considered and the different methods used to identify the groups. In the next section, we show that some groups are probably not real formations. Half of the groups are likely chance structures, although the exact fraction of chance groupings is difficult to estimate.

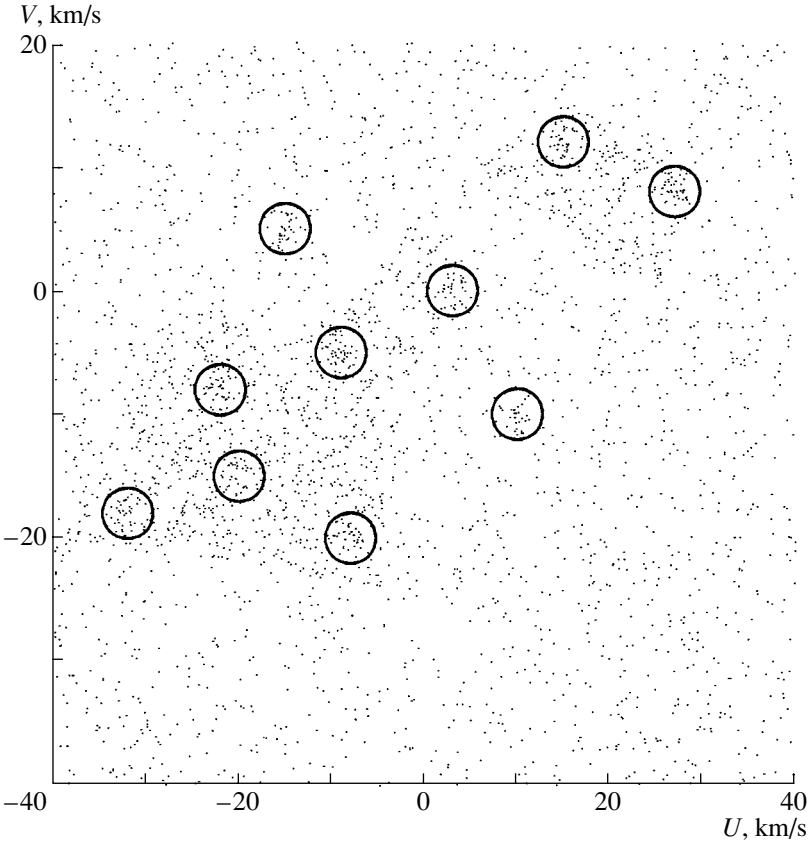

Fig. 4. Example of several moving groups artificially introduced into a simulated sample of stars. Groups are marked by circles.

3. MONTE CARLO MODELS

The 24 moving groups we have identified could include both real physical groups whose members have a common origin (joint formation) or are dynamically related (e.g., capture into the neighborhood of a periodic orbit) and chance groupings (e.g., due to the Poisson noise or observational errors). We used Monte Carlo simulations to estimate the number of such chance groupings.

It is evident from Fig. 2 that all the groups identified are located in the region $-40 \le U \le 40$, $-40 \le V \le 20$, $-20 \le W \le 20$ km/s relative to the local centroid. This region contains a total of 3148 sample stars. Of these, about 1000 stars belong to the Hyades, Pleiades, and Ursa Major streams.

Let us now consider the following simplified model. We have in the UV plane three uniform stellar streams superimposed on a uniform field. In the UV plane, each stream is approximated by a tetragon. The distribution of the W components of the stars in the streams and of the field stars are described by truncated normal distributions with means and dispersions equal to the corresponding quantities inferred from observations. To match the simulated and observed distributions, we generate 2150 field stars and 1000 stars belonging to streams. Figure 3 shows an example of such a simulated distribution.

We generated a total of 100 simulated samples and determined the number m of moving groups for each sample using the same algorithm that was applied to the observed sample (see Section 2). This number usually lay in the interval $22 \le m \le 40$, and its mean and standard deviation were $\bar{m} = 30.5$ and 3.5, respectively. The number of groups identified using the observational data ($m = 24$) is somewhat smaller than this mean. The probability of a chance realization of this or a smaller m is fairly low (several per cent). We therefore conclude that the distribution of stars in the streams may be nonuniform.

To test the efficiency of our method for identifying moving groups, we performed an additional set of Monte Carlo simulations. We used the same model and added $k = 10$ moving groups, each consisting of l stars. We superimposed eight groups on three streams, and put two groups within a small distance from streams (Fig. 4). We decreased the number of field and stream stars so as to preserve the total sample size. We assumed that the distribution within each group had the form of a superposition of three independent normal velocity distributions with one-dimensional standard deviations σ along each com-

ponent. We used the parameter values $l = 30, 50$ stars and $\sigma = 1, 3, 5$ km/s.

We considered each additional group to be identified if the cluster analysis yielded a group of stars with its centroid located within $r_{\rm crit} = 2$–3 km/s of the centroid of this group. Greater $r_{\rm crit}$ values increase the number of false identifications, whereas smaller $r_{\rm crit}$ values strongly decrease the efficiency with which groups are identified.

The results of numerical simulations for 100 samples with $r_{\rm crit} = 3$ km/s are summarized in Table 3. The first two columns give the values of the parameters l and σ. The next two columns give the mean number $\bar{\mu}$ of additionally identified groups and the standard deviation σ_μ of this number (contamination of the sample of identified groups). The last column gives the efficiency of group identification in percents.

As expected, rich compact groups with $l = 50$ and $\sigma = 1$ km/s are always confidently identified, and the number of false groups (the Poisson noise) is small in this case. Less rich but still compact groups ($l = 30$ and $\sigma = 1$ km/s) are also fairly confidently identified, although the number of false groupings increases. Sparser groupings ($\sigma = 3$ km/s) can still be identified relatively confidently, but the Poisson noise becomes rather strong. The identification of widely spaced groups ($\sigma = 5$ km/s) is very uncertain.

Note that only groups with low internal velocity dispersions can be confidently identified, and the observational data must have a high accuracy (the errors of the spatial velocity components should not exceed 1 km/s). Note also the decrease in the number of false identifications among rich groups ($l = 50$) when the additional groups are more compact.

4. DISCUSSION AND CONCLUSIONS

Thus, the maximum-density method of hierarchical cluster analysis applied to stars within 75 pc of the Sun yielded a total of 24 compact groups with radii no greater than 5 km/s in U, V, W velocity space, each containing at least 10 members. More than half of these groups have counterparts among groups identified by Chereul *et al.* [5] using wavelet analysis.

This raises the question of how real these 24 groups are. The Monte Carlo simulations described in Section 3 suggest that approximately half of these identifications may be chance groupings.

We also considered the identifiability of groups, and requirements for the accuracy of the observational data. Our analysis leads us to conclude that

(1) Groups must be sufficiently compact (with one-dimensional velocity dispersion no greater than 2 km/s);

(2) Groups must be sufficiently rich (containing at least several dozen members);

(3) The errors of the spatial velocity components must be sufficiently small (no greater than 2 km/s).

Of all the groups we have identified, only three (those listed in the first three rows of Table 2) appear to satisfy these criteria and are likely not to be chance systems. The future space projects DIVA and GAIA are promising sources of data for identifying poorer and sparser groups of stars.

5. ACKNOWLEDGMENTS

We are grateful to the Academy of Sciences of Finland for supporting this project. We also thank Johan Holmberg for providing the sample of HIPPARCOS stars with known spatial velocities and Ero Korpelainen for numerous fruitful discussions of cluster analysis methods. V. V. Orlov acknowledges financial support from the Ministry of Industry and Education of the Russian Federation (grant no. 00-15-96775 in program "Leading Scientific Schools"). We also thank St. Petersburg State University and Turku University for financial support in the framework of an Agreement on Research Cooperation between the two universities.

REFERENCES

1. J. H. Mädler, *Die Centralsonne* (Dorpat, 1846).
2. R. A. Proctor, Proc. R. Soc. London **18**, 169 (1870).
3. *The Hipparcos and Tycho Catalogues. Astrometric and Photometric Star Catalogues Derived from the ESA Hipparcos Space Astrometry Mission* (ESA Publications Division, Noordwijk, 1997).
4. W. Dehnen, Astron. J. **115**, 2384 (1998).
5. E. Chereul, M. Crézé, and O. Bienaymé, Astron. Astrophys., Suppl. Ser. **135**, 5 (1999).
6. R. Hoogerwerf and L. A. Aguilar, Mon. Not. R. Astron. Soc. **306**, 394 (1999).
7. R. Asiain, F. Figueras, and J. Torra, Astrophys. Space Sci. **272**, 105 (2000).
8. O. J. Eggen, Fundam. Cosm. Phys. **13**, 1 (1989).
9. K. U. Ratnatunga, Astron. J. **95**, 1132 (1988).
10. T. A. Agekyan and V. V. Orlov, Astron. Zh. **61**, 60 (1984) [Sov. Astron. **28**, 36 (1984)].
11. V. V. Orlov, I. E. Panchenko, A. S. Rastorguev, and A. V. Yatsevich, Astron. Zh. **72**, 495 (1995) [Astron. Rep. **39**, 437 (1995)].

12. B. Chen, J. Torra, F. Figueras, and R. Asiain, *Proc. Intern. Conf. Structure & Evolution of Stellar Systems*, Ed. by T. A. Agekian, A. A. Mülläri, and V. V. Orlov (St. Petersburg Univ. Press, St. Petersburg, 1997), p. 118.
13. E. Chereul, M. Crézé, and O. Bienaymé, Astron. Astrophys. **340**, 384 (1998).
14. M. Barbier-Brossat, M. Petit, and P. Figon, Astron. Astrophys., Suppl. Ser. **108**, 603 (1994).
15. S. Grenier, M.-O. Baylac, L. Rolland, *et al.*, Astron. Astrophys., Suppl. Ser. **137**, 451 (1999).
16. R. Asiain, F. Figueras, J. Torra, and B. Chen, Astron. Astrophys. **341**, 427 (1999).
17. J. Binney and M. Merrifield, *Galactic Astronomy* (Princeton Univ. Press, Princeton, 1998).
18. J. A. Hartigan, *Clustering Algorithms* (John Wiley and Sons, N.Y., 1975).

Translated by A. Dambis

Astronomy Reports, Vol. 47, No. 3, 2003, pp. 176–185. Translated from Astronomicheskiĭ Zhurnal, Vol. 80, No. 3, 2003, pp. 202–211.

A Coupled, Dynamical and Chemical Model for the Prestellar Core L1544: Comparison of Modeled and Observed $C^{18}O$, HCO^+, and CS Emission Spectra

Ya. N. Pavlyuchenkov[1], B. M. Shustov[1], V. I. Shematovich[1], D. S. Wiebe[1], and Zhi-Yun Li[2]

[1] *Institute of Astronomy, Russian Academy of Sciences, ul. Pyatnitskaya 48, Moscow, 119017 Russia*

[2] *University of Virginia, Charlottesville, Virginia, USA*

Received September 24, 2002; in final form, October 10, 2002

Abstract—We consider radiative transfer in $C^{18}O$, HCO^+, and CS molecular lines in a spherically symmetrical, coupled, dynamical and chemical model of a prestellar core whose evolution is determined by ambipolar diffusion. Theoretical and observed line profiles are compared for the well-studied core L1544, which may be a collapsing protostellar cloud. We study the relationship between the line shapes and model parameters. The structure of the envelope and kinematic parameters of the cloud are the most important factors determining the shape of the lines. Varying the input model parameters for the radiative transfer—the kinetic temperature and microturbulent velocity—within the limits imposed by observations does not result in any substantial variations of the line profiles. The comparison between the model and observed spectra indicates that L1544 displays a flattened structure, and is viewed at an oblique angle. A two-dimensional model is needed to reproduce this structure. © *2003 MAIK "Nauka/Interperiodica"*.

1. INTRODUCTION

The formation of stars has been a key problem of astrophysics for many years. In spite of substantial advances in both theory and observations, we do not have a clear understanding of the collapse of a molecular cloud and its subsequent early evolution. This "missing link" in the theory of star formation has naturally attracted researchers' attention. A number of previous theoretical studies have assumed that protostellar clouds are initially gravitationally unstable, inevitably resulting in the contraction of the cloud (see, for example, [1]). In reality, the conditions in protostellar clouds are not so rigorously determined: the transition to the collapse and the early stages of the cloud's development can be very prolonged. This is suggested by statistical estimates of both the number of observed dense clouds and of their parameters [2, 3].

Several approaches to studying the initial evolution of a protostellar cloud have been suggested. The most promising involve models of magnetized collapsing clouds with ambipolar diffusion [4–6] and models with turbulent pressure (see, for example, [7, 8]). Chemical processes in the cloud and the external radiation field are no less important, though considerably less studied, factors of a cloud's evolution. A complete theory of the earliest stages of star formation can be developed only on the basis of self-consistent, coupled, dynamical and chemical models for the evolution of protostellar clouds (including the effect of the external radiation field).

These models are necessary for two basic reasons: (1) chemical and dynamical processes are interdependent; i.e., in many respects, chemical processes specify the dynamics of a molecular cloud, which in turn affect its chemical evolution; (2) knowledge of the chemical and dynamical structure of clouds is necessary for interpretation of the observed emission spectra, which are used to study the cloud dynamics.

In our papers [9–11], we presented one of the first self-consistent approaches to studying the coupled dynamical and chemical evolution of the interstellar medium. We showed, in particular, that the role of the external UV radiation is very substantial. The fate of a protostellar cloud and its internal structure are specified by the competition between evaporation and induced contraction. In these models, the impact of chemical processes on the dynamics of a cloud is not clearly expressed. However, the UV radiation can be neglected for blobs located deep inside a molecular cloud. In the absence of strong turbulent motions, the magnetic field is the dominant factor inhibiting the contraction. The contraction timescale and hence the evolution of the chemical structure of the cloud is specified by the efficiency of this inhibition. On the other hand, ions take an active part in chemical reactions; therefore, the degree of ionization and the extent to which the magnetic field is "frozen in" depend

1063-7729/03/4703-0176$24.00

on the chemical history of the cloud. To study these complicated interactions, a self-consistent model is needed.

We suggested one of the first self-consistent, coupled, dynamical and chemical models for prestellar cores with a magnetic field in [12]. We used a one-dimensional approximation to consider the evolution of a magnetized cloud, taking the ambipolar diffusion into account. Based on this model, we explained the chemical structure of the core L1544, a well-studied classical young prestellar object manifesting signs of contraction. Theoretical distributions of the radial concentrations of the CO, HCO^+, CS, CCS, N_2H^+, and NH_3 molecules are in good consistency with the observed averaged distributions. The model explains the shell ("onion-like") structure of the cloud in the CS, CCS, and CO molecules and the increase of the radial concentrations of the nitrogen-family molecules NH_3 and N_2H^+ toward the center.

It is natural to verify models via direct comparisons of the observed spectra of the molecular radiation and spectra derived theoretically from the model distributions for the velocity, abundance, etc. A simple comparison of maps of the integrated intensity of the molecular radiation and theoretical line profiles of the radial concentrations of these molecules can give an impression of how well the calculated and real chemical compositions of the cloud agree. However, the most informative comparison between the structure and kinematic parameters of the cloud and its model parameters is provided by analyses of line profiles. The first results of such a comparison carried out for a "standard" chemical model [12] with a mass of $\sim 20 M_\odot$ and an age of ~ 6 Myrs are presented in [13]. It was tentatively concluded there that the velocity of the collapse derived from the one-dimensional model was too large compared to the observations of L1544.

The influence of the chemical-model parameters on the dynamical evolution of a molecular cloud was analyzed in [13]. The chemical structure of the cloud is related to its characteristic lifetime. In the end, this restricts the velocity of the collapse: a slow contraction prolongs the cloud's evolution and results in the freezing-out of most molecules on the surfaces of dust particles. Under these conditions, the chemical composition of the cloud begins to sharply contradict the observations. In order to reproduce the chemical structure of L1544, the time for the cloud's evolution must not be too large (it should not exceed the free-fall time $t_{\rm ff}$ by more than a factor of ten).

Thus, the lack of agreement between the observed chemical structure and the dynamical parameters of L1544 and other clouds and models of their evolution remains problematic. The fitting of model spectra to the observations carried out by Tafalla *et al.* [14] formally enables estimation of the parameters of the clouds without taking into account their previous history. However, the interpretation of the results and the determination of the evolutionary status of the clouds studied using this technique seem rather ambiguous.

To identify the reasons for inconsistency between observed and theoretical line profiles, the main factors responsible for the formation of the emission lines must be clearly established. In a separate study, we will investigate possibilities for increasing the consistency between the theory and observations by varying the chemical and dynamical parameters. On the other hand, the inconsistency between the observed and model spectra may be due to factors bearing no direct relation to the coupled dynamical and chemical model and are "free" parameters of the model for the radiative transfer.

Here, we analyze the factors affecting the formation of the molecular-line profiles. We attempt to bring the theoretical $C^{18}O$, HCO^+, and CS molecular emission spectra derived from our self-consistent, coupled, dynamical and chemical model into agreement with the observed spectra by varying these factors. In Section 2, we describe the modeling of the radiative transfer. Section 3 contains the interpretation of the theoretical spectra for the standard chemical model and a comparison with the observed spectra for L1544. In Section 4, we consider models with variable radiative-transfer parameters: the temperature profile and distributions of the microturbulent velocity, regular velocity, and molecular concentration. Our results are briefly summarized in the Conclusions.

2. MODEL FOR THE RADIATIVE TRANSPORT

We consider radiative transfer in a spherically symmetrical cloud. The radial distributions for the regular velocity and the molecular concentrations are derived from self-consistent, coupled, dynamical and chemical modeling of a magnetized molecular cloud. Its dynamical evolution is specified by ambipolar diffusion and is related to the chemical evolution via the ionic abundances. The model is based on the "standard" model of [12], which provides the best consistency between the radial molecular concentrations and the observational data. Figure 1 presents the distributions of the concentration of molecular hydrogen, the regular velocity, and the HCO^+, CS and $C^{18}O$ concentrations for $t = 6.5$ Myrs. At this time, the central concentration of H_2 is $n(H_2) = 10^6$ cm^{-3}, close to that derived from observations of the microwave radiation of dust [14]. The model was calculated in an isothermal approximation.

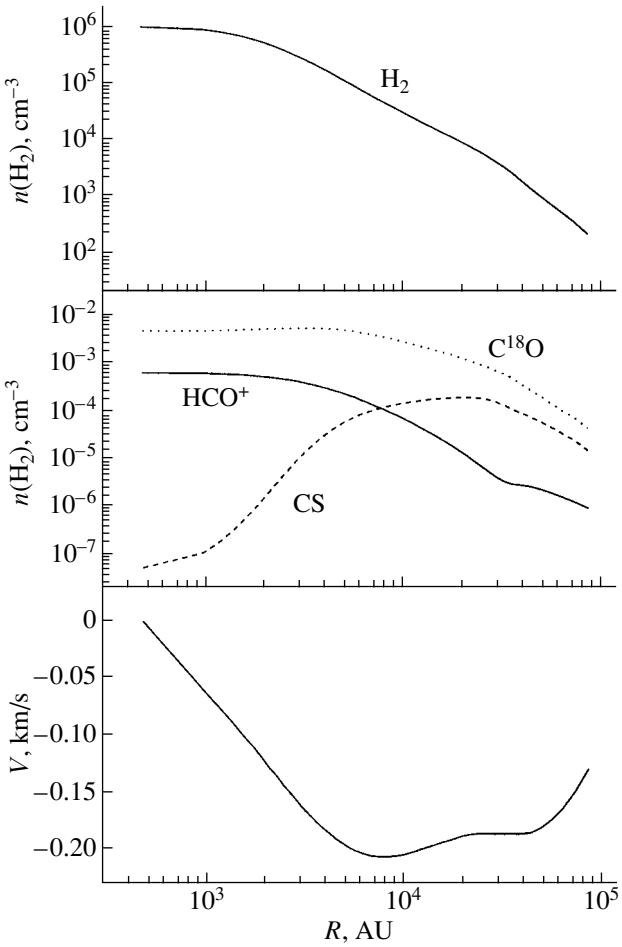

Fig. 1. Distributions of the H_2, $C^{18}O$, HCO^+, CS concentrations and the regular velocity in the standard coupled, dynamical and chemical model of L1544 [12].

The modeling of the radiative transfer is based on the solution of the equation of radiative transfer for the spectral intensity I_ν

$$\frac{\mathrm{d}I_\nu}{\mathrm{d}s} = -\alpha_\nu I_\nu + j_\nu \qquad (1)$$

and the balance equation for the level populations

$$n_l \left[\sum_{k<l} A_{lk} + \sum_{k\neq l} (B_{lk}\overline{J} + C_{lk}) \right] \qquad (2)$$
$$= \sum_{k>l} n_k A_{kl} + \sum_{k\neq l} n_k (B_{kl}\overline{J} + C_{kl}),$$

where α_ν and j_ν are the absorption and emission coefficients,

$$\alpha_\nu^{ul} = \frac{h\nu_0}{4\pi}(n_l B_{lu} - n_u B_{ul})\phi(\nu),$$
$$j_\nu^{ul} = \frac{h\nu_0}{4\pi} n_u A_{ul}\phi(\nu),$$

$\overline{J}$ is the mean intensity of the radiation,

$$\overline{J} = \frac{1}{4\pi}\int\limits_{4\pi} \mathrm{d}\Omega \int\limits_0^\infty I_\nu\, \phi(\nu)\mathrm{d}\nu,$$

n_k are the level populations, A_{ik} and B_{ik} are the Einstein coefficients, and C_{ik} are the coefficients for collisional excitation. In the approximation of a total redistribution over frequency and a Maxwellian turbulence spectrum, the line profile $\phi(\nu)$ is determined by the relation

$$\phi(\nu) = \frac{c}{b\nu_0\sqrt{\pi}} \exp\left(-\frac{c^2(\nu - \nu_0 - (\mathbf{v}\boldsymbol{\omega})\nu_0/c)}{\nu_0^2 b^2} \right).$$

Here, $\mathbf{v}$ is the regular velocity, and the parameter b is related to the kinetic temperature T_k and the most probable microturbulent velocity V_t by the expression

$$b^2 = \sqrt{\frac{2kT_\mathrm{k}}{m_\mathrm{mol}} + V_\mathrm{t}^2}.$$

The coefficients C_{ik} depend on the density and temperature of the gas; $\phi(\nu)$ is a function of the temperature and the microturbulence and regular velocities. Thus, the input model parameters for the radiative transfer are the radial distributions of the gas density (H_2), the molecular concentrations, the temperature, and the microturbulent velocity, as well as the regular velocity field.

We modeled the radiative transfer and constructed the spectrum using the RATRAN package [15], designed for the calculation of level populations and the radiation field in a one-dimensional approximation. The system of equations (1)–(2) was solved using the accelerated Λ iteration (ALI) method, where the mean intensity $\overline{J}$ is calculated using the Monte-Carlo technique. For each cell of the calculation domain, $\overline{J}$ is calculated as the average of the intensities $I(\boldsymbol{\omega}_i)$ for a set of random directions $\boldsymbol{\omega}_i$. The resulting $\overline{J}$ is used in the next step of the iterations to refine the level populations. Direct calculation of $\overline{J}$ makes it possible to divide the radiation into external and internal parts, the latter being generated by the gas within the cell. As a result, an internal subiteration process of bringing $\overline{J}$ and n_k into agreement can be introduced, which substantially accelerates the convergence of the entire procedure, especially for optically thick media.

Particular attention should be given to the partition of the calculation domain into cells. In our calculations, we made sure that the optical depth of each cell for each frequency interval did not exceed 0.1 in regions of the cloud that contribute substantially to the resulting line profile. The grid on which the dynamical modeling is carried out sometimes does not satisfy the criterion of small optical depth; for this

reason, when it was required to model a particular line profile, a special grid was made, on which the results of the dynamical calculations were interpolated. Multiple test calculations of line profiles with increased spatial resolution were carried out to check the reliability of the results.

The molecular constants for the radiative-transfer model were taken from [16] for $C^{18}O$, from [15] for HCO^+, and from [17] for CS. The corresponding collisional excitation coefficients C_{ik} were taken from [18], [15], and [19], respectively. In the course of the spectral modeling, the frequency resolution was selected to be comparable to the resolution of observations of prestellar cores.

3. RESULTS FOR THE STANDARD MODEL

The input model parameters for the radiative transfer and the derivation of the spectrum are the radial distributions of the kinetic temperature and microturbulent velocity. Unfortunately, it is not possible to derive these distributions directly from observations of real objects. As a rule, only mean values for a cloud can be obtained. According to the observations of [14, 20], the temperature and microturbulent velocity of L1544 are $T_k = 8$–10 K and $V_t = 0.1$–0.2 km/s. To obtain the basic model spectra, we assumed

(1) a uniform distribution for the kinetic temperature $T_k = 8.75$ K;

(2) a uniform field for the microturbulent velocity $V_t = 0.15$ km/s.

The microwave background radiation with a temperature of $T = 2.75$ K was also taken into account when modeling the radiative transfer. To compare the model and observations, we used emission spectra of L1544 in the rotational transitions $C^{18}O(J = 1$–$0)$ [14] and $CS(J = 2$–$1)$ [21], and observations in the $HCO^+(J = 3$–$2)$ [22] transition.

Figure 2 compares the theoretical line profiles obtained in the standard chemical model for the direction toward the center of the cloud and the observations. The intensity is given in units of the radiation temperature T_R (with the microwave background subtracted). When calculating the theoretical spectra, we assumed that the beamwidth of the telescope is very small compared to the size of the object. In principle, this assumption makes a direct comparison between the theoretical and observed line profiles not entirely correct. However, since taking into account the finite resolution (as a rule, of the order of 15″) does not substantially change either the shape or the intensity of the line profiles, we did not carry out the required convolution, preferring to represent lines in their "pure" state.

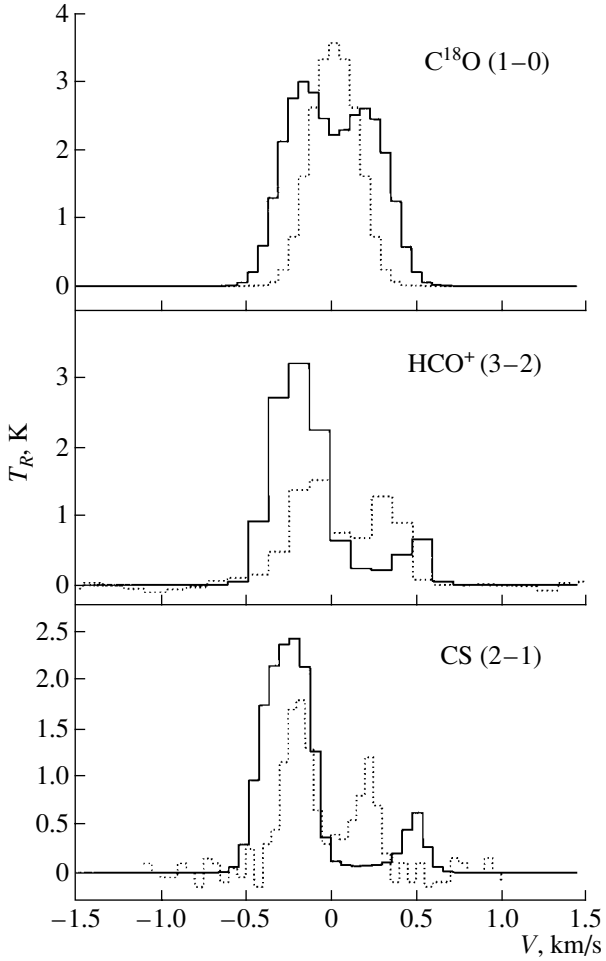

Fig. 2. Line profiles $C^{18}O(1$–$0)$, $HCO^+(3$–$2)$, and $CS(2$–$1)$ for the standard model (solid), and the corresponding observed line profiles for the prestellar core L1544 (dotted) for $C^{18}O$ [14], HCO^+ [22], and CS [21].

Substantial differences between the observed and modeled line profiles are obvious. The theoretical $C^{18}O(1$–$0)$ line has an optical depth at the maximum $\tau = 0.9$. The profile of this line is saddle-shaped, reflecting the infall of material toward the center of the cloud, and is broader than the observed line. The $HCO^+(3$–$2)$ and $CS(2$–$1)$ line profiles are very asymmetrical, also related to the collapse of the object. Their intensity and width appreciably exceed those of the observed lines. The deep dips in the line profiles are due to self-absorption. The optical depth of the theoretical $HCO^+(3$–$2)$ line at the maximum is $\tau = 35$; the maximum optical depth of the $CS(2$–$1)$ line is $\tau = 30$. As a result, these dips are much deeper than in the observed lines. Thus, we can conclude that the emission spectra of L1544 constructed with uniform distributions of the temperature and microturbulent velocity and a self-consistent distribution

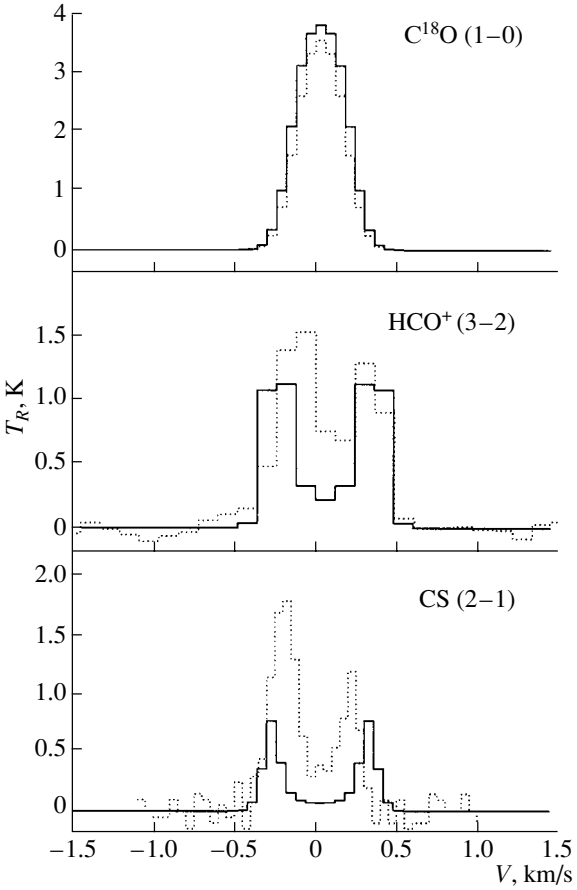

Fig. 3. $C^{18}O(1-0)$, $HCO^+(3-2)$, and $CS(2-1)$ line profiles for the standard model with $V_r = 0$ (solid curves). The dotted curves indicate the observed spectra (as in Fig. 2).

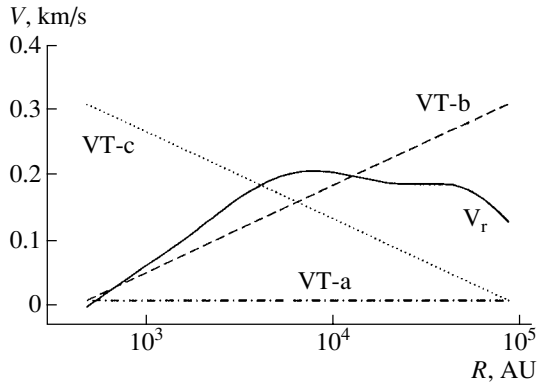

Fig. 4. Model distributions for the microturbulent velocity (models VT-a, VT-b, and VT-c) and for the modulus of the regular velocity V_r (see also Fig. 1).

for the regular velocity field differ appreciably from the observations.

At first glance, the increased (compared to the observations) width of the theoretical lines and their double-peak structure, which is not displayed by the optically thinner observed $C^{18}O(1-0)$ line and is more symmetrical in the $HCO^+(3-2)$ and $CS(2-1)$ lines, can find their simplest explanation in the large regular velocity assumed in the model. This general conclusion is supported by our radiative-transfer calculation for a cloud with the same distributions for the density, chemical composition, temperature, and microturbulent velocity, but with zero regular velocity V_r. Figure 3 presents the corresponding spectra. In the absence of large-scale motions in the cloud, the widths of all the lines approach the observed values. The $C^{18}O(1-0)$ line loses its double-peak structure and virtually coincides with the observed profile. The optically thick lines display a more complicated behavior. The dip due to self-absorption remains broader and deeper than in the observed profile. This can be explained by a large self-absorption, due to the increased abundance of the considered molecules in the envelope (in a region with less than the critical density).

Summarizing, we conclude that our coupled, dynamical and chemical model predicts too high a velocity for the collapse and overestimates the abundances of some molecules in the envelope. However, we should first check if the discrepancies could be due to poorly selected parameters for the radiative-transfer model.

4. VARIATION OF THE MODEL PARAMETERS

4.1. Distribution of the Microturbulent Velocity

In the standard model, we assumed that the microturbulent velocity was constant throughout the cloud. In reality, however, it may increase or decrease from the center to the peripheral zones of the object. A minimum V_t at the center of the cloud may be reached if there are strong sources of turbulence (such as Alfven waves) outside the cloud. An increasing V_t toward the center could be related to a possible increase of the turbulent energy in the course of the collapse. Observations also confirm the presence of different distributions for the turbulence in different molecular clouds [23, 24]. In this section, we will use several examples to check if models with a nonuniform distribution for the microturbulent velocity provide better consistency between the theoretical and observed spectra.

We considered the following cases: (1) model VT-a, in which $V_t(r) = 0$, (2) model VT-b, in which $V_t(r) = 0.2\ln(r/r_0)/\ln(R/r_0)$, (3) model VT-c, in which $V_t(r) = 0.2\ln(r/R)/\ln(r_0/R)$ km/s,

where R is the radius of the cloud and r_0 the inner truncation radius for the V_t distribution. The VT-a

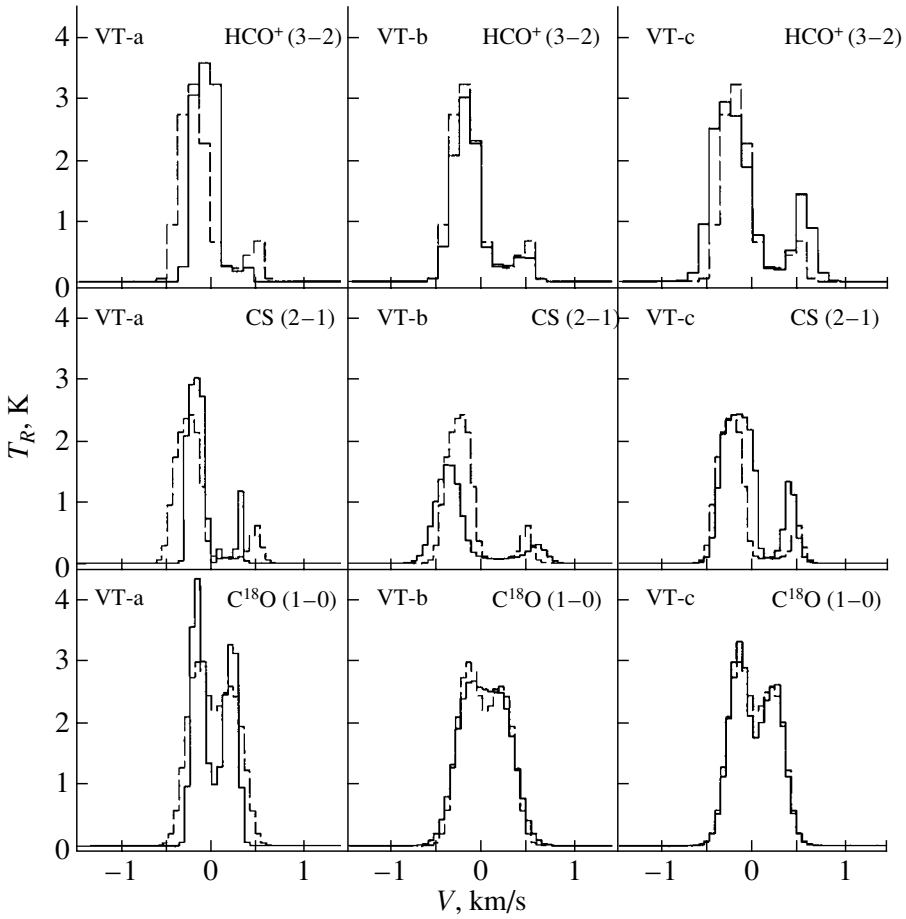

Fig. 5. The solid curves show the $C^{18}O(1-0)$, $HCO^+(3-2)$, and $CS(2-1)$ line profiles for the standard model with various relations between the microturbulent velocity and the radius (models VT-a, VT-b, and VT-c, see Fig. 4). The dashed curves correspond to spectra constructed in the standard model with $V_t = 0.15$ km/s.

case corresponds to strong dissipation of the turbulence or to weakness of the sources of turbulence. The second and third expressions correspond to a linear (in the logarithm of the distance) increase and decrease of V_t approximately from zero to 0.3 km/s. Figure 4 presents the distributions of V_r and V_t in these cases, while Fig. 5 presents the corresponding line profiles calculated for the uniform temperature distribution with $T_k = 8.75$ K.

Adopting a zero microturbulent velocity partially solves the problem of the excessive line widths, however the shapes of the line profiles in this case become even less similar to the observed profiles. In all the lines, the dips related to the presence of the regular velocity and self-absorption become deeper. In the $HCO^+(3-2)$ line, one of the peaks virtually totally disappears.

Specifying a microturbulent velocity that varies with radius affects the lines forming at the center and in the envelope of the cloud in different ways. Increasing V_t in the envelope (model VT-b) alters the shapes of the $CS(2-1)$ and $C^{18}O(1-0)$ lines, while the profiles of the $HCO^+(3-2)$ line remain essentially unaffected. The dip in the $CS(2-1)$ line becomes broader, while the $C^{18}O(1-0)$ line forming nearest the boundary of the cloud becomes more similar to the observed one-peak profile. However, its width appreciably exceeds the observed value. Increasing V_t toward the center of the cloud significantly affects only the $HCO^+(3-2)$ line, making it broader compared to its profile for the standard model.

Overall, varying the distribution of the microturbulent velocity within the indicated limits improves the consistency with the observations only for the $C^{18}O(1-0)$ line. For the other lines, the discrepancies with the observations become even sharper.

4.2. Temperature Distribution

When using the standard model, we assumed that the kinetic temperature in the cloud was constant with radius. However, the thermal structure of the

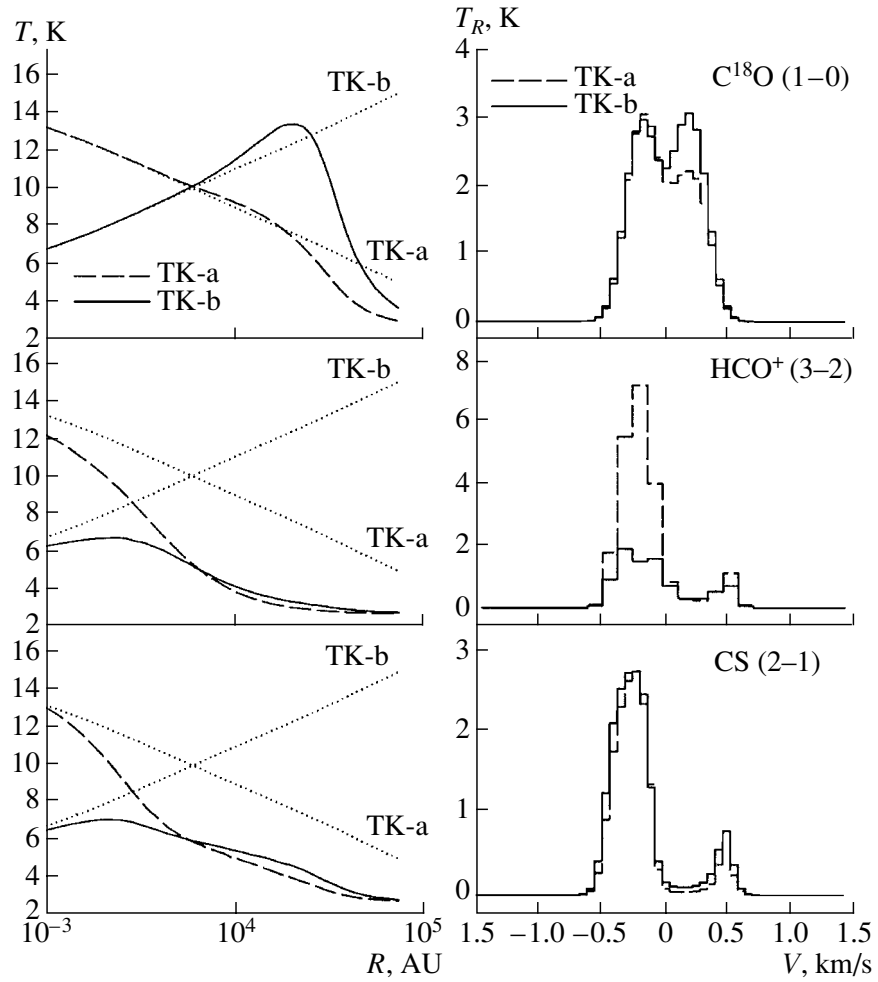

Fig. 6. The left plots present the model distributions of the kinetic temperature TK-a and TK-b (dotted) and the distributions of the excitation temperature in these models (dashed and solid). The right plots present the calculated profiles for the $C^{18}O(1-0)$, $HCO^+(3-2)$, and CS(2–1) emission lines. The dashed and solid curves correspond to the TK-a and TK-b distributions.

cloud may be nonuniform. For example, in the presence of external ultraviolet illumination, the cloud acquires a positive temperature gradient (see, for example, [9]). On the other hand, a negative gradient (an increase of the temperature inwards) can occur in optically thick clouds or clouds with turbulent dissipation. We used the following distributions to model these situations:

(1) model TK-a has
$T_k(r) = 15 - 10\ln(r/r_0)/\ln(R/r_0)$,

(2) model TK-b has
$T_k(r) = 5 + 10\ln(r/R)/\ln(r_0/R)$,

where r_0 and R are the same as in Section 4.1. The TK-a and TK-b distributions correspond to negative and positive temperature gradients. Formally, these distributions are inconsistent with the coupled dynamical and chemical model, which is based on an isothermal approximation. However, the decrease of T_k described by these expressions is small (roughly from 7 to 15 K), so that it will not substantially affect the chemical and dynamical parameters of the cloud. At the same time, the variation of the excitation temperature due to the gradient of T_k can be more appreciable and can result in significant variation of the line shapes.

Figure 6 presents the line profiles and the relations between the excitation temperature and radius corresponding to the TK-a and TK-b distributions. To derive these spectra, we assumed $V_t = 0.15$ km/s.

The shape of the $C^{18}O(1-0)$ line profile is only slightly affected by the temperature variation. Since the critical density for this molecule is low ($n_{cr} \sim 10^3$ cm^{-3}), radiation is generated not only by the core of the cloud, but also by its envelope (Fig. 6). As a result, with the positive temperature gradient, the characteristic "collapse" line profile that appears for $T_k = \text{const}$, with the blue peak dominating over the

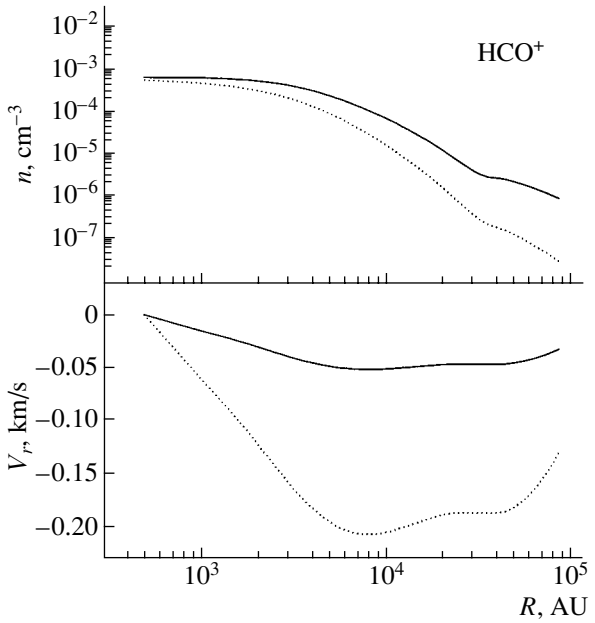

Fig. 7. Distribution of the HCO^+ molecular concentration and regular velocity in the standard model (dotted) and in the model with a decreased regular velocity and concentration of HCO^+ (solid).

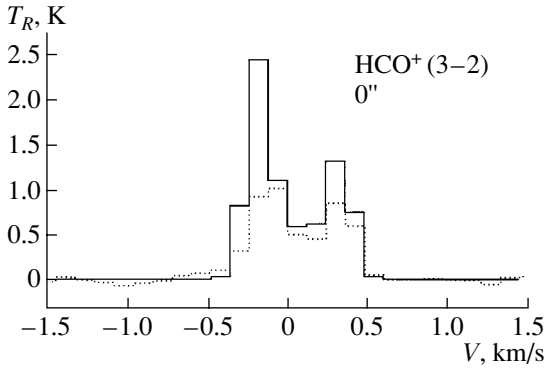

Fig. 8. $HCO^+(3–2)$ line profile for the distributions of the regular velocity and concentration presented in Fig. 7 (solid). The observed line profile [22] is dotted.

red, is transformed into a profile with the opposite asymmetry.

The shape and intensity of the $HCO^+(3–2)$ line depend on the radial temperature distribution more substantially: when the temperature increases toward the center, the line intensity is significantly higher than in the case of increasing temperature toward the envelope. This is due to the fact that, at the center of the cloud, where the collisional excitation of the molecules reaches its maximum, so does the concentration of HCO^+ (Fig. 1). As a result, radiation is generated primarily in the central region, and its intensity corresponds to the central temperature.

At the same time, the variation of the temperature distribution only weakly affects the parameters of the CS(2–1) line. The reason is that the concentration of the CS molecules reaches its maximum in the region $r \sim 10^4$ AU (Fig. 1), where the temperatures of both distributions are similar. The region of subcritical density for the collisional excitation of CS begins at $r > 10^4$ AU, and radiative excitation dominates in this zone. In this case, the temperature variation in the envelope essentially does not affect the distribution of the excitation temperature (Fig. 6) and hence the line intensity.

Thus, despite the fact that radial variations of T_k and of V_t are able to alter the line profiles for individual molecules in the "needed" way, such variations are not able to explain the observed spectra as a whole. The decrease of the $HCO^+(3–2)$ line intensity could be considered the only positive effect of taking into account the radial dependence of T_k. In the standard model, the intensity of this line exceeds the observed value by more than a factor of two (Fig. 2).

It is apparent that simultaneous variation of V_t and T_k will not help either, since the variation of either of these parameters does not act to remove the main discrepancies: the dramatic asymmetry of the lines and the simultaneous deep dips in all three model line profiles.

4.3. Distributions of the Regular Velocity and Molecular Abundance

We conclude that variations of the distributions of the microturbulent velocity and kinetic temperature (within observationally justified limits) do not significantly reduce the inconsistency between the theoretical and observed spectra. This leaves the possibility that this inconsistency is due to limitations inherent to the one-dimensional, coupled, dynamical and chemical model.

As is noted in Section 2, one of the main discrepancies between the theoretical and observed spectra is that the theoretical line profiles are too broad. The most natural explanation for this is the high velocity of collapse in the model. According to the observations, the regular velocity in L1544 is $V_r \sim 0.1$ km/s on scales of the order of both 0.1 pc and 0.01 pc [25, 26]. The study [14] even suggests $V_r = 0$ km/s, based on varying model distributions of physical parameters and comparing spectra. In our standard model, the amplitude of the regular velocity reaches 0.2 km/s. Approximately the same velocity was derived from the two-dimensional model for the object developed by Ciolek and Basu [27]. However, our results indicate that the widths and shapes of the observed lines cannot be fit with this velocity in the one-dimensional

model for L1544. In addition, the model line profiles for optically thick lines display deeper dips than the observed lines, due to the fact that the theoretical concentrations of the corresponding molecules in the envelope of the cloud are too high.

These characteristics of the evolutionary model (a high velocity of collapse and enhanced concentrations of a number of molecules in the envelope) cannot be removed even when the free parameters are varied over a broad range. This is probably associated with limitations of the one-dimensional approximation. The object L1544 displays a non-spherical and possibly flattened shape. If it is observed at some angle, we expect the velocity along the line of sight to be lower and the envelope more rarefied, compared to the predictions of the spherically symmetrical model. Therefore, in the one-dimensional model, the object will appear chemically to be in an earlier stage of evolution.

To verify this suggestion qualitatively, we calculated the model profile for the $HCO^+(3–2)$ line with the regular velocity artificially decreased by a factor of four. In addition, the concentration of this ion was divided by α, which is unity at the center of the cloud and linearly increases with distance to its maximum value $\alpha_{max} = 30$ at the outer boundary (Fig. 7). This correction does not appreciably affect the radial concentration. When deriving this spectrum, the distributions of the temperature and microturbulent velocity were assumed to be uniform, as in the standard model. Figure 8 displays the resulting line profile. It is apparent that the corrected spectrum is much more consistent with the observations than the standard spectrum. As expected, the reduced velocity results in the desired decrease of the line width. The depth of the dip has also been reduced substantially. The consistency for the other lines can be increased in a similar way. Thus, our preliminary calculations confirm the suggestion that the geometry of the object L1544 differs from simple spherical symmetry. A similar conclusion was drawn in [27]. However, a final determination of the shape and orientation of this cloud can be made only by comparing observations and the results of two-dimensional modeling.

5. CONCLUSION

We have compared the observed profiles of the $C^{18}O$, HCO^+, and CS molecular lines of the object L1544 and profiles constructed using a self-consistent, coupled, dynamical and chemical model for a magnetized prestellar core. The comparison indicates that the theoretical and observed line profiles differ substantially, although the same one-dimensional model yields reasonable consistency between the theoretical and observed radial line profiles for the radial concentrations of the key molecules. Kinematic (the regular velocity field, i.e., the collapse velocity) and structural (the structure of the outer layers, i.e., the envelope of the cloud) factors are most important for these inconsistencies. Varying the distributions of the microturbulent velocity and kinetic temperature cannot remove the discrepancies in all the line profiles; however, the shapes of individual lines can be changed toward the "needed" direction. To all appearances, L1544 displays a flattened structure, which requires a two-dimensional, coupled, dynamical and chemical model and a two-dimensional model for the radiative transfer.

6. ACKNOWLEDGMENTS

This work was supported by the Russian Foundation for Basic Research (project nos. 02-02-04008, 01-02-16206). The authors are grateful to A. M. Sobolev for useful discussions and comments.

REFERENCES

1. B. M. Shustov, *Modern Problems of Stellar Evolution* [in Russian] (Geos, Moscow, 1998), p. 1.
2. C. A. Beichman, Astrophys. J. **307**, 337 (1986).
3. T. L. Bourke, A. R. Hyland, and G. Robinson, Mon. Not. R. Astron. Soc. **276**, 1052 (1995).
4. A. E. Dudorov and Yu. V. Sazonov, Nauchnie Informatsii Astrosoveta AN SSSR **42**, 110 (1987).
5. Z.-Y. Li, Astrophys. J. **493**, 230 (1998).
6. G. E. Ciolek and T. C. Mouschovias, Astrophys. J. **418**, 774 (1993).
7. R. S. Klessen, F. Heitsch, and M.-M. MacLow, Astrophys. J. **535**, 887 (2000).
8. F. Heitsch, M.-M. MacLow, and R. S. Klessen, Astrophys. J. **547**, 280 (2001).
9. D. S. Wiebe, V. I. Shematovich, and B. M. Shustov, Astron. Zh. **73**, 702 (1996) [Astron. Rep. **40**, 639 (1996)].
10. V. I. Shematovich, B. M. Shustov, and D. S. Wiebe, Mon. Not. R. Astron. Soc. **292**, 601 (1997).
11. V. I. Shematovich, D. S. Wiebe, and B. M. Shustov, Astron. Zh. **76**, 738 (1999) [Astron. Rep. **43**, 645 (1999)].
12. Z.-Y. Li, V. I. Shematovich, D. S. Wiebe, and B. M. Shustov, Astrophys. J. **569**, 792 (2002).
13. V. I. Shematovich, D. S. Wiebe, B. M. Shustov, *et al.*, *Abstracts of SFCHEM 2002: Chemistry as a Diagnostic of Star Formation* (University of Waterloo, Waterloo, Canada, 2002), p. 11.
14. M. Tafalla, P. C. Myers, P. Caselli, *et al.*, Astrophys. J. **569**, 815 (2002).
15. P. C. Hogerheide and F. F. S. van der Tak, Astron. Astrophys., Suppl. Ser. **362**, 697 (2000).
16. S. Chandra, V. U. Maheshwari, and A. K. Sharma, Astron. Astrophys., Suppl. Ser. **117**, 557 (1996).
17. S. Chandra, W. H. Kegel, R. J. Le Roy, and T. Hertenstein, Astron. Astrophys., Suppl. Ser. **114**, 175 (1995).

18. D. R. Flower and J. M. Launay, Mon. Not. R. Astron. Soc. **214**, 271 (1985).
19. S. Green and S. Chapman, Astrophys. J., Suppl. Ser. **37**, 169 (1978).
20. P. Caselli, C. W. Walmsley, *et al.*, Astrophys. J. **565**, 331 (2002).
21. C. W. Lee, P. C. Myers, and M. Tafalla, Astrophys. J., Suppl. Ser. **136**, 703 (2001).
22. J. E. Lee *et al.*, Astrophys. J., in press (2003).
23. P. Caselli and P. C. Myers, Astrophys. J. **446**, 665 (1995).
24. A. V. Lapinov, P. Schilke, M. Juvela, and I. I. Zinchenko, Astron. Astrophys. **336**, 1007 (1998).
25. M. Tafalla *et al.*, Astrophys. J. **504**, 900 (1998).
26. J. P. Williams, P. C. Myers, D. J. Wilner, and J. di Francesco, Astrophys. J. **513**, L61 (1999).
27. G. E. Ciolek and S. Basu, Astrophys. J. **529**, 925 (2000).
28. Y. Aikawa, S.-I. Inutsuka, E. Herbst, and S. Takakuwa, Astrophys. J. **552**, 639 (2001).

Translated by K. Maslennikov

Astronomy Reports, Vol. 47, No. 3, 2003, pp. 186–196. Translated from Astronomicheskiĭ Zhurnal, Vol. 80, No. 3, 2003, pp. 212–222.

Supersoft X-ray Sources. Parameters of Stellar Atmospheres

A. A. Ibragimov[1], V. F. Suleĭmanov[1], A. Vikhlinin[2], and N. A. Sakhibullin[1]

[1] *Kazan State University, Kazan, Tatarstan, Russia*

[2] *Space Research Institute, Moscow, Russia*

Received March 5, 2002; in final form, October 10, 2002

Abstract—ROSAT spectra of 11 supersoft X-ray sources are approximated with theoretical spectra obtained in LTE models for the atmospheres of hot white dwarfs with line blanketing. The confidence intervals of parameters derived from these approximations—$T_{\rm eff}$, log, g, $N_{\rm H}$, and R^2/d^2—are determined. The results are compared with predictions for a model with stable/recurrent thermonuclear burning on the white-dwarf surface. © *2003 MAIK "Nauka/Interperiodica".*

1. INTRODUCTION

Supersoft X-ray sources (hereafter "supersoft sources") are a class of X-ray object distinguished by ROSAT observations [1–3]. The main characteristic of these objects is a very soft X-ray spectrum that falls off near 0.5–1 keV. Blackbody approximations to the X-ray spectra yield temperatures from 10 to 80 eV. As a rule, the luminosities derived from such approximations are very high ($\geq 10^{38}$ erg/s), and often exceed the Eddington limit for solar-mass objects. The first observations of supersoft sources were obtained by the Einstein Observatory, but ROSAT was the first satellite that was able to distinguish them as a distinct class and detect significant numbers of these sources. Currently, about 60 bright supersoft sources are known, located in our Galaxy, the Magellanic Clouds, the Andromeda galaxy, and NGC 55 [4].

One widely adopted model that can explain the nature of at least classical double supersoft sources is that of van den Heuvel *et al.* [5], in which supersoft sources are close binary systems containing a white dwarf and a more massive subgiant secondary that overfills its Roche lobe. If the mass of the latter star is approximately twice the mass of the white dwarf, the accretion onto the white dwarf occurs on the thermal time scale for the secondary at a high rate ($\sim 10^{-7}\,M_\odot$/yr), which gives rise to stable nuclear burning on its surface, leading to the observed soft X-ray emission. The theoretical possibility of such a situation was predicted in [6] and subsequently studied in detail by a number of authors [7–10].

The spectral energy distribution of such a supersoft source should be described by the theoretical spectrum of a white-dwarf model atmosphere with the appropriate effective temperature $T_{\rm eff}$, gravitational acceleration g, and chemical composition A (see Section 3). Atmospheres with $T_{\rm eff} \sim 10^5$–10^6 K radiate more efficiently at energies 0.1–0.5 keV than a blackbody, so that applying LTE model atmospheres without taking lines into account yielded bolometric luminosities for supersoft sources that were below the Eddington limit for a solar-mass object [11].

The X-ray spectra of supersoft sources have been approximated using a variety of theoretical models, from blackbody models to non-LTE models taking line absorption into account [12]. The parameters of most sources have been estimated using LTE models without including the effect of line absorption.

Our goal in the current study was to rereduce series of ROSAT observations of known supersoft sources using a unified method, in order to derive the physical characteristics of these objects in a uniform way, approximating the observed fluxes using theoretical spectra for blanketed (i.e., including the effect of lines) LTE model atmospheres for hot white dwarfs. It is obvious that considering blanketing of non-LTE model atmospheres for hot white dwarfs would be more realistic, but such computations are appreciably more complex and time-consuming [13]. In addition, we note that the temperature structures of blanketed non-LTE and LTE model atmospheres are very similar and differ substantially from non-LTE models without line absorption [14]. Therefore, we consider blanketed LTE-model atmospheres of hot white dwarfs to be more realistic than non-LTE models without line absorption [15].

Recent high resolution ($\sim$0.06 Å) calibration observations of the source CAL 83 by the XMM-Newton satellite [16] showed that its spectrum is rich in absorption lines. This indicates the photospheric nature of the spectrum and demonstrates that any detailed analysis of the X-ray spectra of these objects

1063-7729/03/4703-0186$24.00

obtained by the new generation of space observatories must make use of the method of synthetic spectra.

The full designations of the sources are presented in Table 2. We will use shortened designations consisting only of the first several symbols.

In all, we studied ten supersoft sources. We also present data for AG Dra; although its spectrum is very soft, the resulting parameters are very uncertain and are not interpreted further. The parameters of the two sources RX J0527 and RX J0513 are the first derived using white-dwarf model atmospheres.

2. DATA REDUCTION

The sample of sources corresponds to the list of Greiner [4]. A number of objects were excluded due to the absence of satisfactory observations or the exceptional softness of their spectra, which led to very large uncertainties in their parameters (the results for AG Dra demonstrate what occurs in this case). In the end, we used 11 sources and 13 observations in our study.

The spectra of the objects were extracted from a circular region with a radius large enough to include the majority of the photons. Information about the background was extracted from a zone having an area several times larger surrounding the source. To increase the signal-to-noise ratios and obtain a high correspondence to the energy resolution of the detector, the spectral flux densities were recalculated to new energy channels that were broader than the instrumental channels (Table 1).

We estimated the physical parameters of the sources by approximating the observed spectra with theoretical spectra derived from computations of blanketed LTE model atmospheres taking into account interstellar absorption. The free parameters in the fitting were the column density of interstellar hydrogen $N_{\rm H}$, the effective temperature of the model atmosphere $T_{\rm eff}$, and a normalization factor accounting for the geometrical decrease in the flux, R^2/d^2 (R is the source radius and d is the distance to the source). The gravitational acceleration $\log g$ was fixed at a preliminarily determined optimal value (this parameter influences the spectrum much more weakly than the others; see Section 4).

Table 2 presents the main data on the sources and the parameters of the observations used.

Table 1. Grouping of counts in broad channels (from one-third to one-half the energy resolution of the detector) used in the analysis

Channel number	Energy, keV	Channel number	Energy, keV
1	0.16–0.20	8	0.87–1.04
2	0.21–0.26	9	1.05–1.24
3	0.27–0.34	10	1.25–1.46
4	0.35–0.44	11	1.47–1.69
5	0.45–0.56	12	1.70–1.93
6	0.57–0.70	13	1.94–2.23
7	0.71–0.86		

3. METHOD FOR COMPUTING THE HOT WHITE-DWARF MODEL ATMOSPHERES

The model atmospheres were characterized by their effective temperature $T_{\rm eff}$, surface gravitational acceleration g, and a scaling factor for the abundance of elements heavier than helium A. Solar chemical composition corresponds to $A = 1$, and a heavy-element content a factor of ten lower corresponds to $A = 0.1$. We assumed that the atmosphere was stationary and static, and consisted of uniform, plane-parallel layers.

The model atmosphere was found numerically, and the distribution of atoms and ions in terms of their excitation and degrees of ionization were determined by the Saha and Boltzmann equations assuming local thermodynamic equilibrium. We used a modified version of the ATLAS5 code of Kurucz [17]. The computations included the 15 most widespread elements (H, He, C, N, O, Ne, Na, Mg, Al, Si, S, Ar, Ca, Fe, Ni). In contrast to the original code of Kurucz, we considered all ionization states. Data on the opacity cross sections were taken from [18]. We also took into account Thomson scattering on free electrons (Compton effects in the atmospheres ot white dwarfs weaken as the gravitational acceleration increases, and do not influence the continuum spectrum [19]). We included about 1200 of the strongest spectral multiplets and lines (for the ionization states corresponding to the conditions in the atmosphere) selected from the list [20], whose effect was determined via direct integration. We took the line profiles to be Voigt profiles broadened by natural damping, the Doppler effect (taking the microturbulent velocity to be 1 km/s), and the Stark effect. The Stark half-width was computed using the simple approximation formula of [21]. We used a grid of $\sim$8000 points in frequency (from 3×10^{13} to 10^{21} Hz) and 100 points in depth to solve the radiative-transfer equation using

Table 2. Data on sources and observations used

Object	Observation	α	δ	Count rate, phot/s	Off-axis angle
RX J0439.8-6809	rp400161n00	$04^h39^m49\overset{s}{.}6$	$-68°09'01''$	1.40	$1\overset{'}{.}52$
RX J0513.9-6951	rp900398a02	05 13 48 8	−69 52 00	1.95	0.57
RX J0527.8-6954	rp400148n00	05 27 48 6	−69 54 02	0.12	0.06
CAL 87	rp400012n00	05 46 45 0	−71 08 54	0.12	0.10
CAL 83	rp110180n00	05 43 33 5	−68 22 23	0.53	40.29
1E 0035.4-7230	rp400299n00	00 37 19 0	−72 14 14	0.52	0.17
	rp400149n00			0.41	0.17
RX J0048.4-7332	rp600196a01	00 48 20 0	−73 31 55	0.17	20.87
1E 0056.8-7154	rp600455a02	00 58 37 1	−71 35 48	0.33	18.30
	rp400300a01			0.37	0.38
RX J0019.8+2156	rp400322n00	00 19 50 1	+21 56 54	1.96	0.10
RX J0925.7-4758	rp900377n00	09 25 42 0	−47 58 00	0.68	40.99
AG Dra	rp200689n00	16 01 41 1	+66 48 10	1.09	1.88

Note: The last column indicates the deviation of the position of the source from the optical axis of the telescope in the field of view of the detector.

the method of [22] for three angles. The upper boundary condition assumed the absence of a rising flux at the first surface point. We used a diffusion approximation as a lower boundary condition. The temperature structure of the atmosphere was computed using a temperature-correction method.

In some high-lying points in the atmosphere (which exert virtually no influence on the emergent flux), the radiation pressure can exceed the gravitational force. Physically, this implies the presence of a stellar wind from the surface of the white dwarf. However, the study of this wind falls outside the framework of the problem at hand, and we will ignore its effect.

4. RESULTS OF THE COMPUTATIONS

We computed a grid of model white-dwarf atmospheres with solar chemical composition [23] and with effective temperatures 5×10^4–1.3×10^6 K in steps of 10^4 K and surface gravities $\log g = 7.0$–9.5 in steps of 0.5 for comparison with the observations. We computed only the models that did not exceed the Eddington limit, i.e., with $\log g > \log g_E$. This limiting surface gravity $\log g_E$ is specified by the relation

$$\log g_E = 4.88 + 4 \log T_5, \qquad (1)$$

where $T_5 = T_{eff}/10^5$ K.

The results of the computations are illustrated in Fig. 1. Figure 1a shows the temperature structures of the blanketed and unblanketed models. Figure 1b shows the difference between the model spectra without lines (dashed) and with lines (solid). This difference is more clearly visible in Fig. 1c, which shows the spectra averaged over intervals of 10 eV. The flux of the blanketed model is lower at high energies and higher at softer energies than that of the unblanketed model, reflecting the differences in their temperature structures. There are also local dips associated with the presence of large numbers of strong lines in these regions. Note that the uncertainty associated with our poor knowledge of the magnitude of the Stark effect for the spectral lines does not significantly influence the resulting spectral energy distribution.

Figure 2 shows the dependence of the spectra on variations of the model parameters: effective temperature (Fig. 2a), surface gravity (Fig. 2b), and heavy-element abundance (Fig. 2c). At energies above 0.5 keV, variations in the slope and overall flux of the spectra are most appreciable in the presence of variations of the effective temperature. Variations of $\log g$ influence the overall redistribution of energy much more weakly, and variations of the chemical composition are manifest only via differing values for absorption jumps.

5. FITTING TECHNIQUE

The PSPC instrument on ROSAT has the following characteristics at soft energies. The energy

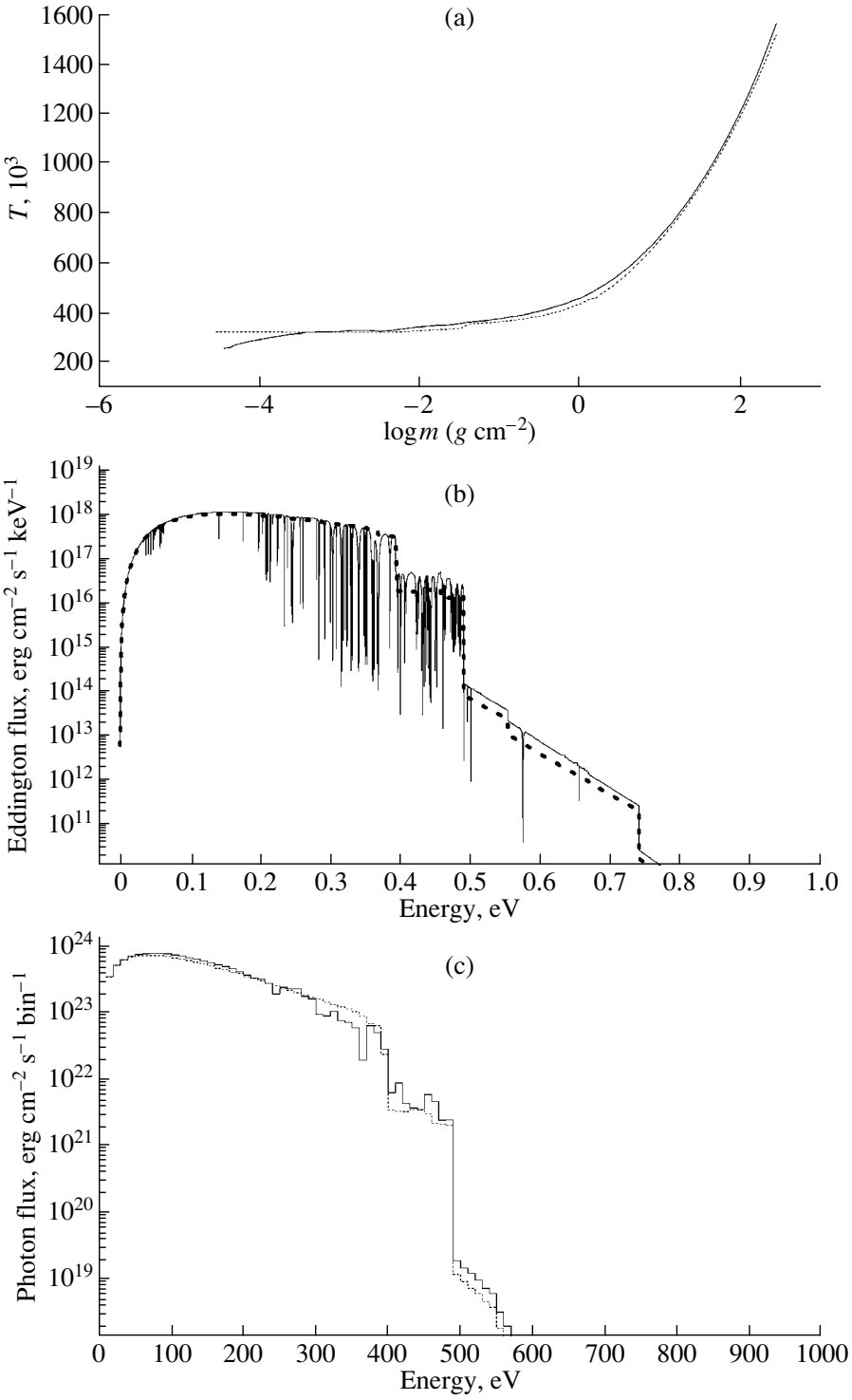

Fig. 1. Difference between blanketed and unblanketed white-dwarf model atmospheres: (a) temperature structure (m is the column density), (b) spectra, and (c) spectra averaged over 10 eV. The model parameters are $T_{\rm eff} = 500\,000$ K, $\log g = 8.5$, $A = 1$. The solid curve shows the model with lines, while the dotted and dashed curves show the model without lines.

resolution of the detector ($\Delta E/E$) to 0.5 keV is about 90%. The detector has no sensitivity near 0.4 keV since photons with this energy are absorbed in the film shielding the instrument. In addition, absorption in the interstellar medium exerts a large influence at these energies. If there are no photons with energies

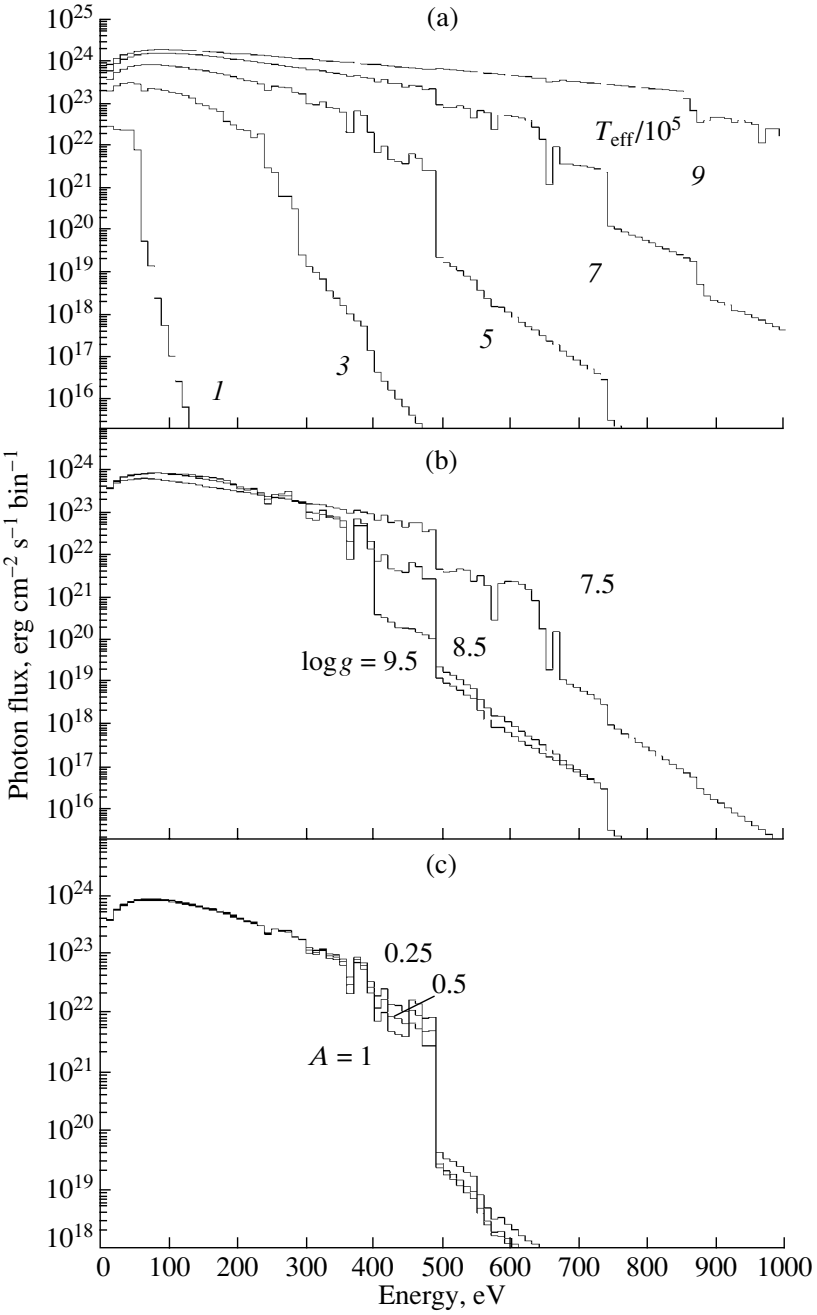

Fig. 2. Atmospheric model spectra as functions of the (a) effective temperature ($\log g = 8.5$, solar chemical composition, $T_{\rm eff} = (1{-}9) \times 10^5$ K), (b) surface gravity ($T_{\rm eff} = 5 \times 10^5$ K, solar chemical composition, $\log g = 7.5{-}9.5$), and (c) chemical composition ($T_{\rm eff} = 5 \times 10^5$ K, $\log g = 8.5$, chemical compositions of 0.25, 0.5, and 1 of the solar value). The spectra are averaged over intervals of 10 eV.

higher than 0.5 keV in an observed spectrum, variations in the interstellar absorption may be compensated by the joint influence of the normalization for the dilution of the flux and the effective temperature, which affects the slope of the spectrum. As a result, various combinations of these three parameters can yield statistically similar results. This is usually visible in a plot of confidence-level contours in the $N_{\rm H}$–$T_{\rm eff}$ plane (curves bounding zones within which the true parameter value is located with some probability) as a characteristic region of possible $T_{\rm eff}$ and $N_{\rm H}$ values (Fig. 3). As a rule, the upper left part of this zone is consistent with the Galactic value of $N_{\rm H}$ in the specified direction (we will call this the Galactic $N_{\rm H}$ value) and yields plausible luminosities for the source.

In connection with this, we estimated the errors in

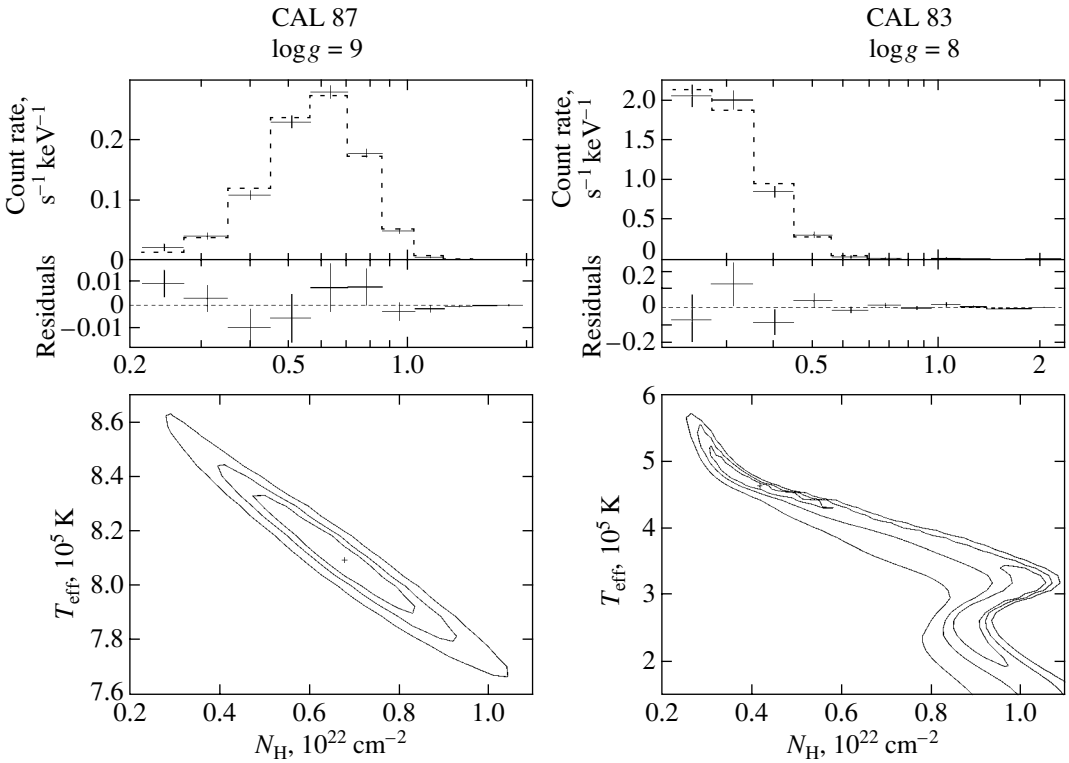

Fig. 3. Observed X-ray spectra for two of the studied sources together with the best-fitting theoretical spectra and the regions of admissible parameters in the N_H–T_{eff} plane corresponding to the surface gravities chosen for the analysis (see Section 6). Values of the "data–model" residuals are presented together with the spectra. The contours bound the 68, 90, and 99% probability zones, and the crosses mark the best-fit values. The source CAL 87 has a relatively hard spectrum, and its parameters are localized with certainty; CAL 83 has a soft spectrum, and the zone of allowed parameters in the N_H–T_{eff} plane is very extended.

T_{eff} and the normalization when limiting the column density N_H in the region of most plausible parameter values. We adopted the extreme values of the errors of T_{eff} and the normalization for two fixed values of N_H for the boundary values delimiting this region. We first determined the 90% probability boundaries for N_H. Then, we determined the errors in the two other parameters for two values of N_H—the minimum value of N_H and either the maximum value of N_H or double best fit, depending on which turned out to be closer to the best approximation. Observations for which errors were derived in this way are denoted in Tables 3 and 4 by the letters A and B in the "Type of errors" column. Statistically, these errors yield a probability of about 98% that the true value is within the error interval.

For several sources, the parameters were well constrained in the zone corresponding to the best-fit approximation. This is because the data for these sources were fairly hard, so that either the cutoff in their spectra is beyond 0.5 keV (RX J0513) or the maximum observed flux occurs at 0.7–0.9 keV (CAL 87 and RX J0925). In this case, we did not use the error-estimation method described above, and the parameter errors were calculated using the usual statistical criteria ($\Delta\chi^2 = 2.71$, 90% probability, type C in Tables 3 and 4).

Given the complexity of accurately estimating parameters, we attempted to determine the most general bounds for the possible parameter values. Most often, due to the impossibility of separating the influences of individual parameters, the magnitude of χ^2 remained virtually unchanged for any value of the surface gravity; however, different effective temperatures were naturally obtained for different surface gravities. Therefore, we present two approximations for nearly all the sources, corresponding to the lower and upper bounding values of the surface gravity.

In addition, very often, very broad limits for the column density N_H were allowed statistically. Our analysis (Section 6) showed that the Galactic column density [24] is located within the confidence intervals for most of the sources (located in the Large and Small Magellanic Clouds). Accordingly, we have included approximations for the source parameters obtained by fixing the column density to be the Galactic value (the errors were calculated in the usual way, error type C).

Table 3. Approximation parameters for the minimum $\log g$

Object	N_H, 10^{20} cm^{-2}	T_{eff}, 10^5 K	$\log g$ (cm s^{-2})	$\log(R/d)^2$	Flux (0.2–2 keV), erg cm^{-2} s^{-1}	χ^2/d. o. f.	Type of errors
RX J0439	$4.75^{+10.15}_{-4.67}$	$2.80^{+1.52}_{-0.70}$	7.5	$-26.63^{+5.29}_{-2.84}$	4.32×10^{-11}	9.30/8	A
RX J0513	$5.94^{+0.47}_{-0.40}$	$5.95^{+0.10}_{-0.07}$	$8.4^{+0.04}_{-0.15}$	$-28.57^{+0.10}_{-0.08}$	1.09×10^{-10}	19.4/8	C
RX J0527	$27.6^{+11.3}_{-24.25}$	$3.02^{+2.49}_{-1.81}$	8.0	$-23.43^{+10.00}_{-6.65}$	1.26×10^{-7}	1.47/8	A
CAL 87	$69.2^{+23.1}_{-22.0}$	$8.20^{+0.22}_{-0.24}$	9.0	$-28.20^{+0.85}_{-0.81}$	1.17×10^{-9}	13.5/8	C
CAL 83	$11.0^{+11.3}_{-6.46}$	$4.64^{+0.94}_{-0.64}$	8.0	$-27.59^{+2.17}_{-1.51}$	2.62×10^{-10}	16.1/8	B
1E 0035	$5.00^{+3.72}_{-2.34}$	$4.82^{+0.49}_{-0.29}$	8.0	$-28.89^{+0.80}_{-0.63}$	1.67×10^{-11}	6.69/8	C
	$3.83^{+3.13}_{-1.89}$	$4.96^{+0.54}_{-0.34}$	8.0	$-29.29^{+0.74}_{-0.56}$	8.16×10^{-12}	3.42/8	C
RX J0048	$27.6^{+10.5}_{-12.6}$	$3.35^{+0.55}_{-0.48}$	7.5	$-24.55^{+2.82}_{-2.50}$	3.09×10^{-8}	8.08/8	C
1E 0056	$12.1^{+7.00}_{-9.24}$	$2.69^{+0.95}_{-0.43}$	7.5	$-25.01^{+1.37}_{-3.82}$	1.20×10^{-9}	9.41/8	A
	$3.71^{+21.29}_{-2.38}$	$4.00^{+1.24}_{-0.97}$	8.0	$-28.85^{+2.02}_{-0.44}$	5.31×10^{-12}	13.2/8	B
RX J0019	$16.7^{+6.9}_{-13.35}$	$2.80^{+1.26}_{-0.35}$	7.5	$-23.62^{+2.82}_{-4.67}$	4.46×10^{-8}	18.1/8	A
RX J0925	163^{+14}_{-46}	$9.85^{+1.05}_{-0.37}$	9.5	$-26.23^{+0.59}_{-1.57}$	2.53×10^{-7}	8.85/8	C
AG Dra	$0.0595^{+0.0405}_{-0.0595}$	$3.09^{+0.41}_{-2.59}$	7.5	$-28.82^{+14.82}_{-0.18}$	7.67×10^{-13}	4.21/8	B

Note: Fluxes have been corrected for interstellar absorption.
Type of errors: A denotes error limits based on the limiting values of N_H (98%); B denotes error limits based on the left boundary of N_H and $2N_H$ for the best approximation (98%); C denotes errors derived from usual χ^2 criteria (90%).
The error for $\log g$ for RXJ0513 is 1σ; the remaining parameters were derived with this value fixed.
The data for AG Dra are approximate.

Table 4. Approximation parameters for the maximum $\log g$

Object	N_H, 10^{20} cm^{-2}	T_{eff}, 10^5 K	$\log g$ (cm s^{-2})	$\log(R/d)^2$	Flux (0.2–2 keV), erg cm^{-2} s^{-1}	χ^2/d. o. f.	Type of errors
RX J0439	$5.00^{+0.06}_{-5.00}$	$3.10^{+2.75}_{-0.88}$	9.5	$-26.79^{+1.81}_{-3.31}$	5.03×10^{-11}	9.31/8	A
RX J0513	Not given: one possible value of $\log g$						
RX J0527	$21.9^{+8.00}_{-18.55}$	$3.43^{+3.62}_{-0.22}$	9.5	$-25.10^{+2.03}_{-5.52}$	6.72×10^{-9}	1.47/8	A
CAL 87	Not presented: one possible value of $\log g$						
CAL 83	$10.6^{+24.4}_{-6.25}$	$5.65^{+1.48}_{-1.08}$	9.5	$-28.11^{+2.19}_{-1.51}$	2.16×10^{-10}	16.3/8	B
1E 0035	$4.62^{+3.54}_{-2.21}$	$5.93^{+0.75}_{-0.50}$	9.5	$-29.40^{+0.85}_{-0.65}$	1.44×10^{-11}	6.61/8	C
	$3.51^{+2.97}_{-1.77}$	$6.14^{+0.82}_{-0.53}$	9.5	$-29.79^{+0.72}_{-0.56}$	7.23×10^{-12}	3.44/8	C
RX J0048	$22.7^{+5.1}_{-9.2}$	$4.10^{+0.90}_{-0.63}$	9.5	$-25.88^{+1.71}_{-0.81}$	5.21×10^{-9}	9.35/8	C
1E 0056	$10.1^{+4.10}_{-8.07}$	$3.00^{+1.96}_{-0.56}$	9.5	$-25.81^{+2.46}_{-3.96}$	3.35×10^{-10}	9.82/8	A
	$3.28^{+17.42}_{-2.21}$	$4.59^{+1.97}_{-1.24}$	9.5	$-29.29^{+1.95}_{-1.20}$	4.26×10^{-12}	13.1/8	B
RX J0019	$11.7^{+6.20}_{-8.76}$	$3.31^{+2.04}_{-0.60}$	9.5	$-25.40^{+2.81}_{-3.57}$	2.39×10^{-9}	18.2/8	A
RX J0925	Not presented: one possible value of $\log g$						
AG Dra	$2.51^{+3.99}_{-2.51}$	$1.16^{+2.84}_{-0.66}$	9.5	$-20.96^{+4.66}_{-8.36}$	3.49×10^{-12}	4.20/8	A

Note: See comments for Table 3.

Table 5. Approximation parameters for the minimum $\log g$ and Galactic $N_{\rm H}$

Object	$N_{\rm H}$, 10^{20} cm^{-2}	$T_{\rm eff}$, 10^5 K	$\log g$ (cm s^{-2})	$\log(R/d)^2$	Flux (0.2–2 keV), erg cm^{-2} s^{-1}	χ^2/d. o. f.
RX J0439	5.60	$2.72^{+0.12}_{-0.15}$	7.5	$-26.24^{+0.35}_{-0.26}$	7.99×10^{-11}	9.30/9
RX J0513	7.24	$5.74^{+0.03}_{-0.03}$	8.4	$-28.29^{+0.02}_{-0.01}$	1.71×10^{-10}	33.8/9
RX J0527	6.31	$4.65^{+0.24}_{-1.12}$	8.0	$-29.18^{+0.83}_{-0.09}$	6.90×10^{-12}	2.17/9
CAL 87	7.58	Unsatisfactory approximation				
CAL 83	6.33	$5.04^{+0.17}_{-0.17}$	8.0	-28.57 ± 0.08	4.59×10^{-11}	17.3/9
1E 0035	6.94	$4.64^{+0.09}_{-0.11}$	8.0	-28.45 ± 0.06	3.62×10^{-11}	7.58/9
	6.94	$4.64^{+0.09}_{-0.13}$	8.0	$-28.56^{+0.08}_{-0.05}$	2.83×10^{-11}	6.10/9
RX J0048	4.24	Unsatisfactory approximation				
1E 0056	6.16	$2.90^{+0.09}_{-0.11}$	7.5	$-27.02^{+0.26}_{-0.22}$	2.56×10^{-11}	10.3/9
	6.16	$3.20^{+0.99?}_{-0.09}$	8.0	$-27.63^{+0.36}_{-0.86}$	1.85×10^{-11}	13.3/9
RX J0019	4.20	$3.57^{+0.24}_{-0.20}$	7.5	$-27.71^{+0.20}_{-0.22}$	3.61×10^{-11}	19.5/9
RX J0925	55.6	Unsatisfactory approximation				
AG Dra	3.08	$2.35^{+0.17}_{-0.16}$	7.5	$-26.41^{+0.46}_{-0.41}$	7.79×10^{-12}	4.73/9

Note: See comments for Table 3.

Table 6. Approximation parameters for the maximum $\log g$ and Galactic $N_{\rm H}$

Object	$N_{\rm H}$, 10^{20} cm^{-2}	$T_{\rm eff}$ 10^5 K	$\log g$ (cm s^{-2})	$\log(R/d)^2$	Flux (0.2–2 keV), erg cm^{-2} s^{-1}	χ^2/d. o. f.
RX J0439	5.60	$3.02^{+0.19}_{-0.20}$	9.5	$-26.47^{+0.37}_{-2.35}$	7.77×10^{-11}	9.31/9
RX J0513	7.24	Not presented: one possible value of $\log g$				
RX J0527	6.31	$5.60^{+0.37}_{-1.68}$	9.5	$-29.59^{+0.95}_{-0.14}$	6.84×10^{-12}	2.01/9
CAL 87	7.58	Not presented: one possible value of $\log g$				
CAL 83	6.33	$6.20^{+0.24}_{-0.25}$	9.5	$-29.01^{+0.09}_{-0.08}$	4.59×10^{-11}	17.1/9
1E 0035	6.94	$5.61^{+0.14}_{-0.27}$	9.5	$-30.88^{+0.11}_{-0.06}$	3.59×10^{-11}	7.95/9
	6.94	$5.60^{+0.14}_{-0.30}$	9.5	$-28.98^{+0.13}_{-0.06}$	2.81×10^{-11}	6.83/9
RX J0048	4.24	Unsatisfactory approximation				
1E 0056	6.16	$3.31^{+0.16}_{-0.20}$	9.5	$-27.37^{+0.35}_{-0.29}$	2.50×10^{-11}	10.3/9
	6.16	$3.65^{+0.87}_{-0.26}$	9.5	$-27.91^{+0.41}_{-0.77}$	1.81×10^{-11}	13.3/9
RX J0019	4.20	$4.06^{+0.29}_{-0.17}$	9.5	$-28.01^{+0.14}_{-0.21}$	3.47×10^{-11}	19.3/9
RX J0925		Not presented: one possible value of $\log g$				
AG Dra	3.08	$1.44^{+0.46}_{-0.23}$	9.5	$-22.49^{+1.46}_{-2.04}$	5.24×10^{-12}	4.22/9

Note: See comments for Table 3.

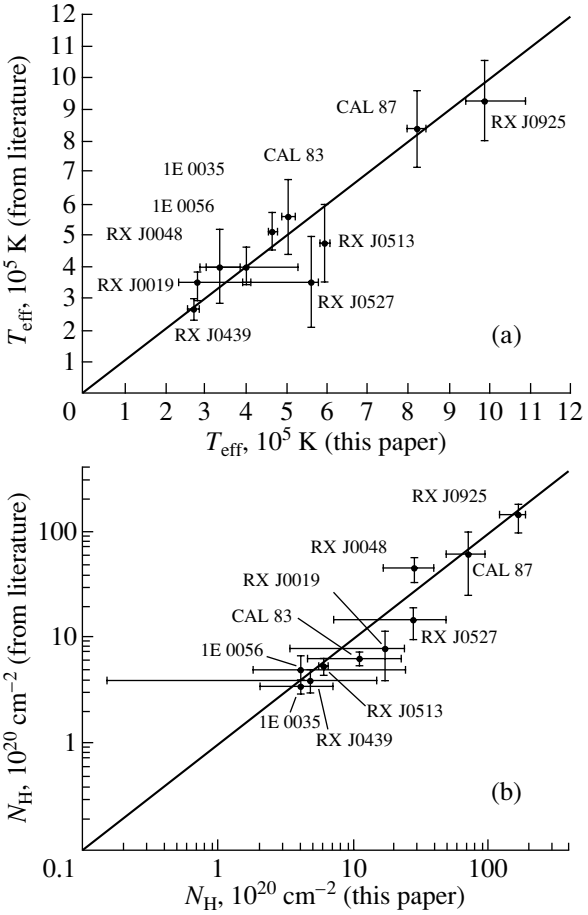

Fig. 4. Comparison of derived parameters with the data of other studies (references given in the text): (a) effective temperatures and (b) column densities of interstellar hydrogen.

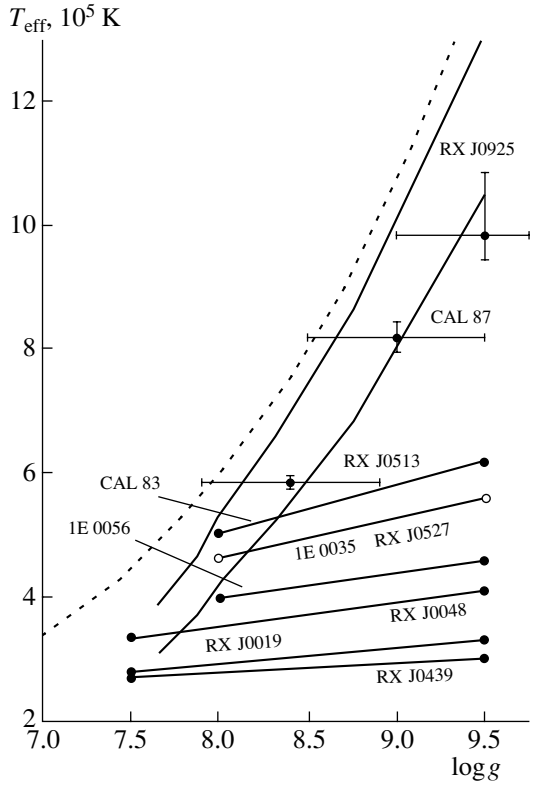

Fig. 5. Position of the studied sources in the $T_{eff}-\log g$ plane. The bold solid curves show the strip of stable burning. The dotted curve indicates the Eddington limit.

6. DISCUSSION

The approximation results are shown in Tables 3 and 4, which contain the approximation data for $\log g = 7.5$ and 9.5, and Tables 5 and 6, which contain the data for these surface gravities and the Galactic value of N_H. Figure 3 depicts the spectra and confidence contours for the surface gravities used in the analyses for two sources.

Figure 4 compares our results with the data of other authors. Figure 4a shows such a comparison for the effective temperatures. Our data for the minimum $\log g$ are shown for all the sources; for RX J0439, RX J0527, CAL 83, and 1E 0035, we have used the approximation with the Galactic N_H value, while N_H has been left as a free parameter for the other sources. Overall, the agreement is good, though we should point out a number of features.

First, the temperatures for RX J0527 and RX J0513 are approximately 100 000 K higher than those determined by other authors based on approximations of their spectra using Planck functions. Second, for the limiting values of T_{eff} for the two hardest sources CAL 87 and RX J0925, we used temperatures derived from non-LTE models (lower bounds) and unblanketed LTE models (upper bounds) [12, 15]. We can see that the non-LTE values are lower and the LTE values (for the non blanketed models) higher than our values. The remaining sources approximated by non blanketed LTE models also display somewhat higher temperatures than those we derived. Consequently, we conclude that including the effect of lines in the LTE models for the white-dwarf atmospheres leads to lower temperatures for the supersoft sources.

Figure 4b compares our values for N_H in the directions of the sources with previously published values. We adopted the extreme values from the literature data as the limiting values of N_H. If they were known, we used independent values of N_H derived from optical and ultraviolet observations. The figure shows our resulting values for the minimum $\log g$.

We used the data of the catalog [4], as well as from the following papers: 1E 0056—[28] (N_H), RX J0048—[28], 1E 0035—[29], RX J0019—[30], RX J0925—[31] (N_H).

The gravitational acceleration is poorly constrained. We were able to fix it well only for the three

sources with the highest temperatures: RX J0925, CAL 87 (the only possible value for them is $\log g = 9.5$), and RX J0513 ($\log g = 8.4^{+0.04}_{-0.15}$, errors shown are 1σ). The errors in their $\log g$ values in Fig. 5 were estimated to be ± 0.5. For the remaining sources, values of $\log g$ from the entire range of parameters for our model grid are statistically allowed. However, the model of van den Heuvel *et al.* [5] predicts a rigorous relation between $T_{\rm eff}$ and $\log g$, according to which stable hydrogen burning is possible without an appreciable increase in the white-dwarf radius only within a rather narrow range of accretion rates, called the stable-burning strip (SBS) [8–10]. The edges of the SBS depend on the mass of the white dwarf. When the accretion rate $\dot{M}$ is lower, matter will accumulate on the surface of the white dwarf, with subsequent explosive burning and the ejection of the accreting envelope (novae, recurrent novae, and symbiotic novae). At higher values of $\dot{M}$, there will be continuous stable hydrogen burning with a luminosity close to the Eddington luminosity. The excess matter will be blown out by the optically thick wind from the white-dwarf surface, leading to an increase in the effective radius of the photosphere and a decrease in the effective temperature [25]. Using the theoretical relation between the mass and radius of a white dwarf [26], we can reflect the SBS from the $\dot{M}-M$ [9] to the $T_{\rm eff}-\log g$ [27] plane. The SBS, Eddington limit, and positions of the sources in these coordinates are shown in Fig. 3. The three sources with well-defined values of $\log g$ lie inside the SBS (within the errors in the parameters). The temperatures of the remaining sources are also consistent with the SBS for the case of the minimum allowed surface gravity ($\log g = 7.5$–8).

The computations of models for white dwarfs with stable surface thermonuclear burning predict an increase in the photospheric radius in the SBS by a factor of two to three compared with the radius of a cool white dwarf [7, 9]. However, using source sizes exceeding the radius of a cool white dwarf of the given mass by a factor of two when reflecting the stable-burning strip onto the $T_{\rm eff}-\log g$ plane only leads to a shift of the strip downward to the left along the strip itself and the Eddington limit. Therefore, in this case, the conclusions drawn above that the sources are located in the stable-burning strip remain valid.

7. CONCLUSION

We have carried out an analysis of archival ROSAT observations of 11 known supersoft X-ray sources. We have derived the atmospheric parameters $T_{\rm eff}$ and $\log g$ for these sources by approximating their spectra using computed theoretical spectra for blanketed LTE models of hot white-dwarf atmospheres. The resulting parameter values are in agreement with values published previously.

In our paper [32], we will carry out an analysis of the parameters obtained from the point of view of their consistency with the theory of stable/recurrent burning; luminosity, mass, and radius estimates for seven sources; and a discussion of the effective temperature–mass relation.

8. ACKNOWLEDGMENTS

This work was supported by the Russian Foundation for Basic Research (project nos. 99-02-17488 and 02-02-17174). A. A. Ibragimov thanks the High-energy Astrophysics Department of the Space Research Institute of the Russian Academy of Sciences for hospitality during the time the work was being carried out.

REFERENCES

1. J. Trümper, G. Hasinger, and B. Aschenbach, *et al.,* Nature **349**, 579 (1991).
2. G. Hasinger, in *Reviews in Modern Astronomy,* Ed. by G. Klare (1994), Vol. 7, p. 129.
3. P. Kahabka and van den E. P. J. Heuvel, Ann. Rev. Astron. Astrophys. **35**, 69 (1997).
4. J. Greiner, New Astron. **5**, 137 (2000).
5. E. P. J. van den Heuvel, D. Bhattacharya, K. Nomoto, and S. Rappaport, Astron. Astrophys. **262**, 97 (1992).
6. B. Paczynski and A. Zytkow, Astrophys. J. **222**, 604 (1978).
7. I. Iben, Astrophys. J. **259**, 244 (1982).
8. K. Nomoto, Astrophys. J. **253**, 798 (1982).
9. M. Fujimoto, Astrophys. J. **257**, 767 (1982).
10. I. Iben and A. V. Tutukov, Astrophys. J., Suppl. Ser. **105**, 145 (1996).
11. J. Heise, A. van Teeseling, and P. Kahabka, Astron. Astrophys. **288**, L45 (1994).
12. H. Hartmann, J. Heise, P. Kahabka, C. Motch, and A. Parmar, Astron. Astrophys. **346**, 125 (1999).
13. I. Hubeny and T. Lanz, Astrophys. J. **439**, 875 (1995).
14. L. Anderson, Astron. Soc. Pac. Conf. Ser. **77** (1990).
15. H. Hartmann and J. Heise, Astron. Astrophys. **322**, 591 (1997).
16. F. Paerels, A. Rasmussen, H. Hurtmann, *et al.*, astro-ph/0011038 (2000).
17. R. Kurucz, Smithson. Astrophys. Obs. Spec. Rep. **309**, 1 (1970).
18. D. A. Verner, G. H. Ferland, K. T. Korista, and D. G. Yakovlev, Astrophys. J. **465**, 487 (1996).
19. J. Madej, Astron. Astrophys. **286**, 515 (1994).
20. D. A. Verner, E. M. Verner, and L. J. Ferland, Bull. Am. Astron. Soc. **188**, 54.18 (1996).
21. R. Kurucz and I. Furenlid, Smithson. Astrophys. Obs. Spec. Rep. **387**, 1 (1979).
22. L. Auer, J. Quant. Spectrosc. Radiat. Transf. **16**, 931 (1976).

23. E. Anders and N. Grevesse, Geochim. Cosmochim. Acta **53**, 197 (1989).
24. J. Dickey and F. Lockman, Ann. Rev. Astron. Astrophys. **28**, 215 (1990).
25. M. Kato, in *Supersoft X-Ray Sources,* Ed. by J. Greiner; Lect. Notes Phys. **472**, 15 (1996).
26. R. Popham and R. Narayan, Astrophys. J. **442**, 337 (1995).
27. A. van Teeseling, J. Heise, and P. Kahabka, in *IAU Symp. 165: Compact Stars in Binaries*, Ed. by J. van Paradijs, E. P. J. van den Heuvel, E. Kuulkers, *et al.* (Kluwer Academic, Dordrecht, 1996), p. 445.
28. P. Kahabka, W. Pietsch, and G. Hasinger, Astron. Astrophys. **288**, 538 (1994).
29. P. Kahabka, A. Parmar, and H. Hurtmann, Astron. Astrophys. **346**, 453 (1999).
30. K. Beuermann, K. Reinsch, H. Barwig, *et al.*, Astron. Astrophys. **294**, L1 (1995).
31. C. Motch, G. Hasinger, and W. Pietsch, Astron. Astrophys. **284**, 827 (1994).
32. V. F. Suleimanov and A. A. Ibragimov, Astron. Zh. **80**, 223 (2003) [Astron. Rep. **47**, 197 (2003)].

Translated by D. Gabuzda

Astronomy Reports, Vol. 47, No. 3, 2003, pp. 197–205. Translated from Astronomicheskiĭ Zhurnal, Vol. 80, No. 3, 2003, pp. 223–230.

Supersoft X-ray Sources: Basic Parameters

V. F. Suleĭmanov and A. A. Ibragimov

Kazan State University, Kazan, Tatarstan, Russia

Received March 5, 2002; in final form, October 10, 2002

Abstract—The parameters of ten supersoft X-ray sources observed by ROSAT obtained using blanketing approximations and LTE model atmospheres are analyzed. The consistency of the resulting parameters with a model with stable/recurrent burning on the surface of the white dwarf is studied. The luminosity and sizes of seven of the sources are in good agreement with this model. The masses of the white dwarfs in these sources are estimated. A formula that can be used to estimate the masses of white dwarfs in classical supersoft sources based on their effective temperatures is presented. © *2003 MAIK "Nauka/Interperiodica".*

1. INTRODUCTION

Supersoft X-ray sources are a class of X-ray object with very soft spectra (effective temperatures of the order of 10–80 eV) [1]. It is known that supersoft sources do not form a uniform class. Some are close binary systems with periods from tenths of days ($0^d.17$ for 1E0035—typical of the periods of cataclysmic variables) to several days ($1^d.04$ for CAL83).

The widely adopted classical model for these sources put forth by van den Heuvel *et al.* [2] (vdH92) proposed that they are close binary systems with a white dwarf and subgiant, in which material from the donor is accreting onto the white dwarf on the thermal time scale at a rate on the order of $10^{-7}\,M_\odot$/yr. At such accretion rates onto the white-dwarf surface, a regime of stable thermonuclear hydrogen burning is realized, without the substantial increase in the radius of the white dwarf predicted theoretically in [3–7]. However, this model also encounters certain difficulties. In particular, the radial velocities of the source CAL87 imply a mass for the secondary that is half that of the white dwarf, in contradiction with the expectations of the model [8].

Symbiotic stars with periods of hundreds of days ($\sim 550^d$ for AG Dra) are also found among supersoft sources. It is thought that, in these systems, there is accretion from the wind of a giant donor, with subsequent burning on the white-dwarf surface. It is likely that recurrent novae (such as U Sco [90]) also undergo a supersoft stage. The source RX J0439 in the Large Magellanic Cloud has not yet been demonstrated to be a binary. There are no signs of an accretion disk in its spectrum, so that it has been classified either as a single star at a very late stage of evolution or as a system of two degenerate dwarfs [10].

In all cases, the presence of soft X-ray emission is associated with thermonuclear burning on the surface of a white dwarf or a naked hydrogen or helium core of a star in a late stage of evolution.

In the first part of our current study [11], we approximated ROSAT spectra using blanketed LTE model atmospheres. Here, we analyze the consistency of those results with the theory of stable/recurrent burning on the surface of a white dwarf, estimate a number of physical parameters of the sources, and analyze their mass–effective temperature relation. The full designations of the sources are presented in Table 1. We will use shortened designations consisting only of the first several symbols.

2. POSITION OF SOURCES IN THE HERTZSPRUNG–RUSSELL DIAGRAM

In [11], we approximated archival ROSAT observations using blanketed LTE model atmospheres. For most sources, we obtained four different approximations: for the smallest and largest possible values of $\log g$ and with the column density of interstellar hydrogen either treated as a free parameter or fixed at the Galactic value (i.e., the value for the given direction in the Galaxy). The resulting source parameters are presented in Tables 3–6 of [11]: the column density of interstellar hydrogen $N_{\rm H}$, effective temperature $T_{\rm eff}$, logarithm of the gravitational acceleration $\log g$, and normalization factor R^2/d^2. Knowing the source parameters and distances d, we can find their luminosities and sizes:

$$L = 4\pi\sigma T_{\rm eff}^4 \frac{R^2}{d^2} d^2, \qquad R = \sqrt{\frac{R^2}{d^2}}\, d. \qquad (1)$$

We took the distances to the Large and Small Magellanic Clouds to be 50 and 60 kpc, respectively. We calculated the luminosities and sizes of sources in the Galaxy assuming $d = 2$ kpc.

1063-7729/03/4703-0197$24.00

Table 1. Approximation parameters

Object	$N_{\rm H}$, 10^{20} cm^{-2}	$T_{\rm eff}$, 10^5 K	$\log g$ (cm s^{-2})	$\log(R/d)^2$	Flux (0.2–2 keV), erg cm^{-2} s^{-1}	χ^2/d. o. f.
RX J0439.8-6809	5.60	$2.72^{+0.12}_{-0.15}$	7.5	-26.24 ($-26.50\ldots-25.89$)	7.99×10^{-11}	9.30/9
RX J0513.9-6951	7.24	$5.74^{+0.03}_{-0.03}$	8.4	-28.29 ($-28.30\ldots-28.27$)	1.71×10^{-10}	33.8/9
RX J0527.8-6954	6.31	$5.60^{+0.37}_{-1.68}$	9.5	-29.59 ($-29.73\ldots-28.64$)	6.84×10^{-12}	2.01/9
CAL 87	$69.2^{+23.1}_{-22.0}$	$8.20^{+0.22}_{-0.24}$	9.0	-28.20 ($-29.01\ldots-27.35$)	1.17×10^{-9}	13.5/8
CAL 83	6.33	$5.04^{+0.17}_{-0.17}$	8.0	-28.57 ($-28.65\ldots-28.49$)	4.59×10^{-11}	17.3/9
1E 0035.4-7230	6.94	$4.64^{+0.09}_{-0.13}$	8.0	-28.56 ($-28.61\ldots-28.48$)	2.83×10^{-11}	6.10/9
RX J0048.4-7332	$27.6^{+10.5}_{-12.6}$	$3.35^{+0.55}_{-0.48}$	7.5	-24.55 ($-27.05\ldots-21.73$)	3.09×10^{-8}	8.08/8
1E 0056.8-7154	$3.71^{+21.29}_{-2.38}$	$4.00^{+1.24}_{-0.97}$	8.0	-28.85 ($-29.29\ldots-26.83$)	5.31×10^{-12}	13.2/8
RX J0019.8+2156	$16.7^{+6.9}_{-13.35}$	$2.80^{+1.26}_{-0.35}$	7.5	-23.62 ($-28.29\ldots-20.8$)	4.46×10^{-8}	18.1/8
RX J0925.7-4758	163^{+14}_{-46}	$9.85^{+1.05}_{-0.37}$	9.5	-26.23 ($-27.80\ldots-25.64$)	2.53×10^{-7}	8.85/8

Note: The lack of an error for $N_{\rm H}$ means that this parameter was fixed at the Galactic value. The fluxes were corrected for interstellar absorption.

The positions of sources in the Hertzsprung–Russell (HR) diagram are shown in Fig. 1, which also depicts theoretical curves for white dwarfs of various masses with hydrogen burning on their surfaces. It is known [7] that the maximum luminosity of such a white dwarf depends substantially on its internal temperature, especially in the case of low-mass white dwarfs. The luminosity of a hot white dwarf whose temperature is comparable to the temperature in a shell with thermonuclear burning,

$$\frac{L}{L_\odot} = 60000\left(\frac{M}{M_\odot} - 0.52\right), \qquad (2)$$

is substantially lower than the luminosity reached in the case of thermonuclear burning on the surface of a cooled white dwarf,

$$\frac{L}{L_\odot} = 46\,000\left(\frac{M}{M_\odot} - 0.26\right). \qquad (3)$$

Since we do not know the temperatures of the white dwarfs in the studied sources *a priori*, we compared their positions in the HR diagram with evolutionary tracks for novae in the declining brightness phase, which corresponds to burning on the surfaces of cool white dwarfs [13] (Fig. 1a), and with tracks for burning on the surfaces of hot white dwarfs, above the edge of the stable-burning strip [7] (SBS; the zone in which there can be *continuous* burning; Fig. 1b). The horizontal part of the tracks reflects variations in the photospheric radius and effective temperature of the white dwarf with the luminosity remaining nearly constant at its maximum value, while the sloped part of the tracks (Fig. 1a) reflects variations in the luminosity as the temperature of the white dwarfs decreases, with the radius remaining constant.

Four sources (RX J0925, CAL 87, RX J0513, and 1E 0056) are located near turning points of the evolutionary curves for both cool and hot white dwarfs. This means that they are located in the SBS, and that their luminosities are close to the maximum values (without appreciable increases in the white-dwarf radii). Note that their positions correspond to curves for white dwarfs of various masses, depending on their internal temperatures (compare Figs. 1a and 1b). Three sources (CAL 83, RX J0527, and 1E 0035) are located on white-dwarf cooling curves below the SBS.

The positions of four sources (1E 0035, 1E 0056, CAL 83, and RX J0527) are shown for two values of $\log g$ (the lower left point corresponds to $\log g = 9.5$, and the upper right point to $\log = 8.0$). Since the parameters obtained for RXJ0048, RXJ0439, and RXJ0019 were either uncertain or do not agree with acceptable parameters for white dwarfs, these objects are shown only in Fig. 1a for the minimum value of $\log g$. The luminosity of RXJ0019 is very uncertain, but this source may be a white dwarf located in the SBS. RXJ0439 and RXJ0048 have luminosities higher than the Eddington luminosities of white dwarfs (a lower limit for the latter source is indicated).

The parameters obtained in [11] show a large scatter due to uncertainty in the interstellar absorption (determined by $N_{\rm H}$). However, independent estimates of $N_{\rm H}$ derived from ultraviolet observations

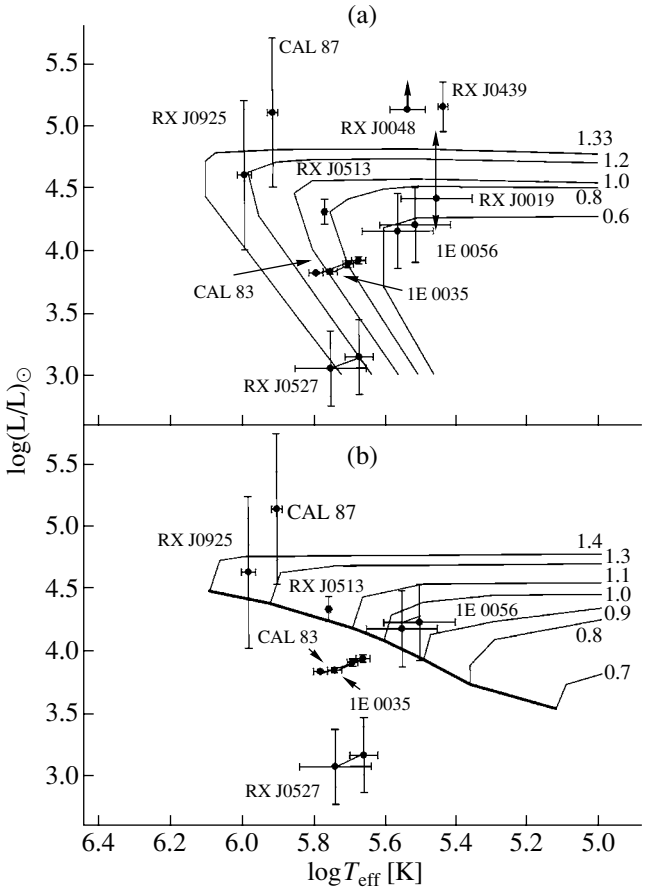

Fig. 1. Position of the sources in the Hertzsprung–Russell diagram. Theoretical relations for white dwarfs with hydrogen burning on their surfaces are also shown: (a) evolutionary tracks for novae in the declining brightness phase [13]; (b) theoretical curves for stable burning of hydrogen and helium on the surfaces of hot white dwarfs [7]. The bold solid curve shows the boundary of the stable-burning strip. The numbers near the curves indicate the white-dwarf masses in solar units.

are available for some of the sources, which testify that the values of $N_{\rm H}$ in the direction of the sources in the Magellanic Clouds differ little from the Galactic value. Therefore, we used the parameters for these sources obtained for the Galactic value of $N_{\rm H}$ (when this was possible). The values of the approximation parameters adopted to obtain the source characteristics are presented in Table 1. A basis for the choice of one or another approximation for each source is given below.

3. ESTIMATES OF THE SOURCE MASSES AND SIZES

Figure 2 shows the positions of the sources in the R–$\log g$ plane. The bold line presents the theoretical dependence for cool white dwarfs, while the dashed line presents the same dependence for the case when the white-dwarf radius is twice the theoretical value for a cool white dwarf. The circles in Fig. 2a show the positions of six sources: three with fixed values of $\log g$ (CAL 87, RX J0925, and RX J0513) and three whose sizes are very uncertain (RX J0019) or are not consistent with the sizes expected for white dwarfs (RX J0439 and RX J0048); only lower limits to the sizes of these last sources are indicated. The circles in Fig. 2b show the positions of the remaining four sources for the extreme values of $\log g$.

Let us analyze the positions of the sources in the HR diagram (Fig. 1) and in the $R-\log g$ plane (Fig. 2) taking into account available observational information, with the aim of estimating the masses of the white dwarfs in these objects. The mass can be derived from the source size as follows. We first determine the regions of $\log g$ values in Fig. 2 corresponding to the sizes of the sources, to the theoretical sizes of cool white dwarfs (solid line), and to sizes exceeding these theoretical sizes by a factor of two (dashed line; we will call this the "$2R$ case"). In this way, we find the $\log g$ values for which the theoretical curves correspond to the source sizes derived from observations. We can then find the mass of an object from the two $M-\log g$ relations, calculated from the

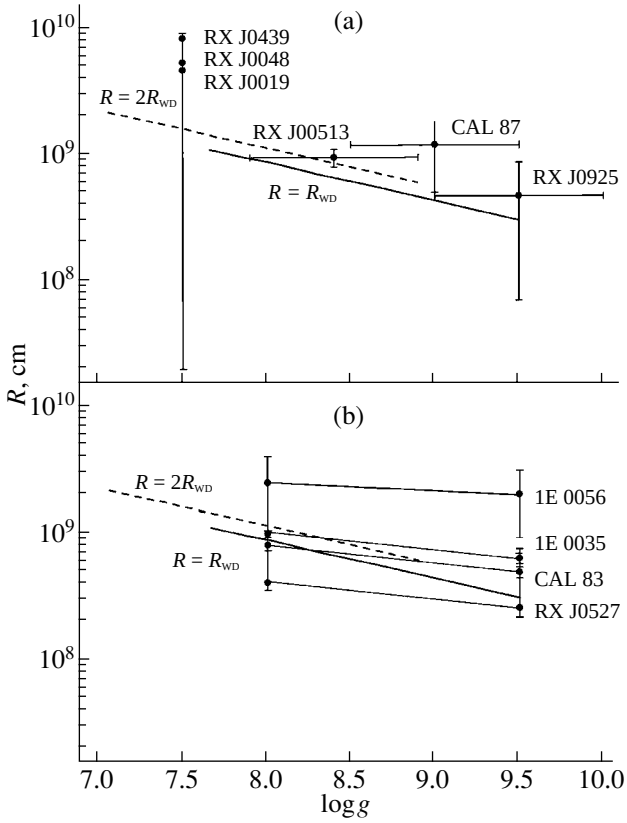

Fig. 2. Position of the sources in the $R-\log g$ plane: (a) with specified values of $\log g$ or sizes that are not consistent with those of white dwarfs; (b) with uncertain values of $\log g$. The solid curve shows the theoretical dependence for white dwarfs that follows from the mass–radius relation, and the dashed curve shows the same dependence for the case when the white-dwarf radius is doubled.

$M-R$ law for cool white dwarfs [14] and for objects with the same masses but doubled radii (Fig. 3).

RX J0439.8–6809. The size and luminosity of this source testify that it is not a classical supersoft source. In our analysis, we used the parameters derived for $\log g = 7.5$ and the Galactic $N_{\rm H}$ value, since $N_{\rm H}$ values derived independently using Hubble Space Telescope (HST) data [10] demonstrate the soundness of this approach. Two models are currently being considered for this source in the literature. It may be a system of two degenerate dwarfs, one of which overfills its Roche lobe, while thermonuclear burning occurs on the surface of the other [15], or it may be a star such as PG 1159, which is the virtually naked core of a star in a late stage of its evolution [10]. In either case, the spectrum of this source cannot be modeled using hydrostataic model atmospheres with solar chemical composition, and the parameter values we have obtained should be treated as very approximate. It is not possible to derive its mass from our data.

RX J0513.9–6951. This is a recurrent binary whose parameters are in agreement with the vdH92 model. The value of $N_{\rm H}$ has been derived using HST data [16], making it possible to determine its physical parameters. We used the parameters derived for the Galactic $N_{\rm H}$ value as upper limits for the luminosity and radius and a lower limit for $T_{\rm eff}$, and used the parameters derived allowing $N_{\rm H}$ to be free for the opposite limits. The location of the source in the HR diagram is near the turning points of evolutionary tracks with masses of $1.1-1.2\,M_\odot$ for hot and $0.8-0.9\,M_\odot$ for cool white dwarfs. Its size corresponds to the theoretical radius of white dwarfs with masses of $0.6-0.7\,M_\odot$, or $1-1.3\,M_\odot$ for the $2R$ case. The source size exceeds the size of a cool white dwarf, and its mass lies in the range $0.8-1.2\,M_\odot$.

RX J0527.8–6954. The X-ray flux from this object continually decreased in the 1990s, but the source was not detected by the Einstein satellite 20 years ago, although it was in its field of view [17, 18]. It thus appears that the source is recurrent and was in a declining brightness phase during the ROSAT observations. We used the parameters obtained for the Galactic $N_{\rm H}$, since the approximation data obtained when $N_{\rm H}$ was allowed to float are very uncertain. The source occupies the position of cooling curves for white dwarfs with masses of $1.2-1.4\,M_\odot$ in the

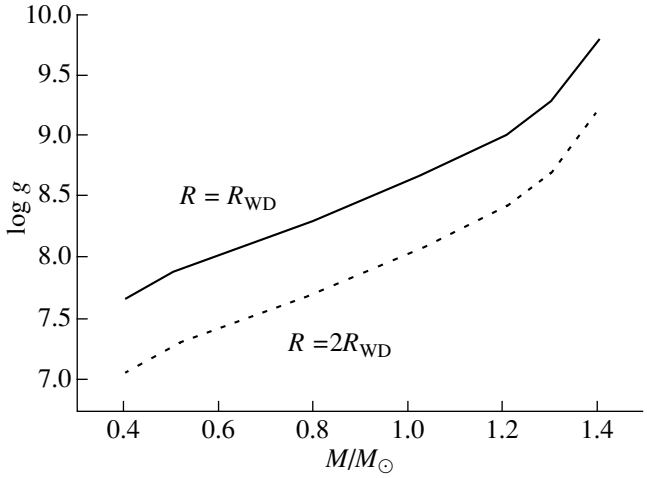

Fig. 3. Theoretical $M-\log g$ for cool white dwarfs (solid) and for objects with the same masses but doubled radii.

HR diagram. Its position in the $\log g-R$ plane is in better agreement with the relation for a cool white dwarf with $\log g = 9.5$, which yields a mass based on its size of $1.3-1.4\,M_\odot$. Thus, the $\log g$ of the source is fairly high (about 9.5) and its mass is in the range $1.2-1.4\,M_\odot$.

CAL 87. This object is an eclipsing binary system that has been studied by various authors and observed by various satellites [12, 19, 20]. The $N_{\rm H}$ value is appreciably higher than the Galactic value, presumably due to the fact that the orbital plane is strongly inclined to the line of sight, and the X-ray source is partially eclipsed by material above the plane of the disk. Its parameters are well defined, since it has a hard spectrum. The position of the object in the HR diagram suggests that the $N_{\rm H}$ value in the direction of the source may be overestimated, so that its luminosity and size are likewise overestimated. We therefore considered only the lower limits of these quantities. The source is located in the HR diagram in the SBS near white dwarfs with masses of $1.1-1.3\,M_\odot$. Its size is in agreement with theoretical radii of white dwarfs with masses lower than $1.05\,M_\odot$ ($1.3\,M_\odot$ for the $2R$ case). Consequently, the size of the source exceeds those of cool white dwarfs, and its mass is in the range $1.1-1.3\,M_\odot$.

CAL 83. This is a classical double supersoft source. We used the parameters obtained for the Galactic $N_{\rm H}$ value, since the absorption for this object derived from HST observations is close to this value [16]. The source is located in the HR diagram below the SBS on the cooling curves for white dwarfs with masses of $0.8-1.1\,M_\odot$ (for $\log g = 8.0-9.5$). Its position in the $\log g-R$ plane is in agreement with the size of a cool white dwarf with a low $\log g$ (about 8.0). The mass derived from the size corresponds to $0.6-0.8\,M_\odot$ ($1.2-1.3\,M_\odot$ for the $2R$ case). Thus, our estimates suggest the mass is close to $0.8\,M_\odot$.

1E 0035.4−7230. This is a cataclysmic variable that probably has a complex history [21]. We derived parameters for two separate observations, which are in good agreement with each other. We used the parameters obtained when approximating the April 28, 1002 observations using the Galactic $N_{\rm H}$ value. The source is located in the HR diagram below the SBS on cooling curves for white dwarfs with masses $0.8-1.0\,M_\odot$. Its size is in agreement with that for a cool white dwarf with a mass of about $0.75\,M_\odot$ ($1.25\,M_\odot$ in the $2R$ case). Consequently, the size and position of the source in the HR diagram indicate the low value $\log = 8.0$ and a mass of $0.7-0.8\,M_\odot$.

RX J0048.4−7332. This is a symbiotic novae that has been in a flaring stage since 1981 [23]. Our hydrostatic models yield high luminosities and sizes that are not consistent with the vdH92 model. However, models with winds ($\dot{M} \sim 10^{-5}-10^{-6} M_\odot/{\rm yr}$) yield reasonable estimates of the source's luminosity [22]. The parameters we have determined should be treated as estimates. We are not able to determine the source's mass.

1E 0056.8−7154. This is the nucleus of the planetary nebula N67. We obtained parameters for two observations that were not in good agreement, although the confidence contours for the two observations are consistent with each other; i.e., there is a high probability that the parameters obtained from the second observation are also possible for the first observation. In our analysis, we used the parameters derived for the October 7, 1993 observation leaving $N_{\rm H}$ free to vary with $\log g = 8.0$. The object is located in the SBS for white dwarfs with masses of $0.9-1.1\,M_\odot$ (hot white dwarfs) and $0.5-0.8\,M_\odot$ (cool white dwarfs). Its size exceeds the sizes of cool white dwarfs and

Table 2. Estimates of physical parameters of the sources

Source	$T_{\rm eff}$, 10^5 K	$\log g$	R, 10^8 cm	$M/M_\odot$	$L_{\rm bol}$, 10^{37} erg/s
RX J0513	5.85 ± 0.1	8.0–8.5	8–12	0.8–1.2	5.5–9.5
RX J0527	$5.60^{+0.37}_{-1.68}$	9.0–9.5	2.5–4	1.2–1.4	0.4–0.9
CAL 87	8.2 ± 0.25	8.5–8.75	5–9	1.1–1.3	7.5–20
CAL 83	5.04 ± 0.17	8.0–8.25	7–9	0.7–0.9	2.8–3.1
1E 0035	4.64 ± 0.1	7.7–7.9	8–10	0.65–0.85	3–3.3
1E 0056	4 ± 1	7.7–8.5	10–28	0.85–1.05	2.4–8
RX J0925	$9.85^{+1}_{-0.4}$	8.5–9.5	5–9	1.2–1.4	4–20

is consistent with the $2R$ case if the mass is lower than $1.0\,M_\odot$. It is probable that the white dwarf is hot, has recently formed (the planetary nebula), and has a mass of 0.9–$1.1\,M_\odot$.

RX J0019.8+2156 or QR And. This is a Galactic supersoft source. We used the parameters obtained leaving the $N_{\rm H}$ value free with $\log g = 7.5$, since the parameters derived for the Galactic $N_{\rm H}$ value yield a very low luminosity ($\sim 2 \times 10^{34}$ erg/s d(kpc)^2) and size (4×10^7 cm d(kpc)) for the source. The results are very uncertain, but in good consistency with the vdH92 model. We are not able to estimate the source mass using the available data.

RX J0925.8–6809. This is also a Galactic supersoft source located behind a molecular cloud in Vela, so that it is strongly reddened ($E(B-V) = 2.1$) [24]. We adopted a distance of 2 kpc, since this yields good agreement with the vdH92 model. In this case, the source is located above the SBS, and its mass is 1.2–$1.4\,M_\odot$. Its size is also consistent with this mass estimate (larger than $0.95\,M_\odot$ for a cool white dwarf and larger than $1.25\,M_\odot$ for the $2R$ case). The size of the white dwarf is larger than expected for a cool white dwarf.

Thus, we have estimated the white-dwarf masses and the most probable values of the remaining physical parameters for seven supersoft sources (Table 2). Of these, four sources (CAL 87, RX J0925, 1E0056, and RX J0513) were in the SBS at the epoch of observation, with their sizes exceeding those of cool white dwarfs. The remaining three sources (CAL 83, RX J0527, and 1E0035) were below the SBS on white-dwarf cooling curves, with their sizes consistent with those of cool white dwarfs.

We conclude that the physical characteristics of classical supersoft sources are consistent with the model of stable or recurrent thermonuclear burning on the surface of a white dwarf and that these sources occupy positions in the HR diagram either near the turning points of evolutionary tracks for this model or lower, on white-dwarf cooling curves.

4. MASS–TEMPERATURE RELATION

Let us investigate the relation between the effective temperature of the supersoft sources and the corresponding white-dwarf masses. It is known [7] that the luminosity of a white dwarf with thermonuclear burning on its surface is located on the horizontal section, or plateau, of the theoretical curves in the HR diagram associated with their mass [formulas (2) and (3)]. Using a linear approximation for the mass–radius dependence for white dwarfs and relation (3) between the luminosities and masses of white dwarfs, Iben and Tutukov [7] derived the dependence of the maximum possible effective temperature $T_{\rm eff}$ on the white-dwarf mass:

$$T_{\rm eff} = 3.6 \times 10^5\ {\rm K} \frac{(M/M_\odot - 0.26)^{1/4}}{(1 - 0.59 M/M_\odot)^{1/2}}, \quad (4)$$

shown in Fig. 4 by the dotted curve. This formula was derived assuming that the maximum temperature is reached when the luminosity is half the luminosity on the plateau (3), and the photospheric radius is double the radius of the white dwarf.

This same figure presents the positions of the four sources located in the SBS and two theoretical dependences. The upper curve is constructed from the positions of the maximum-temperature points for the evolutionary tracks of novae in the declining brightness phase [13], and the lower curve from the positions of these points for hot white dwarfs with a shell burning source [7]. It is clear that the formula proposed in [7] does not provide a good description of the relation between the mass and maximum temperature of the supersoft sources, although its underlying principle remains correct. We attempted to improve this formula by allowing for the fact that the mass–radius relation for white dwarfs is not linear, and the ratio of the size of the photosphere of a supersoft source to the radius of the corresponding cool white dwarf could depend on its mass. We accordingly approximated the

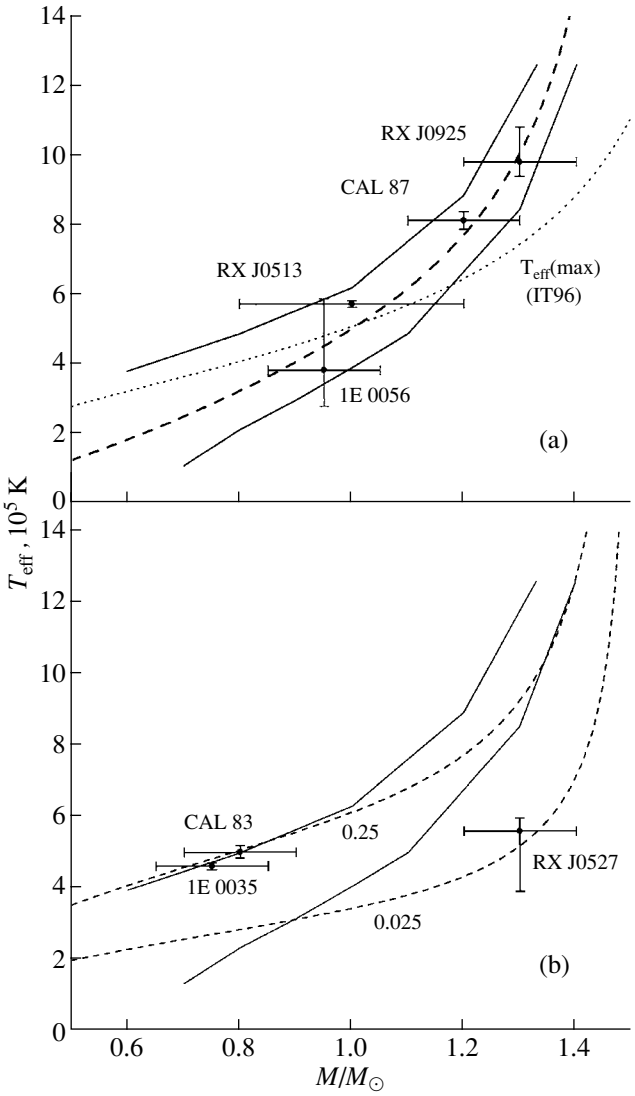

Fig. 4. Position of the studied sources in the $T_{\rm eff}$–M plane. (a) Position of sources in the stable-burning strip. The dotted curve labeled IT96 corresponds to the theoretical relation proposed by Iben and Tutukov [7]. The solid curves show relations between the maximum temperatures and masses of white dwarfs following from numerical computations of brightness declines of novae [13] (upper curve, compare with Fig. 1a) and of stable hydrogen and helium burning on the surfaces of hot white dwarfs [7] (lower curve, compare with Fig. 1b). The dashed curve depicts the relation of 6, which we proposed to estimate the masses of white dwarfs with supersoft sources located in the stable-burning strip. (b) Position of sources located on white-dwarf cooling curves. The dashed curves show the dependence of the source temperature on the white-dwarf mass if its radius is equal to the radius of a cool white dwarf with this mass and its luminosity comprises a constant fraction of the luminosity on the plateau (3). The numbers near the curves indicate the luminosity as a fraction of the maximum luminosity on the plateau.

mass–radius relation using a third-order polynomial:

$$\frac{R}{R_\odot} = 0.0273 - 0.0417\frac{M}{M_\odot} + 0.0364\left(\frac{M}{M_\odot}\right)^2 - 0.0138\left(\frac{M}{M_\odot}\right)^3 \quad (5)$$

and used this in place of the linear relation. However, this significantly influenced the results only for white dwarfs with masses higher than $1.2\,M_\odot$. Analysis of the ratio of the photospheric radius to the white-dwarf radius indicated that, in order to construct the best approximation to the results of the computations of surface thermonuclear burning, this ratio should be inversely proportional to the square of the white-dwarf mass.

Accordingly, we propose the following formula for the relation between the mass of a white dwarf and its effective temperature in the region of the SBS:

$$T_{\rm eff} = 3 \times 10^5 \frac{M/M_\odot (M/M_\odot - 0.26)^{0.25}}{(1 - 1.53M/M_\odot + 1.33(M/M_\odot)^2 - 0.51(M/M_\odot)^3)^{0.5}}. \quad (6)$$

This relation is shown in Fig. 4a by the dashed curve. We can see that it provides a good approximation to the results of the numerical computations. It was obtained assuming that the luminosity of the white dwarf is half the luminosity on the plateau, and the photospheric radius is a factor of $2(M_\odot/M)^2$ larger than the white-dwarf radius. We note that this is only a suggestion for the required relation, and the actual relation at the boundary of the SBS could be more complex.

Figure 4b shows the positions of the remaining three sources (CAL 83, 1E 0035, and RX J0527) in the $M-T_{\rm eff}$ plane. The solid curves depict the dependences of the maximum temperature on the white-dwarf mass that follow from the numerical computations (the same as in Fig. 4a). The dashed curves represent the relationships between the effective temperatures and masses of white dwarfs for sources with radii equal to the radii of cool white dwarfs and luminosities that are factors of 4 to 40 lower than the maximum possible luminosity (3). The numbers near the curves indicate the ratio of the luminosity of the white dwarf to the maximum luminosity. The degree of cooling of these three sources at the observation epoch and the influence of the nonlinearity of the mass–radius relation for white dwarfs are evident (compare the dotted curve in Fig. 4a and the dashed curves in Fig. 4b).

5. CONCLUSION

We have analyzed archival ROSAT observations of 10 known supersoft X-ray sources, and investigated the source parameters obtained in the first part of our study [11] to test for consistency with the model of thermonuclear hydrogen burning on the surface of a white dwarf (vdH92). The values of $T_{\rm eff}$ and $\log g$ obtained for the three hottest sources are consistent with those expected for the stable-burning strip in this model. The parameters of the remaining sources are consistent with those expected for this strip if the lowest possible values of $\log g (7.5–8.0)$ are adopted.

We have estimated the sizes and luminosities of ten sources. The sizes and luminosities of two sources (RX J0048 and RX J0439) are not consistent with those for hot white dwarfs, confirming earlier conclusions of other studies that hydrostatic white-dwarf model atmospheres with solar chemical composition are not suitable for these sources. The parameters of another source (RX J0019) are very uncertain, although they lie in the range of admissible parameters for the hot white-dwarf model.

The sizes and luminosities of seven classical supersoft sources are in good agreement with the vdH92 model, enabling us to estimate their masses from their sizes and positions in the HR diagram. We considered the dependence of $T_{\rm eff}$ on the mass of the white dwarfs in these supersoft sources and have proposed a formula that can be used to estimate the mass of a white dwarf in a classical binary supersoft source from its temperature.

6. ACKNOWLEDGMENTS

This work was supported by the Russian Foundation for Basic Research (project nos. 99-02-17488 and 02-02-17174).

REFERENCES

1. P. Kahabka and E. P. J. van den Heuvel, Ann. Rev. Astron. Astrophys. **35**, 69 (1997).
2. E. P. J. van den Heuvel, D. Bhattacharya, K. Nomoto, and S. Rappaport, Astron. Astrophys. **262**, 97 (1992).
3. B. Paczynski and A. Zytkow, Astrophys. J. **222**, 604 (1978).
4. I. Iben, Astrophys. J. **259**, 244 (1982).
5. K. Nomoto, Astrophys. J. **253**, 798 (1982).
6. M. Fujimoto, Astrophys. J. **257**, 767 (1982).
7. I. Iben and A. V. Tutukov, Astrophys. J., Suppl. Ser. **105**, 145 (1996).
8. A. Cowley, P. Schmidtke, D. Crampton, and J. Hutchings, Astrophys. J. **504**, 854 (1998).
9. P. Kahabka, H. Hartmann, A. Parmar, and I. Negueruela, Astron. Astrophys. **347**, L43 (1999a).
10. B. Gänsicke, A. van Teeseling, K. Beuermann, and K. Reinsch, New Astron. Rev. **44**, 143 (2000).
11. A. A. Ibragimov, V. F. Suleimanov, A. Vikhlinin, and N. A. Sakhibullin, Astron. Zh. **80**, 212 (2003) [Astron. Rep. **47**, 186 (2003)].
12. H. Hartmann and J. Heise, Astron. Astrophys. **322**, 591 (1997).
13. M. Kato and I. Hachisu, Astrophys. J. **437**, 802 (1994).
14. R. Popham and R. Narayan, Astrophys. J. **442**, 337 (1995).
15. I. Iben and A. V. Tutukov, Astrophys. J. **418**, 343 (1993).
16. B. Gänsicke, A. van Teeseling, K. Beuermann, and D. De Martino, Astron. Astrophys. **333**, 163 (1998).

17. J. Greiner, G. Hasinger, and P. Kahabka, Astron. Astrophys. **246**, L17 (1991).
18. J. Greiner, R. Schwarz, G. Hasinger, and M. Orio, Astron. Astrophys. **312**, 88 (1996).
19. A. Parmar, P. Kahabka, H. Hartmann, *et al.*, Astron. Astrophys. **323**, L33 (1997).
20. K. Asai, T. Dotani, F. Nagase, *et al.*, Astrophys. J. **503**, L143 (1998).
21. P. Kahabka and E. Ergma, Astron. Astrophys. **318**, 108 (1997).
22. S. Jordan, W. Schmutz, B. Wolff, *et al.*, Astron. Astrophys. **346**, 897 (1996).
23. D. Morgan, Mon. Not. R. Astron. Soc. **258**, 639 (1992).
24. C. Motch, G. Hasinger, and W. Pietsch, Astron. Astrophys. **284**, 827 (1994).

Translated by D. Gabuzda

Astronomy Reports, Vol. 47, No. 3, 2003, pp. 206–213. Translated from Astronomicheskiĭ Zhurnal, Vol. 80, No. 3, 2003, pp. 231–238.

The Herbig Ae/Be Star HD 200775 as a Spectroscopic Binary

N. Z. Ismailov

Shemakha Astrophysical Observatory, National Academy of Sciences of Azerbaijan, Shemakha, 373243 Azerbaijan

Received May 20, 2002; in final form, August 21, 2002

Abstract—New spectroscopic observations obtained in 1998–2001 and published radial velocities of neutral helium absorption lines suggest that the Herbig Ae/Be star HD 200775 is a spectroscopic binary with a 1180 ± 60 day period. We have determined the elements of the spectroscopic orbit. The presence of both rapid and long-time-scale spectral variability is demonstrated. The rapid variability is apparently due to a nonuniform circumstellar environment and modulation by the axial rotation of the system's primary. Using data from the literature, we plot the V light curve of the system, which shows some brightening near the time of the minimum radial velocity, with its duration not exceeding 0.2 of the orbital cycle. We suggest that the system's secondary is a low-mass ($\geq 0.5 M_\odot$) protostar, and that a semitransparent extended circumstellar envelope gives rise to eclipses in the system. © *2003 MAIK "Nauka/Interperiodica"*.

1. INTRODUCTION

The main features of the star HD 200775 (MWC 361) were already noted in the first review of Herbig Ae/Be stars [1]. According to Mendoza [2], this reddened B3e star is located in the reflection nebula NGC 7023, which also contains about 15 more known T Tauri stars having H_α emission and low-luminosity IR sources [3, 4], along with regions of dense CO associated with bipolar outflows [5] and an OH maser emitting at 1667 MHz [6]. The star has comparatively narrow hydrogen emission lines with central absorption features, which apparently display variable shifts. Weak [FeII] line emission attributed to the spectrum of an envelope is observed [7].

According to [8–10], the star's photospheric spectral type can be estimated to be B3IV-Ve. Emission in the Paschen series (P_{12}–P_{17}), in the OI λ8446 Å line, and in the lines of the CaII $\lambda\lambda$8948, 8542, 8662 Å triplet are observed in the near IR [7, 10].

According to Viotti [7], the star's hydrogen Balmer emission demonstrates variable intensity ratios of the violet and red components of the lines, V/R, that are correlated with the displacement of the central absorption. Variations of the line intensities and profiles on time scales of about a month were revealed in [9, 11–13]. Ruusalepp [14] notes variations of parameters of the H_β line with a period of about 200 days. More rapid changes in the H_α and H_β lines were found in [11, 15]. Miroshnichenko *et al.* [16] demonstrated that the equivalent width of the H_α line varies with a 3.68-year period, with the star's activity in this line reaching its maximum in 1997.

Ismailov [17] presented preliminary results of his study of various lines in the star's spectrum. He demonstrated the presence of significant line-profile variations for H_α, H_β, and HeI with time scales from an hour to several years and concluded that the star was probably a spectroscopic binary [17, 18].

In the system of the "General Catalogue of Variable Stars" (GCVS), the star has the designation V380 Cep. Suspected as a variable already in the 19th century [19], it was included in the GCVS as a low-amplitude variable more than 90 years later on the basis of the data of [13].

This paper presents new spectroscopic observations of the Herbig Ae/Be star HD 200775 acquired over the last four years, along with conclusions derived from their analysis.

2. OBSERVATIONS AND RESULTS

Our spectroscopic observations were made with an échelle spectrometer at the Coudé focus of the 2 m telescope of the Shemakha Astrophysical Observatory, National Academy of Sciences of Azerbaijan, equipped with a 530×580 pixel CCD detector. The $\lambda\lambda$4400–6800 Å spectral range was divided into 40 orders, with 35–50 Å from each used in the reduction. The spectral resolution was $R = 30\,000$. The readout and reduction of the spectra were performed using software developed at the Special Astrophysical Observatory of the Russian Academy of Sciences [20]. The instrument and observing techniques are described fully in [21].

The mean exposure time was 20 min, with the signal-to-noise ratio in the region of the H_α line being

1063-7729/03/4703-0206$24.00

Table 1. Parameters of the H_α line in the spectrum of HD 200775

JD 2450000+	W_λ, Å	V_{r1}, km/s	V_a, km/s	V_{r2}, km/s	$\Delta\lambda_{1/2}$, Å	I_1/I_2
1020.4792	66.58	−75.1	−14.0	70.8	6.67	1.06
1020.4875	55.70	−75.0	−10.0	70.0	6.70	1.07
1024.4896	63.82	−73.0	−13.0	88.0	6.56	1.13
1024.4972	59.25	−60.0	−11.0	104.0	6.34	1.01
1036.3431	73.10	−62.3	−14.0	81.0	6.76	1.02
1036.3653	74.48	−62.0	−9.7	56.1	7.10	1.07
1036.3819	48.30	−61.0	−3.1	85.0	7.56	1.01
1036.3958	59.10	−62.3	−5.4	85.5	6.81	1.18
1054.4618	63.80	−73.0	−13.0	88.0	6.56	1.10
1054.4694	72.01	−76.6	−11.0	87.0	6.89	1.11
1769.3556	52.70	−73.6	−9.1	45.6	6.41	1.14
1769.3729	60.90	−54.7	−5.0	63.9	6.26	1.09
1770.2604	55.60	−71.5	−6.8	44.2	6.18	1.16
1770.2882	57.40	−72.6	−7.6	44.1	6.14	1.15
1770.3174	53.50	−73.3	−6.9	43.9	6.28	1.19
1770.3319	55.60	−69.3	−6.1	45.1	6.35	1.17
1771.2465	53.50	−64.5	−6.9	41.7	6.47	1.23
1771.2625	46.30	−69.1	−6.7	42.1	6.48	1.20
2066.3388	65.60	−72.1	−9.5	61.1	6.40	1.10
2067.2923	66.50	−73.6	−10.3	55.5	6.30	1.04
2067.3131	67.20	−72.8	−12.7	53.1	6.40	1.00
2067.3284	68.10	−73.8	−10.9	58.7	6.50	1.10
2083.3000	79.50	−84.1	−6.6	49.8	6.50	1.01
2083.3104	80.90	−83.7	−4.9	47.1	6.40	1.02
2084.2979	103.78	−84.3	−8.0	35.0	6.60	1.01
2084.3097	91.40	−79.6	−8.7	35.2	6.50	1.03
2113.4569	89.20	−77.9	−11.2	49.4	6.30	1.02
2113.4708	72.10	−77.3	−9.3	50.0	6.60	1.02
2157.2687	65.50	−72.6	−7.3	38.1	6.40	1.10
2157.2798	71.45	−70.7	−6.5	37.9	6.30	1.03

$S/N \approx 150$. In the blue part of the spectrum, near the HeI $\lambda\lambda$4471, 4387 Å lines, the signal-to-noise ratio did not exceed 40. The mean uncertainty of our radial-velocity measurements derived from narrow absorption lines of standard stars is ±0.5 km/s. The emission lines have a complex multicomponent structure, so that the uncertainty of our V_r measurements for these lines could be as high as ±1 km/s. The relative rms error in the relative equivalent widths was up to 6–8% and was 0.5% for the central residual intensities. Our observations cover the time interval from 1998 to 2001, with a total of 30 spectrograms obtained. Table 1 presents the results of our measurements of parameters of the H_α line.

As was demonstrated in [3, 17], the profiles of

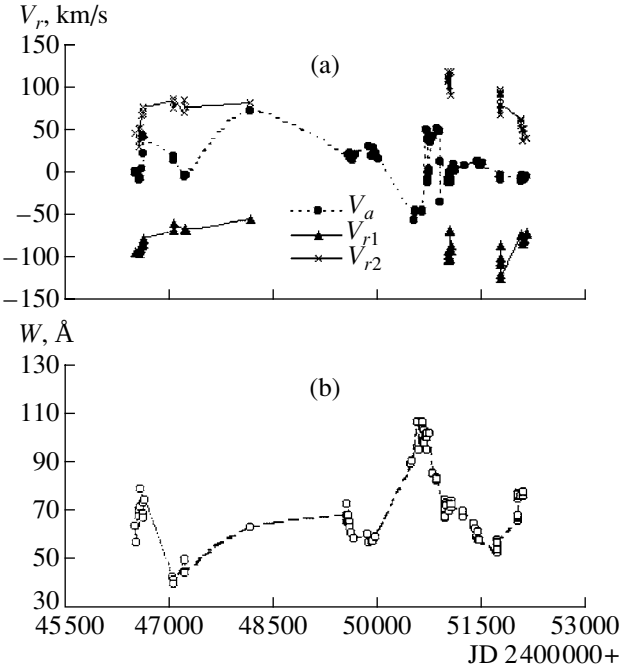

Fig. 1. Time dependence of the parameters of the H_α line.

the H_α and H_β lines show a two-component saddle shape. Various authors have measured a variety of characteristics of the hydrogen-line components, and we accordingly give only those hydrogen-line parameters measured by us that were also derived by all other authors in Table 1. These are the radial velocity of the central absorption V_a, the radial velocities of the blue and red components V_{r1} and V_{r2}, the total emission equivalent width W(Å), and the ratio of the central intensities of the blue and red components I_1/I_2. Table 1 also contains the values of $\Delta\lambda_{1/2}$ corresponding to the line half-widths (the full width at half maximum, FWHM).

To make our analysis of data on the H_α line as complete as possible, we used all data available in the literature. Some of the existing H_α data were presented by Beskrovnaya *et al.* [22]. Pogodin *et al.* [23] collected all H_α measurements acquired at various observatories prior to 2000.

Figure 1 displays the variations in the parameters of the H_α line derived from all published data from 1986 until the present, including our data from Table 1. The parameter V_a in Fig. 1a is the radial velocity of the H_α absorption. This figure demonstrates long-term variability of all the displayed spectroscopic parameters.

The radial-velocity measurements for the line's blue and red components are not numerous and do not show any definite variation pattern over the entire observation interval. Nevertheless, there is no doubt that they are variable; it appears that the displacements of these components sometimes vary synchronously with the variations of other parameters. In addition to the long-term variations, short-time-scale variations of the line parameters within individual nights are also observed.

We presented the H_β profiles in [16]. This line's central absorption divides the H_β emission completely into two peaks, right to the continuum level. Therefore, we measured all the spectroscopic parameters individually for the line's two components. Our measurements show that variations of the intensity ratio of the blue and red components are sometimes present. Table 2 contains the parameters of the H_β line; the subscripts 1 and 2 refer to data for the blue and red components, respectively. We can see from the last column of the table that, as a rule, the W_1/W_2 ratio exceeds unity, though ratios less than unity are also observed from time to time.

Our studies [17, 18] based on 20 years of observations of the H_α line suggested the presence of an eight-year variability period. The period is especially good at reproducing the full equivalent widths of the H_α line. As noted by Pogodin *et al.* [23], the central absorption is sometimes split into several components, so that the measured H_α-absorption radial velocities can disagree with the actual displacement of the star's center of mass.

We also measured the spectroscopic parameters of the strongest HeI lines, $\lambda\lambda$4387, 4471, 5876, 6678 Å. The values of V_r, W_λ, and FWHM for all the measured lines are collected in Table 3. Note that the region of the HeI λ5876 Å line was outside the spectral range covered by the CCD chip in our 1998 observations. The parameters of the HeI lines showed variability from season to season. Simultaneous changes were observed in the line profiles. As an example, Fig. 2 shows the profiles of the HeI λ6678 Å line obtained in 1998 (left) and in 2000 (right). In 1998, the line profiles appear asymmetric, with the blue wing being steeper than the red wing. In contrast, the red wing was steeper in 2000.

There is a substantial amount of data in the literature only for the HeI λ5876 Å line. These data, with our results added, can be used to conduct a frequency analysis to search for periodicities. We used Scargle's method [24], which was later improved by Horne and Baliunas [25]. The code for the period-search algorithm was written by I. I. Antokhin, and some methodical questions connected with the algorithm's application are discussed in detail in [26].

We used a total of 71 observations for our frequency analysis of the radial velocities of the HeI λ5876 Å absorption line. Figure 3a shows the power spectrum for the frequency range 0–0.02 d^{-1}, and

Table 2. Parameters of the H_β line in the spectrum of HD 200775

JD 2450000+	W_1, Å	W_2, Å	V_{r1}, km/s	V_a, km/s	V_{r2}, km/s	$(\Delta\lambda_{1/2})_1$, Å	$(\Delta\lambda_{1/2})_2$, Å	W_1/W_2
1020.4792	1.53	1.97	−101.3	10.0	107.8	2.44	3.13	0.78
1020.4875	1.50	1.90	−103.0	6.0	107.0	2.40	3.10	0.79
1024.4896	1.71	1.73	−91.4	14.0	116.0	2.73	3.55	0.99
1024.4972	1.48	1.62	−96.3	16.2	104.0	2.35	2.49	0.91
1036.3431	1.50	1.50	−101.0	12.0	94.0	1.36	3.85	1.00
1036.3653	1.70	1.79	−68.0	9.0	115.0	1.70	1.40	0.95
1036.3819	1.52	1.47	−101.9	2.0	93.3	2.54	2.80	1.03
1036.3958	1.69	1.79	−68.5	12.0	114.7	2.26	2.90	0.94
1054.4618	1.67	1.74	−91.4	14.0	116.0	2.74	3.55	0.96
1054.4694	1.76	1.74	−84.6	3.2	88.6	2.49	2.26	1.01
1769.3556	0.96	0.92	−104.0	−18.0	72.1	2.29	2.08	1.04
1769.3729	1.14	1.06	−107.3	−16.5	72.6	1.72	2.02	1.08
1770.2604	1.10	0.92	−119.0	−14.0	95.0	2.98	1.99	1.20
1770.2882	1.01	1.02	−85.2	−15.0	90.8	2.04	1.78	0.99
1770.3174	0.81	0.54	−99.2	−9.1	92.0	1.88	1.74	1.50
1770.3319	0.89	0.65	−100.1	−18.7	85.2	1.87	1.62	1.38
1771.2465	0.64	0.44	−124.0	−15.9	66.4	2.66	1.37	1.45
1771.2625	0.77	0.77	−124.0	−20.8	77.3	2.74	1.48	1.00
2066.3388	0.81	0.83	−104.0	−10.0	57.4	2.21	1.38	0.98
2067.2923	0.83	0.81	−102.0	−11.5	55.2	2.10	1.32	1.02
2067.3131	1.10	0.98	−103.0	−13.1	56.1	1.85	1.23	1.12
2067.3284	1.30	1.20	−101.5	−12.6	50.4	1.76	1.27	1.08
2083.3000	1.30	1.10	−103.0	3.9	52.0	1.74	1.77	1.18
2083.3104	1.20	1.32	−102.6	4.4	51.2	1.88	1.79	0.91
2084.2979	1.11	1.07	−84.3	5.6	35.0	1.69	1.89	1.04
2084.3097	1.21	1.10	−79.6	−7.4	35.2	1.37	1.81	1.10
2113.4708	1.29	1.27	−77.3	−1.4	50.0	1.80	1.91	1.02
2157.2687	1.14	0.98	−72.6	17.1	38.1	1.65	1.88	1.16
2157.2798	1.33	1.22	−70.7	20.7	37.9	1.88	1.78	1.09

Fig. 3b shows the corresponding spectral window. The most significant peak in this range is at $\nu = 0.00085$ d^{-1}, corresponding to a period of 1180 ± 60 d. This period can satisfactorily reproduce all the V_r measurements. The radial-velocity curve is shown in Fig. 4. The phases were computed using the elements $\mathrm{Min}V_r(\mathrm{HeI}) = \mathrm{JD}\ 2452157 + 1180E$. The solution of the radial-velocity curve using the method of Lehmann-Filhés [27] yields the spectroscopic orbital elements in Table 4.

All available $UBVR$ photometry of HD 200775 is contained in the data bank [28], available via the Internet. The bulk of the photometric data were obtained by the group of Shevchenko (for example, see [13]). The data bank presents a total of 1148 individual $UBVR$ observations acquired over 15 years. Some seasons display rapid brightness fluctuations,

Table 3. Parameters of the HeI lines in the spectrum of HD 200775

JD2450000+	HeI λ5875			HeI λ6678			HeI λ4471			HeI λ4387		
	V_r, km/s	W, Å	$\Delta\lambda_{1/2}$, Å	V_r, km/s	W, Å	$\Delta\lambda_{1/2}$, Å	V_r, km/s	W, Å	$\Delta\lambda_{1/2}$, Å	V_r, km/s	W, Å	$\Delta\lambda_{1/2}$, Å
1020.4792	–	–	–	1.2	0.88	3.35	−15.6	1.27	2.55	−9.3	1.20	2.00
1020.4875	–	–	–	1.7	0.86	3.40	−14.0	1.22	2.23	−8.3	1.37	2.60
1024.4896	–	–	–	−1.2	0.55	1.73	−4.0	1.12	2.16	−16.1	1.31	2.80
1024.4972	–	–	–	3.8	0.58	1.80	−6.0	1.18	2.08	−17.0	1.12	2.30
1036.3431	–	–	–	−3.3	0.59	2.17	−13.0	1.13	1.99	−12.4	1.19	2.16
1036.3653	–	–	–	−3.2	0.48	2.10	−12.5	1.18	1.51	−10.8	1.17	2.56
1036.3819	–	–	–	−2.4	0.49	1.90	−11.9	0.80	1.79	−11.3	0.75	2.90
1036.3958	–	–	–	1.1	0.71	2.44	−11.1	1.00	1.86	−19.4	1.08	2.20
1054.4618	–	–	–	−2.8	0.65	2.31	−2.8	1.11	1.49	−2.6	1.10	2.35
1054.4694	–	–	–	−3.0	0.50	1.96	−3.4	1.09	1.61	−4.3	1.75	2.01
1769.3556	8.0	0.66	1.95	8.9	0.37	2.07	12.4	0.98	1.76	13.3	1.53	2.29
1769.3729	11.0	0.56	2.37	7.9	0.36	1.65	9.4	1.30	1.88	17.0	1.42	2.21
1770.2604	15.0	0.58	1.65	4.1	0.41	1.55	14.2	1.34	2.10	12.5	1.29	1.99
1770.2882	17.7	0.62	1.59	4.4	0.41	1.68	18.2	1.37	2.30	13.4	1.25	1.97
1770.3319	14.5	0.59	1.88	3.7	0.36	2.15	9.3	1.22	2.12	12.7	1.19	2.25
1770.3517	8.5	0.66	1.89	3.8	0.37	1.74	10.7	0.71	2.35	16.1	1.25	2.28
1771.2465	6.8	0.73	2.63	13.6	0.41	2.13	13.4	1.41	3.02	14.0	0.73	2.30
1771.2625	10.0	0.52	1.68	9.9	0.50	2.03	9.0	1.18	2.26	13.6	1.29	2.53
2066.3388	1.2	0.61	2.70	2.4	0.48	2.04	1.8	1.02	1.56	3.1	1.22	2.44
2067.2923	−0.5	0.60	2.56	1.3	0.52	2.09	1.4	0.94	2.00	2.9	1.09	2.12
2067.3131	0.9	0.72	2.44	1.9	0.59	1.99	1.8	0.73	1.23	3.1	1.19	2.19
2067.3284	0.7	0.73	2.95	1.1	0.68	2.56	–	–	–	–	–	–
2083.3000	−2.1	0.89	2.67	0.8	0.67	2.89	−1.4	0.66	1.08	1.3	1.26	2.37
2083.3104	−3.2	0.94	2.88	−1.2	0.61	2.91	−0.6	0.61	1.42	1.1	1.06	2.19
2084.2979	−14.2	1.60	3.84	−8.7	0.41	1.97	−14.0	0.26	1.48	–	–	–
2084.3097	−15.7	0.68	2.10	−9.7	0.65	4.62	–	–	–	–	–	–
2113.4569	−12.5	0.67	1.70	−11.1	0.67	2.80	−10.9	0.69	3.22	−6.7	0.96	2.20
2113.4708	−5.9	0.65	1.50	−12.3	0.75	2.50	−11.5	0.75	3.38	−18.0	0.95	2.10
2157.2687	−7.4	0.87	2.75	−5.5	0.54	2.52	−16.0	0.60	2.73	–	–	–
2157.2798	−11.6	0.94	3.03	−10.6	0.67	2.74	−12.0	1.51	2.59	−7.3	0.73	2.30

with amplitudes up to $\Delta V = 0^m.1$, superposed by a wave of long-term variability with an amplitude $\Delta V \leq 0^m.05$.

The environment of HD 200775 was studied in the 21 cm band with 14″ resolution in [29]. There is an HI region near the star with a biconical cometary shape formed by strong matter outflows occurring in the course of the system's evolution. These data testify to the complex circumstellar structure of the HD 200775 system. This structure can explain the observed rapid variations of the star's brightness and spectrum during individual seasons. The system's

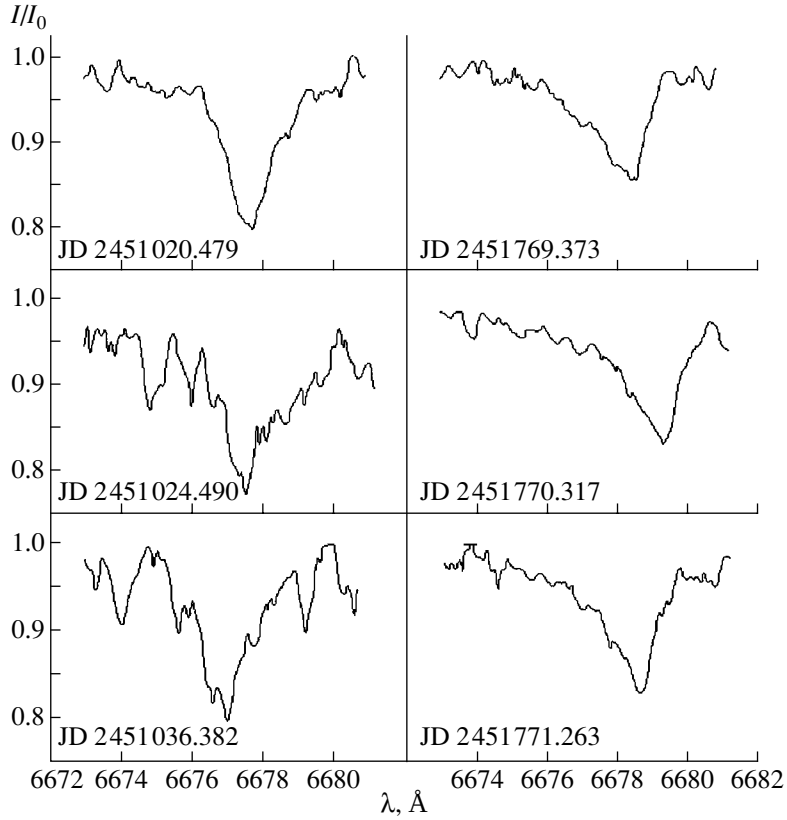

Fig. 2. The HeI λ6678 Å line profiles in 1998 (left) and 2000 (right).

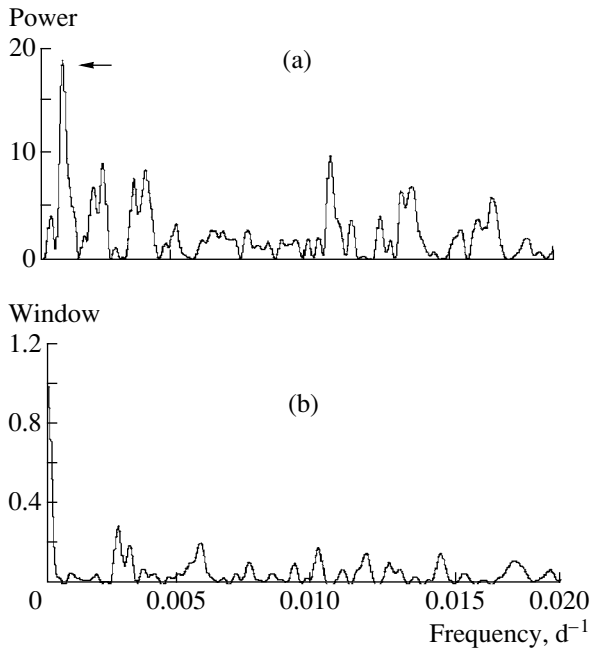

Fig. 3. The power spectrum (a) and the window spectrum (b) for the radial velocities of the HeI λ5876 Å line. The arrow in the upper panel marks the most significant peak.

bright component, with a radius of $\sim R_\odot$, should have a rotational period of about 20 hours. Therefore, it is reasonable to expect that the rapid brightness variations should have a time scale of the order of several hours.

Figure 5 shows the mean V light curve folded in accordance with the phases of the spectroscopic orbital period. The observations were averaged using phase bins with a width of 0.05. Strongly deviating observations were rejected. The presence of strongly deviating observations for this star was also noted in [13]. The figure demonstrates that the plotted mean data have large uncertainties and that the light curve as a whole cannot be considered entirely regular. The light curve shows a comparatively narrow phase interval (about 0.2 of the period, or 228 days) near the minimum of the radial-velocity curve (when the star approaches the observer at the highest rate, i.e., in the descending node), characterized by a higher brightness.

The nature of the detected photometric variability with the orbital period is not entirely clear. The light curve is not typical of eclipsing, ellipsoidal, or reflection variability. Based on the half-widths of the HeI lines (on average, about 2 Å), the star's rotational velocity projected onto the line of sight can

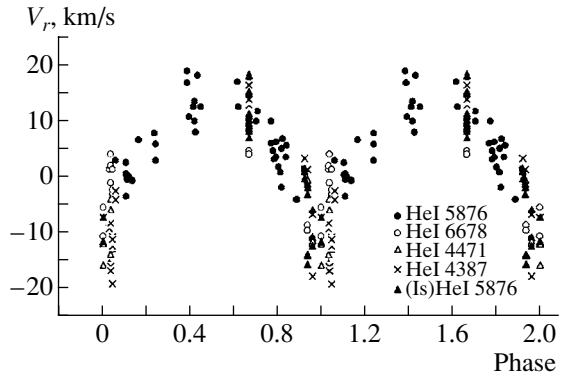

Fig. 4. Radial-velocity curve of HD 200775 derived from the HeI lines, folded with the 1180-day period. The radial velocities of all the lines except HeI λ5876 Å were measured by the author. The radial velocities determined by the author for the HeI λ5876 Å lines are designated (Is)HeI 5876 Å.

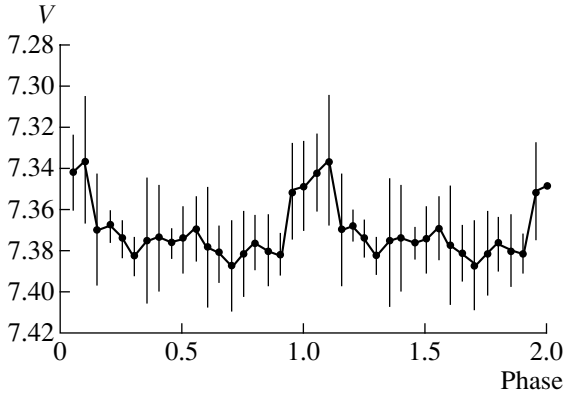

Fig. 5. Mean V light curve of HD 200775 for the phases of the spectroscopic period. The dispersion when averaging over phase is shown for each data point.

be estimated to be $v \sin i \approx 110$ km/s, leading to the estimate $i \sim 25°$, assuming that the real rotational velocity is comparable to those characteristic of early Be stars (250–300 km/s). If we nevertheless suppose that the variability is due to eclipse-like phenomena, then the eclipses must be due to gas and dust forming a semitransparent extended envelope of considerable size.

3. CONCLUSIONS

Our observations show that HD 200775 is probably a spectroscopic binary system with a period of about 3.22 years. We determined the system's corresponding spectroscopic orbital elements. The mass function, $f_1 = 0.446 \pm 0.010 M_\odot$, should be considered a lower limit for the secondary's mass. The system is located in a star-forming region [2–4, 6], and the companion may be a young star with a mass $\leq 1 M_\odot$. Binaries whose bright components are (O–B) stars with young T Tauri star companions are known (see, for instance, [30–33] and references therein).

Table 4. Spectroscopic orbital elements of the spectroscopic binary system HD 200775

Orbital element	Value
Period P, days	1180 ± 60
Eccentricity e	0.103 ± 0.01
Semiamplitude K_1, km/s	15.5 ± 0.5
Center-of-mass velocity γ, km/s	5.0 ± 0.3
Orbital semimajor axis $a \sin i$, $R_\odot$	357 ± 5
Mass function $f_1(m)$, $M_\odot$	0.446 ± 0.010
Longitude of periastron ω, deg	251 ± 5

An analysis of the light curve together with the radial-velocity curve reveals some synchronism between the photometric variability and the radial-velocity variations. If we interpret the mean V light curve as resulting from eclipses, the eclipsing body must have a very large linear size, comparable to that of the spectroscopic orbit. The spectrum of the star does not experience any significant changes at phases of reduced brightness. The star may be partially eclipsed by semitransparent circumstellar gas and dust. New observations are needed before we can achieve a full understanding of all the features of this system.

To conclude, we list the principal results of this study.

(1) We have plotted the first complete radial-velocity curve based on data for helium lines and computed the spectroscopic orbital elements for the Herbig Ae/Be star HD 200775. The system is a spectroscopic binary with an orbital period of $P = 1180 \pm 60$ days (3.22 years).

(2) The parameters of the H_α and H_β lines display long-time-scale as well as rapid changes. The long-time-scale variations are mainly due to the spectroscopic binarity, whereas the rapid changes are apparently related to the axial rotation of the primary and the presence of a nonuniform circumstellar envelope.

(3) Using data from the literature, we have plotted the system's V light curve folded with the spectroscopic period. We have attempted to interpret the orbital-period photometric variability as being due to partial eclipses by a semitransparent circumstellar envelope.

ACKNOWLEDGMENTS

The author is grateful to N.N. Samus' and A. S. Rastorguev for their help during the preparation of the final version of the manuscript.

REFERENCES

1. G. H. Herbig, Astrophys. J., Suppl. Ser. **4**, 337 (1960).
2. E. E. Mendoza, Astrophys. J. **128**, 207 (1958).
3. L. Rosino and G. Romano, Contr. Oss. Astrof. Padova Asiago, No. 127, 1 (1962).
4. D. Y. Gezari, M. Schmitz, and J. M. Mead, *Far IR Supplement: Catalog of IR Observations, 1984,* NASA Ref. Publ., No. 1119, p. A-69.
5. G. D. Watt, W. B. Burton, S.-U. Choe, and H. S. Liszt, Astron. Astrophys. **163**, 194 (1986).
6. J. R. D. Lepine and Nguen-Quang-Rieu, Astron. Astrophys. **36**, 469 (1974).
7. R. Viotti, Mem. Soc. Astron. Ital. **40**, 75 (1969).
8. A. Altamore, G. B. Baratta, A. Casatella, *et al.*, Astron. Astrophys. **90**, 290 (1980).
9. U. Finkenzeller, in *IAU Colloq. 98: Physics of Be Stars,* Ed. by M. Jaschek and H. G. Groth (D. Reidel, Dordrecht, 1982), p. 501.
10. B. Baschek, M. Beltrametti, J. Köppen, and G. Traving, Astron. Astrophys. **105**, 300 (1982).
11. S. E. Strom, K. M. Strom, J. Yost, *et al.*, Astrophys. J. **173**, 353 (1972).
12. M. A. Pogodin, Astron. Zh. **62**, 918 (1985) [Sov. Astron. **29**, 531 (1985)].
13. V. S. Shevchenko, M. A. Ibragimov, and S. D. Yakubov, Astron. Zh. **66**, 941 (1989) [Sov. Astron. **33**, 487 (1989)].
14. M. A. Ruusalepp, Publ. Tartu Astrophys. Obs. **52**, 303 (1987).
15. N. Sh. Minikulov, M. A. Pogodin, and A. E. Tarasov, Pis'ma Astron. Zh. **13**, 132 (1987) [Sov. Astron. Lett. **13**, 54 (1987)].
16. A. S. Miroshnichenko, C. L. Mulliss, K. S. Bjorkman, *et al.*, Publ. Astron. Soc. Pac. **110**, 883 (1998).
17. N. Z. Ismailov, Izv. Akad. Nauk Azerb., Ser. Fiz.-Tekh. Mat. Nauk **21**, 87 (2001).
18. N. Z. Ismailov, Tsirk. Shemakhinsk. Obs., No. 101 (2001).
19. T. E. Espin, Astron. Nachr. **145**, 321 (1898).
20. G. A. Galazutdinov, Preprint SAO No. 92 (1992).
21. S. G. Aliev and N. Z. Ismailov, Astron. Zh. **77**, 834 (2000) [Astron. Rep. **44**, 738 (2000)].
22. N. G. Beskrovnaya, M. A. Pogodin, A. G. Shcherbakov, and A. E. Tarasov, Astron. Astrophys. **287**, 564 (1994).
23. M. A. Pogodin, A. S. Miroshnichenko, K. S. Bjorkman, *et al.*, Astron. Astrophys. **359**, 299 (2000).
24. J. D. Scargle, Astrophys. J. **263**, 835 (1982).
25. J. H. Horne and S. L. Baliunas, Astrophys. J. **302**, 757 (1986).
26. I. Antokhin, J.-F. Bertrand, R. Lamontagne, *et al.*, Astron. J. **109**, 817 (1995).
27. R. Lehmann-Filhés, Astron. Nachr. **136**, 17 (1894).
28. W. Herbst, D. K. Herbst, E. J. Grossman, and D. Weinstein, Astron. J. **108**, 1906 (1994).
29. A. Fuente, J. Martin-Pintado, A. Rodriguez-Franco, and G. D. Moriarty-Schieven, Astron. Astrophys. **339**, 575 (1998).
30. K. P. Lindroos, Astron. Astrophys. **156**, 223 (1986).
31. N. Z. Ismailov, Astron. Zh. **65**, 971 (1988) [Sov. Astron. **32**, 508 (1988)].
32. E. A. Antokhina, N. Z. Ismailov, and A. M. Cherepashchuk, Pis'ma Astron. Zh. **15**, 837 (1989) [Sov. Astron. Lett. **15**, 362 (1989)].
33. E. A. Vitrichenko and S. I. Plachinda, Pis'ma Astron. Zh. **27**, 682 (2001) [Astron. Lett. **27**, 581 (2001)].

Translated by N. Samus'

Astronomy Reports, Vol. 47, No. 3, 2003, pp. 214–231. Translated from Astronomicheskiĭ Zhurnal, Vol. 80, No. 3, 2003, pp. 239–257.

Interpretation of Light Curves of the Cataclysmic Variable OY Car in a Model with Shockless Interaction between a Gaseous Stream and the Disk

T. S. Khruzina[1], A. M. Cherepashchuk[1], D. V. Bisikalo[2], A. A. Boyarchuk[2], and O. A. Kuznetsov[3]

[1] *Sternberg Astronomical Institute, Universitetskiĭ pr. 13, Moscow, 119899 Russia*

[2] *Institute of Astronomy, Russian Academy of Sciences, ul. Pyatnitskaya 48, Moscow, 109017 Russia*

[3] *Keldysh Institute of Applied Mathematics, Russian Academy of Sciences, Miusskaya pl. 4, Moscow, 125047 Russia*

Received June 22, 2002; in final form, August 21, 2002

Abstract—To determine the parameters of the accretion disk and shock-wave region responsible for the formation of the orbital peak in the light curve of the binary system OY Car (an SU UMa-type variable), we have analyzed its $UBVR$ and JK light curves using two gas-dynamical models with different regions of shock interaction: one with a hot line along the stream from the Lagrange point L_1 and one with a hot spot on the accretion disk. The hot-line model can better describe the quiescent state of the system: the maximum χ^2 for the optical light curves does not exceed 207, whereas the minimum residual for the hot-spot model is $\chi^2 > 290$. The shape of the eclipse is almost identical in both models; the main differences are in interpreting out-of-eclipse portions of the light curves, whose shape can vary in the transition from one orbital cycle to another. The hot-spot model is not able to describe variations of the system's brightness at orbital phases $\varphi \sim 0.1$–0.6. The rather complex behavior of the observed flux in this phase interval can be explained in the hot-line model as being due to variations of the temperature and size of the system. Based on the analysis of a sequence of 20 B curves of OY Car, we conclude that the flux variations in the primary minimum are due to variations of the luminosity of the accretion disk, whereas the flux variability in the vicinity of the orbital peak is due to the combined effect of the radiation of the disk and hot line. The JK light curves of OY Car in the quiescent state and during a small flare also indicate preference for the hot-line model, since the primary minimum and the flux near quadratures calculated using the hot-spot model are not consistent with the observations. © *2003 MAIK "Nauka/Interperiodica".*

1. INTRODUCTION

Cataclysmic close binary systems are among the most interesting non-steady-state astrophysical objects, due to the intense mass transfer between the components. Their short orbital periods enable the determination of the characteristics and parameters of the system over comparatively short observational times.

The light curves and radial-velocity curves of these systems indicate that they consist of a white dwarf and cool main-sequence star. The latter fills its Roche lobe, resulting in an outflow of matter through the vicinity of the inner Lagrange point L_1. Further, this matter is captured by the white dwarf's gravitation and forms an accretion disk, halo, and intercomponent envelope. The existence of the accretion disk is confirmed by the profile of the eclipse of the white dwarf and the surrounding material by the cool component of the system. However, light curves of eclipsing close binaries display some additional features that cannot be described in simple "cool star–white dwarf–accretion disk" models. In particular, the vast majority of light curves of eclipsing close binaries display a so-called "orbital peak." Gorbatskiĭ [1] and Smak [2] suggested that this is due to a hot spot at the edge of the accretion disk, where the stream from L_1 collides with the disk. Over the last 30 years, the hot-spot model has been widely used to interpret the light curves of cataclysmic binaries (see, for example, [3]).

Gas-dynamical studies of the mass transfer in close binaries [4–9] showed that the stream and accretion disk are morphologically a single formation and that their interaction is shockless. Naturally, in this case, the temperature at the point of contact between the stream and disk does not increase, so that the hypothesis that there is a hot spot on the accretion disk must be abandoned. Three-dimensional gas-dynamical calculations of mass transfer in an interacting close binary [4–9] have indicated that, in the steady-state case, a shock interaction resulting

1063-7729/03/4703-0214$24.00

Table 1. Parameters of the OY Car components

The system, $P = 0^d.063121$ [17]			Hot dwarf			Cool star		
i, deg	$q = M_1/M_2$	a_0, 10^{10}, cm	R_1/a_0	T_1, K	M_1, $M_\odot$	R_2/a_0	T_2, K	M_2, $M_\odot$
79(2) [14]	4–7 [14]	4.8(3) [14]	0.013(4) [14]	25 000 [16]	0.95 [14]	0.23(6) [14]	3000 [14]	0.14 [14]
81 [28]	9.8(3) [29]	4.3(2) [29]	0.0182(3) [29]	$\geq$ 20 000 [31]	0.33 [22]	0.209 [29]		0.07 [29]
83.3 [29]				$\leq$15 000 [28]	1.26 [18]			
				15 000 [23]	0.68 [29]			
					0.69 [17]			
82	9.8		0.0182	15 000			3000	

Note: The bottom row presents parameters derived from our analysis of the OY Car light curves. The error in the last digit of a parameter is given in parentheses.

in a temperature increase occurs when the matter flowing around the accretor but not yet captured by the disk collides with the stream from L_1. This interaction forms an extended shock wave oriented along the stream [4–6, 10] (the "hot line"), whose radiation makes it possible to understand certain observed effects in the light curves of cataclysmic variables [11, 12], in particular, the occurrence of regular and irregular peaks during eclipses of the accretion disk by the donor star. Comparisons between models with a hot spot and a hot line [11, 12] have presented conclusive evidence in favor of the latter type of model for the interpretation of close-binary light curves.

Eclipsing close binaries, whose light curves can be used to investigate the flow structure, are rare and do not form a homogeneous group. Therefore, it is of interest to consider close binaries with various features in their light curves and to analyze the suitability of various gas-dynamical models for their interpretation. Here, we present our analysis of light curves of the SU UMa cataclysmic variable OY Car.

2. GENERAL INFORMATION ABOUT OY Car

The variability of OY Car (= *S*6302) was discovered by Hoffmeister [13] in 1959; however, this star was observed little in the subsequent two decades. In the beginning of the 1980s, interest in this system increased substantially, leading to intense observations. Comprehensive summaries of the photometric observations are given by Vogt *et al.* [14], Vogt [15], Schoembs *et al.* [16, 17], and Cook [18], of IR photometric observations by Berriman [19, 20] and Sherrington *et al.* [21], and of spectral observations by Bailey and Ward [22], Hessman *et al.* [23], and Harlaftis and Marsh [24].

The light curve of the system in the inactive state is typical of eclipsing close binaries. A pronounced peak with its maximum at phase $\sim$0.75 is observed in each orbital cycle prior to the eclipse of the primary. The times of the onset and end of the ingress into eclipse for the white dwarf, disk, and hot region of the shock are clearly visible in the eclipse curve.

In the active state, the system displays a number of peculiarities. The flare activity of OY Car classifies it as an SU UMa variable; these are dwarf novae with orbital periods shorter than 3 h. Flares of this type of star are divided into two separate classes: regular flares, which are brief and irregularly distributed in time, and superflares. The latter are more prolonged, brighter, and less frequent; however, at the same time, they are more predictable. In the case of OY Car, the regular flares occur every 25–50 days and have amplitudes up to $\simeq 3^m$ and durations of about 3 days. Superflares occur approximately once a year. Their amplitude reaches 4^m, and they may last for up to 2 weeks. Photometric observations of the system in these periods have been carried out by Krzeminski and Vogt [25], Schoembs [26], and Bruch *et al.* [27].

Observations of OY Car are analyzed in [18, 22, 23, 28, 29]. The orbital parameters and mass ratio of the components were derived from radial-velocity measurements. The size of the disk and the white dwarf, as well as the orbital inclination, were estimated based on the shape of the primary minimum. The spectrum and comparisons of the photometric parameters of the system in various colors have been used to determine the effective temperature of the cool component and, with lower accuracy, the temperature of the hot star. The mass of the white dwarf was estimated based on its radius using the Hamada–Salpeter relation [30]; later, the mass of the cool component was also derived. The period of the system was determined with good accuracy from an extensive set of photometric observations. Table 1 presents some parameters of OY Car.

Below, we analyze $UBVR$ [17, 27, 29] and JK [21] light curves of OY Car and derive the characteristics of the main gaseous components of the system: the accretion disk and the shock region responsible for the formation of the orbital peak.

3. BASIC ASSUMPTIONS OF THE MODEL

The observed radiation of a binary system is generally a combination of the contributions of both of its components, the accretion disk, and gaseous structures forming in the system due to the outflow from the donor star. According to gas-dynamical calculations, the shape of the intercomponent gaseous envelope in the system is rather complex, and a detailed analysis of its radiation represents a very sopisticated problem. As a first approximation, given the low gas density in the intercomponent envelope, we will ignore its contribution to the total radiation. We also assume that the contribution to the visible radiation from the stream from L_1 is negligible due to the low temperature of the gas in the stream. In our present model, we take into account only the radiation from the system's components, the accretion disk, and the shock-interaction region.

In general, light-curve analyses can be used to determine the parameters of these systems. However, since each source has some temperature and size, and since the temperature can vary across the surface of the star, even a restricted model will be specified by a set of more than 20 parameters. Naturally, the large number of parameters involved complicates their reliable determination. Therefore, we selected a set of parameters whose values are known with high certainty and fixed them in the model. For example, we adopted the values in Table 1 for the stellar components.

Imposing additional constraints enabled us to restrict the number of free parameters and thereby simplify the model. Here, we aim to obtain the characteristics only of the accretion disk and the region of shock interaction by analyzing the light curves. We derive solutions using two gas-dynamical models with different locations for the region of shock interaction: (a) in a hot line along the stream from L_1 (this model is described in [32]) and (b) in a hot spot on the accretion disk (the light curve for this model is synthesized in [33]). Comparisons between the results will help distinguish between these gas-dynamical models.

4. OPTICAL LIGHT CURVES OF OY Car IN ITS INACTIVE STATE

Schoembs *et al.* [17] carried out photometry of OY Car in its inactive state using a multichannel photometer with a time resolution 2 s. They present continuous sets of B observations during six nights from January 26 to February 2, 1984 (HJD 2445725–2445733). The shape of the light curves varies substantially. Those with flat portions between the orbital peaks alternate with those displaying flares between the peaks. No periodicity in the occurrence of the flares has been detected.

Twenty light curves at orbital phases from −0.5 to +1.5 were selected from the six sets of observations obtained on different nights, labeled with numbers N from 1 to 20. When constructing the Nth curve, observations for partial orbital light curves (i.e., those observed at the beginning and end of the observations) were assigned to the nearest total light curve. When an observational set was divided into separate orbital curves, the interval of orbital phases was selected so that the fluxes at the beginning and end of the light curve were roughly the same. As a rule, this break fell at phases $\varphi \sim 0.3$–0.4, However, if a secondary peak (flare) was observed in this phase interval at the beginning or end of the curve, the break was shifted to a less perturbed portion of the curve.

The out-of-eclipse portions of individual observed light curves were averaged. The averaged portions of the curves are represented by $n = 23$–33 regular dots with the rms error $\sigma_j \sim 0^m.010$–$0^m.015$. Observations at the minimum of the light curve were not averaged. Generally, four to eight points were obtained during an eclipse of the white dwarf. Unaveraged observations were assigned the error $\sigma \simeq 0^m.03$, which roughly corresponds to the error of a single observation [17]. From the collection of 20 observed light curves, we selected the $N = 14$ curve, which had the minimum flux ($\delta B = 3^m.83$ relative to the comparison star) at the first quadrature ($\varphi = 0.25$), and used this magnitude $\delta B = 3^m.83$ as the zero level for all remaining light curves. All 20 individual light curves were expressed in magnitude differences ΔB relative to the magnitude of the system at the first quadrature of the $N = 14$ light curve:

$$\Delta B = B_N^{obs}(\varphi) - B_{14}^{obs}(\varphi)$$
$$= -2.5\log(F_N^{obs}(\varphi)/F_{14}^{obs}(0.25)).$$

This means that we use the same energy unit—the observed flux from the system at orbital phase $\varphi = 0.25$ for the $N = 14$ light curve—for the entire set of 20 light curves. This enables us to estimate the brightness differences between curves at each phase, and thereby to use variations of the flux levels, as well as of the shape of the light curve, when comparing the observed and synthesized curves. In other words, this is one way to impose additional restrictions on the range of allowed parameters of the system.

The shapes of successive light curves of OY Car in its inactive state indicate that some non-steady-state processes occur in the system even during this

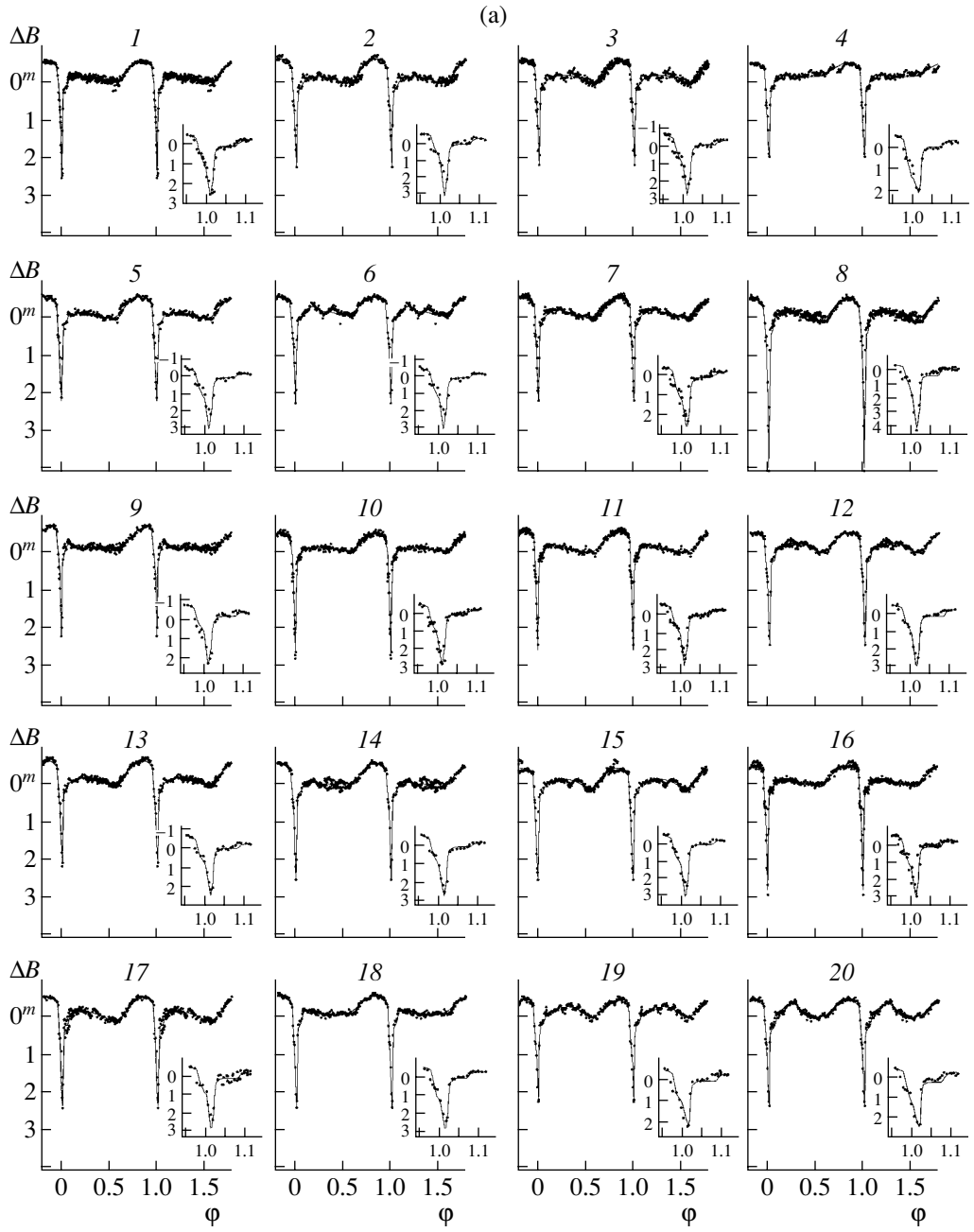

Fig. 1. (a) Individual B light curves of OY Car in magnitude differences relative to the flux observed at quadrature ($\varphi = 0.25$) for the $N = 14$ light curve. The solid curves indicate theoretical light curves synthesized in the hot-line model. The inset in each plot presents the eclipse portion of the corresponding light curve. (b) Contributions of the white dwarf (*1*), donor star (*2*), elliptical disk (*3*), and hot line (*4*) to the total flux in arbitrary units (see text) for the corresponding light curve of OY Car.

brief period of time (Fig. 1a). There are variations in both the depth of the primary minimum (with amplitudes up to $\simeq 1^m$–2^m) and in the amplitude of the orbital peak (up to $\simeq 0^m.5$) associated with the region of shock radiation. The shape of the curve varies at orbital phases $\varphi \sim 0.2$–0.6 from cycle to cycle, precisely in the phase interval when the radiation from the hot spot cannot reach the observer.

We analyzed 20 individual light curves using the hot-line model in order to identify the model components whose variations result in the observed variations of the shape of the orbital curves. In addition, it was important to confirm that the hot-line model provides a better fit than the hot-spot model, not only in the analysis of the light curve averaged over numerous cycles, but also for each of the 20 individual light curves, despite the substantial cycle-to-cycle variations.

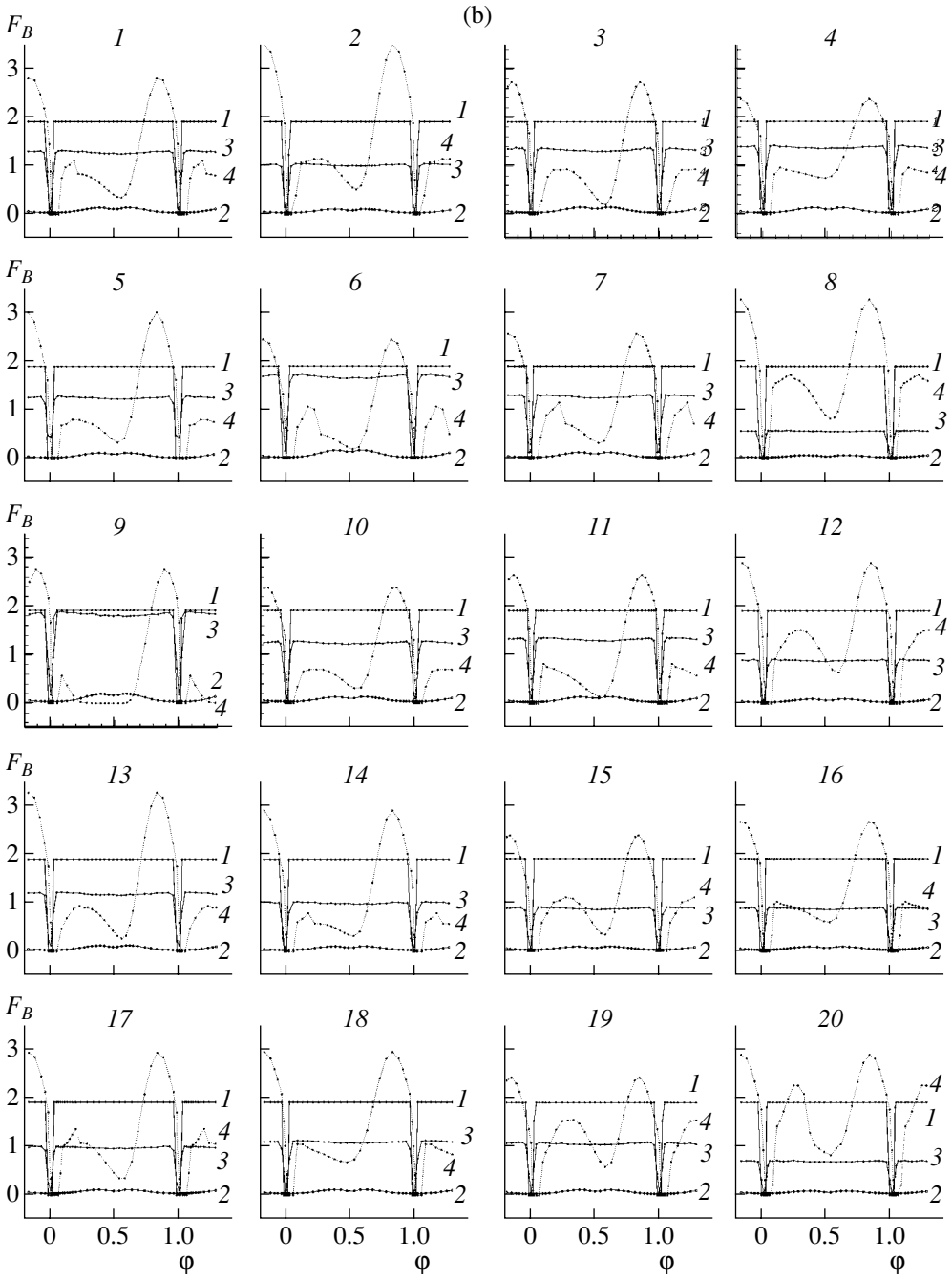

Fig. 1. (Contd.)

To construct the theoretical light curve, we calculated the flux from the system's components $F(X, \varphi)$ for a specified set of parameters X and for a sequence of orbital phases φ. The resulting $F(X, \varphi)$ values were given in arbitrary units. They can be transformed into generally accepted units (per unit wavelength interval) using the expression $f = Fa_0^2 \times 10^{-12}$ erg/s cm^3, where a_0 is the distance between the centers of mass of the stars in centimeters. As noted above, the N analyzed light curves ($N = 1$–20) are given in magnitude differences ΔB, where $\Delta B = 0\overset{m}{.}0$ corresponds to the average observed flux at the first quadrature for the $N = 14$ light curve. Accordingly, when translating the theoretical fluxes $F_N^{th}(X, \varphi)$ to magnitudes $\Delta B_N^{th}(X, \varphi)$ when constructing the synthesized light curves, we used the first-quadrature flux $F_{14}^{th}(0.25)$ for the theoretical curve that gives the best fit to the observed $N = 14$ light curve; i.e., the theoretical magnitude of the

system at phase φ for light curve N will be

$$\Delta B_N^{th}(\varphi) = -2.5\log(F_N^{th}(\varphi)/F_{14}^{th}(0.25)).$$

This imposes an additional restriction on the range of allowed parameters. If we interpret a single light curve rather than a sequence of homogeneous curves, the first-quadrature flux corresponding to the given trial curve is used to translate the calculated flux to magnitudes to construct the trial theoretical curve (in magnitudes). In this case, there is no need to first subtract the first-quadrature flux in magnitudes from the observed light curve. To compare the synthesized and observed curves, it is sufficient to shift the calculated trial light curve so that the observed and calculated fluxes (in magnitudes) at the first quadrature coincide. We selected the best-fit theoretical light curve based on a minimum residual χ^2 derived from comparison with the observed curve.

We carried out the calculations for the sequence of 20 B light curves in two stages. We first fixed five of the 18 unknown parameters, which had been determined with sufficient certainty in other studies. The values adopted for these parameters are presented in the bottom row of Table 1. We thus reduced the number of unknown parameters to 13 at the first stage of our calculations. The allowed values of most of these were additionally restricted.

For example, in accordance with [15–17], the maximum radius of the disk was restricted to the interval $a_{\max}/\xi = 0.53$–0.62, since analyses of the shapes of eclipses yield the average radius $a_d/\xi = 0.58$ for $q = 9.8$ (ξ is the distance between the center of mass of the white dwarf and the inner Lagrange point, $\xi/a_0 = 0.7159$). As a rule, when the structure of eclipses is analyzed, only the time of the beginning of the disk eclipse is determined with certainty, whereas the time of the egress from the eclipse is determined fairly uncertainly [34]. On the other hand, three-dimensional hydrodynamical calculations of flows in cataclysmic variables [35] indicate that, in the inactive state of the system, the accretion disk is elliptical and the longitude of its periastron lies in the interval $\alpha_e \sim 150°$–$170°$. Given this orientation of the disk, the radius derived from the moment of the ingress of the eclipse is close to the radius at apoastron of the disk. Therefore, it was the radius of the disk at apoastron rather than its average value that we restricted in our calculations.

The other desired parameters describe the shape of the disk and the shape and size of the hot line:

(1) the eccentricity of the disk (we assumed its value in the inactive state does not exceed $e \sim 0.22$);

(2) the paraboloid constant A_p specifying the thickness of the outer edge of the disk z/a, along with the radius of the disk at periastron (for a thin disk, $A_p \sim 5$–7);

(3) the azimuth of the disk periastron α_e, measured in the direction of the orbital motion of the secondary, from the straight line connecting the centers of mass of the components;

(4) the brightness temperature T_b in the boundary layer where the disk material is accreted onto the compact star ($T_b \geq T_1$);

(5) the parameter α_g specifying the variation of the brightness temperature with the disk radius in accordance with the formula $T_r = T_b(R_1/r)^{\alpha_g}$ (we assumed $\alpha_g \sim 0.6$–0.75);

(6) the shape of the hot line—a truncated ellipsoid with semiaxes a_v, b_v, c_v extended toward the inner Lagrange point L_1 (the lateral surface of this ellipsoid coincides with the tangent to the elliptical disk for any disk orientation, while its center is located in the orbital plane inside the disk at some distance from its edge; the procedure used to construct the shape of the hot line is described in detail in [32]);

(7) the maximum brightness temperature of the hot line on its windward ($T_{\max}^{(1)}$) and leeward ($T_{\max}^{(2)}$) sides;

(8) the y coordinate on the axis of the hot line $y_{\min}$, where the heating of the gaseous stream by the shock wave becomes zero (i.e., the temperature is equal to the temperature the matter would have in the absence of the shock);

(9) the shift Δy along the axis of the hot line between the points with the maximum values $T_{\max}^{(1)}$ and $T_{\max}^{(2)}$ from the windward and leeward sides (generally, $\Delta y/a_0 < 0.05$).

The calculations indicate that the values for the eccentricity of the disk, A_p, and α_g derived from the analysis of the 20 light curves are fairly closely clustered around their average values. At the second stage of the calculations, we also fixed the values of these parameters to be $e = 0.185$, $A_p = 5.400$ (which corresponds to an flaring angle for the outer edge of the disk $\beta_d = 3.^\circ 9$), and $\alpha_g = 0.70$. A trial run was made for Δy in the interval 0.0–0.60. As a result, the number of free parameters was decreased to nine.

Table 2 presents the resulting parameters of the disk and hot line, as well as the values of other quantities that depend on them. Asterisks denote light curves whose shapes are distorted by short flares at orbital phases $\varphi \sim 0.5$. Table 2 also presents the observed flux of OY Car relative to the comparison star averaged for phase intervals $\varphi = 0.99$–1.01, 0.10–0.16, 0.50–0.60, and 0.80–0.86.

Since only one of the solutions (for the $N = 14$ curve) had a lower than critical significance level $\chi^2_{0.001,n}$ ($\chi^2_{0.001,n} = 49.7$–64.0 for $\alpha = 0.001$, with the number of degrees of freedom being $n = 23$–33 for

Table 2. Theoretical parameters of OY Car in its inactive state (from B observations), derived from the light curves of [17] and the hot-line model

Parameter	Light curve number									
	1st set of observations			2nd set of observations				3rd set of observations		
	1	2	3*	4	5	6*	7	8	9*	10
n	33	27	30	23	24	25	29	32	29	30
a/a_0	0.364	0.345	0.374	0.345	0.346	0.355	0.363	0.324	0.358	0.356
$a_{\max}/\xi$	0.603	0.571	0.619	0.572	0.572	0.588	0.601	0.536	0.592	0.589
α_e, deg	168.8	159.0	171.7	182.3	161.8	166.0	170.6	148.1	154.9	165.7
T_b, K	22 461	21 069	22 821	22 592	22 134	23 820	22 493	18 270	24 279	22 191
a_v/a_0	0.065	0.057	0.055	0.097	0.062	0.063	0.068	0.075	0.06 7	0.056
b_v/a_0	0.352	0.361	0.334	0.556	0.404	0.384	0.378	0.423	0.20 3	0.352
c_v/a_0	0.021	0.019	0.023	0.018	0.021	0.023	0.022	0.020	0.02 7	0.019
$y_{\min}/a_0$	0.265	0.238	0.248	0.274	0.247	0.302	0.266	0.267	0.203	0.251
$T^{(1)}_{\max}$, K	14 747	18 031	14 782	16 565	15 838	10 592	13 958	19 562	13 691	13 853
$T^{(2)}_{\max}$, K	11 181	13 947	12 246	10 258	13 187	9318	10 612	12 587	12 934	11 611
$\langle T^{(1)}\rangle$, K	6367	6184	6364	3653	5068	5777	5707	5854	8047	5739
$\langle T^{(2)}\rangle$, K	5773	5166	4775	4153	4499	5713	5383	4825	6888	4954
$F^{\rm obs}_{0.99-1.01}$	3.0(2)	3.8(2)	3.9(2)	4.8(2)	4.3(2)	3.8(2)	3.9(2)	0.7(2)	3.8(2)	2.3(2)
$F^{\rm obs}_{0.10-0.16}$	34.6(4)	33.1(5)	33.6(3)	33.7(5)	33.4(7)	37.0(6)	35.1(5)	34. 0(3)	33.6(3)	31.1(3)
$F^{\rm obs}_{0.50-0.60}$	30.2(5)	30.3(4)	29.6(5)	37.0(4)	29.8(3)	32.6(3)	30.0(4)	27. 7(2)	31.5(3)	30.0(3)
$F^{\rm obs}_{0.80-0.86}$	49.4(3)	53.9(7)	49.5(3)	46.9(3)	49.7(5)	50.1(5)	50.1(5)	48. 7(4)	52.9(6)	45.5(5)
$\chi^2_{0.001,n}$	64.0	55.5	59.7	49.7	51.2	52.6	58.3	62.6	58.3	59.7
χ^2	74.8	167	107	179	123	173	173	271	72.2	121
	4th set of observations			5th set of observations			6th set of observations			
	11	12*	13	14	15*	16	17	18	19*	20*
n	30	27	29	27	28	34	30	28	29	31
a/a_0	0.361	0.358	0.367	0.358	0.358	0.356	0.366	0.345	0.360	0.351
$a_{\max}/\xi$	0.598	0.593	0.607	0.593	0.592	0.589	0.605	0.571	0.595	0.581
α_e, deg	160.1	172.6	169.3	167.7	169.2	168.2	170.3	160.3	184.0	175.2
T_b, K	22 599	20 652	22 163	21 210	20 595	20 591	21 186	21 459	21 497	19 500
a_v/a_0	0.078	0.051	0.046	0.056	0.045	0.081	0.063	0.104	0.04 1	0.069
b_v/a_0	0.313	0.415	0.348	0.397	0.368	0.413	0.355	0.464	0.46 7	0.555
c_v/a_0	0.025	0.019	0.020	0.018	0.019	0.019	0.023	0.020	0.01 7	0.018
$y_{\min}/a_0$	0.245	0.264	0.256	0.278	0.231	0.247	0.243	0.274	0.255	0.328
$T^{(1)}_{\max}$, K	15 690	17 485	12 968	12 164	15 990	18 996	18 597	17 334	16 215	15 304
$T^{(2)}_{\max}$, K	12 987	10 878	11 483	10 846	11 990	12 177	12 383	11 582	10 023	9270
$\langle T^{(1)}\rangle$, K	6548	5981	6070	5177	5516	4802	6012	4236	5124	5321
$\langle T^{(2)}\rangle$, K	5096	4982	5897	5565	4332	4625	4871	4713	4701	4873
$F^{\rm obs}_{0.99-1.01}$	3.3(2)	3.0(2)	4.0(2)	2.8(2)	2.8(2)	2.0(2)	3.2(2)	3.2(2)	3.8(2)	3.4(2)
$F^{\rm obs}_{0.10-0.16}$	34.2(3)	33.3(4)	32.2(2)	29.7(4)	30.7(3)	31.6(3)	33.3(4)	34. 0(4)	32.8(3)	32.9(4)
$F^{\rm obs}_{0.50-0.60}$	29.7(4)	29.2(3)	28.9(2)	28.5(4)	26.1(2)	28.9(3)	27.4(3)	32. 2(3)	29.9(4)	30.2(4)
$F^{\rm obs}_{0.80-0.86}$	49.2(3)	46.5(3)	52.9(7)	48.3(3)	44.0(0)	46.2(6)	48.1(3)	49. 9(5)	45.4(6)	45.9(4)
$\chi^2_{0.001,n}$	59.7	55.5	58.3	55.5	56.9	65.5	59.7	56.9	58.3	61.2
χ^2	61.2	106	97.9	46.8	167	258	63.8	172	185	176

Note: n is the number of regular points in the averaged curve. The parameters of the disk and hot line are derived for fixed $q = M_1/M_2 = 9.8$, $i = 82°$, $T_2 = 3000$ K, $T_1 = 15\,000$ K, $R_1 = 0.0182a_0$, $\alpha_g = 0.7$, $e = 0.185$, and $A_p = 5.4$ (this corresponds to a flaring angle for the outer edge of the disk $\beta_d = 3°.9$). The parameter $\Delta y \sim 0.001$–0.02 for most of the light curves. The maximum and minimum radii of the disk for the known e are determined using the formulas $a_{\max} = a(1+e)$ and $a_{\min} = a(1-e)$, where a is the semimajor axis of the disk. The average radius of the red dwarf is $\langle R_2\rangle/a_0 = 0.2144$. The asterisks mark orbital cycles with flares.

various curves; see Table 2), the effect of varying a particular parameter can be estimated by imposing some other limit for the residual in place of the critical limit; for example, the obtained minimum residual can be increased by 10%. For most parameters, the interval of possible variations does not exceed 1–2% of their optimum value. Only for the maximum brightness temperature of the hot line were deviations from the optimum value as large as 8–10% and 2–3% for its windward and leeward sides, respectively; $\Delta y \sim 10$–12%, $a_v \sim 5$–7%, and $\alpha_e \sim 9$–12%.

The solid curves in Fig. 1a represent theoretical light curves synthesized with the parameters from Table 2, reduced to the flux $F_{14}^{th}(0.25)$. The points show the individual (nonaveraged) light curves in magnitude differences relative to the observed first-quadrature flux of the $N = 14$ curve. The curves are numbered in accordance with the notation in Table 2. The inset shows the eclipse portion of the corresponding light curve. The analysis of the contributions from the white and red dwarfs, the elliptical disk, and the hot line indicates (see Fig. 1a) that the contribution of the red dwarf is insignificant at optical wavelengths given the high component mass ratio of OY Car (it does not exceed 1.5–2%).

The out-of-eclipse contribution from the white dwarf is constant for all the curves, at 30–37% of the total maximum flux (at phases $\varphi \sim 0.85$). The out-of-eclipse flux from the elliptical disk is also essentially constant due to the small eccentricity; overall, it is lower than the flux from the white dwarf, and displays a comparable magnitude only in certain individual cycles ($N = 9$, $N = 6$). Since the radius of the disk varies insignificantly, the variations of the disk luminosity are due to fluctuations of T_b. Due to the law for the radial variation of the temperature adopted in our model, the inner parts of the disk that are $\sim 0.25R_d$ from the white dwarf yield roughly the same flux as the remaining outer three quarters, since the temperature of the outer parts of the disk is comparable to that of the red dwarf ($T_d \sim 2000$–3000 K).

The orientation of the disk proved to be close to that obtained from hydrodynamical calculations [35], $\alpha_e \sim 150°$–$185°$; the longitude of the disk periastron fluctuates only slightly about its average value, $\sim 165°$. This orientation of the elliptical disk makes it possible to describe the shapes of both the eclipse and out-of-eclipse portions of the light curves with good accuracy (Fig. 1a). For smaller longitudes of the disk periastron, the theoretical curve remains fairly consistent with the observations. However, the shape of the curve at $\varphi \sim 0.3$–0.8 is fit more poorly. It is not possible to fit the shape of the eclipse well when $\alpha_e > 190°$: its depth decreases and its shape changes, since the eclipse of the hot line shifts toward later orbital phases relative to the eclipses of the white dwarf and disk, which are symmetrical about $\varphi = 0.0$. Since the model assumes that the leeward side of the gaseous stream is tangent to the edge of the disk, the orientation of the disk indirectly affects the visibility conditions for the bright part of the hot line from both its windward and leeward sides.

Figure 2 combines all 20 average light curves obtained by Schoembs *et al.* [17]. It is apparent that the shape of the curves is essentially reproduced from cycle to cycle and that the curves fluctuate about the average position. The variations are largest near the primary and secondary minima, and are somewhat smaller near the orbital peak. Note that the secondary minimum in this system is basically due to the effects of the eclipse of the hottest part of the shock wave by the edge of the disk from its windward side, rather than to eclipses of the red dwarf, whose luminosity is very low.

The procedure of matching all the synthesized light curves to the same flux $F_{14}^{th}(0.25)$ enables us to determine the component whose variations mainly affect the amplitude of the orbital peak and the depth of the primary minimum of the light curves.

To obtain quantitative estimates, we selected four reference points in the light curves, at phases $\varphi \sim 0.0$ (primary minimum), 0.13 (egress from the eclipse and the region around the secondary maximum of the flux from the hot line), 0.55 (close to the secondary minimum of the flux from the hot line, specified by the eclipse of the line by the disk edge), and 0.83 (the maximum of the peak, the region adjacent to the primary maximum of the hot-line flux). Figure 2 presents the positions of various components at these phases. The real times of the maxima and minimum of the curves may differ by $\Delta\varphi \sim \pm 0.06$–$0.08$ to one or the other side of the selected average positions. Such deviations often indicate the presence of flares in the light curves.

The asymmetrical shape of the eclipse (the steep ingress into eclipse and smoother egress from eclipse) is consistent with the fact that the projections of the hottest regions of the disk and hot line onto the plane of the sky are displaced from the line connecting the centers of the stars. In the case of a circular disk, the center of its eclipse (either total or partial) would be at phase $\varphi = 0.0$, as would the center of the white-dwarf eclipse. The elliptical shape of the disk shifts the phase of the deepest eclipse by $\Delta\varphi \sim 0.005$ from phase $\varphi = 0.0$. The center of the hot-line eclipse is shifted by an even larger amount ($\Delta\varphi \sim 0.04$ from phase $\varphi = 0.0$).

In cycle $N = 8$, a substantial decrease of the system flux in the primary minimum is observed compared to the adjacent cycles. The analysis of the contributions from the components (Fig. 1b) indicates

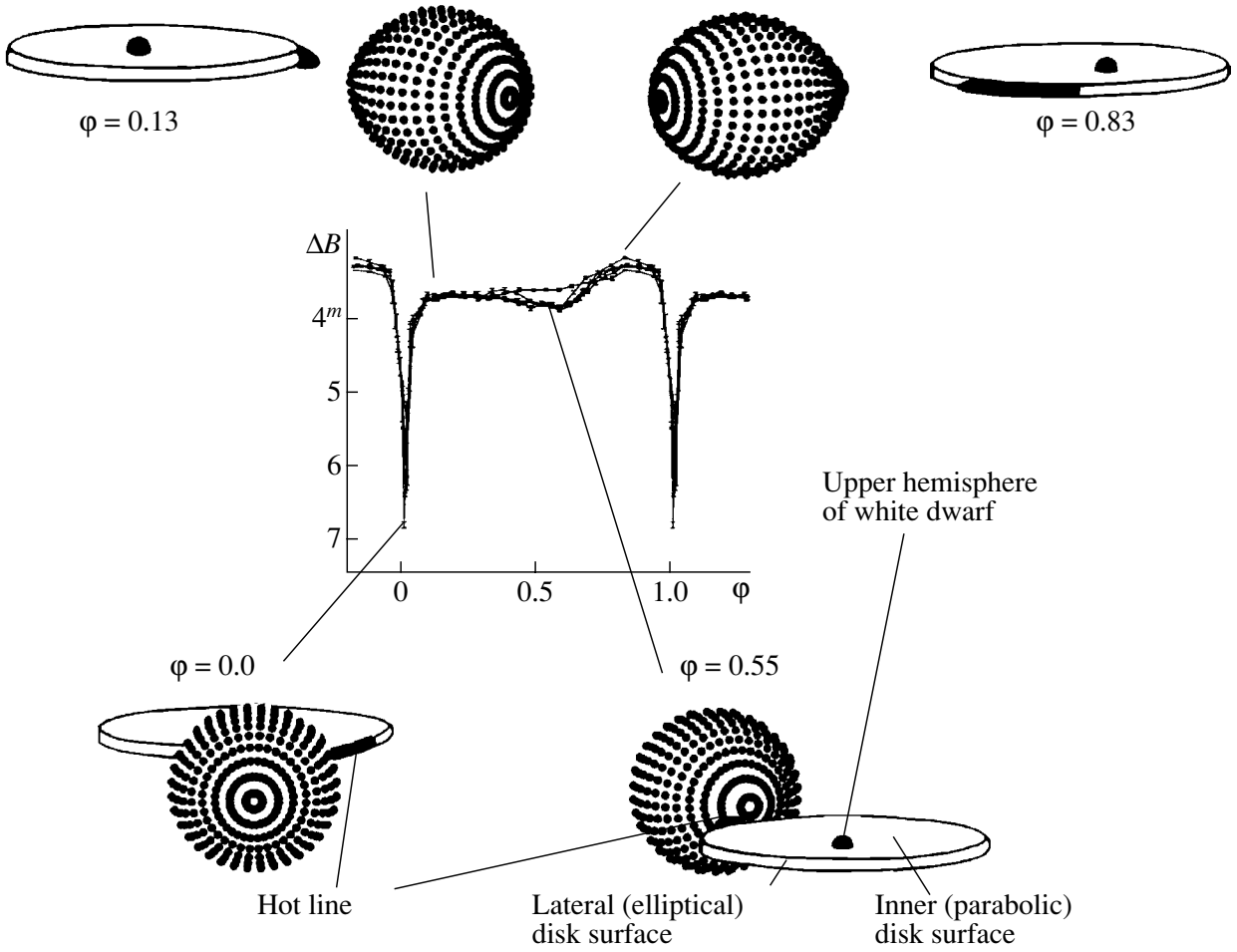

Fig. 2. The red dwarf, disk (the contours of the disk edge are shown schematically), and the hot line (its surface is shaded for better contrast) at various phases of the orbital cycle (at reference points; see the text). The sum of all 20 average light curves obtained by Schoembs *et al.* [17] is presented in the center.

that the luminosity of the disk in cycle $N = 8$ decreased by factors of 2.3 and 3.2 compared to its luminosity in the adjacent cycles $N = 7$ and 9, respectively. We can see from Fig. 2 that the disk eclipse is partial. However, the main flux comes from the inner regions of the disk, which are heated to temperatures > 5000 K, while the outer parts of the disk, whose temperature is comparable to that of the red dwarf ($T_d \sim 2000$–3000 K), do not contribute appreciably to the total flux. The temperature decrease along the radius of the disk is rather steep—the hottest regions of the disk with temperatures > 5000 K are no further than $(0.20$–$25)R_d$ from the white dwarf. Therefore, the maximum temperatures of the inner parts of the disk in cycles $N = 7$ and 9 are $\sim 22\,500$–$24\,300$ K, while the maximum temperature in cycle $N = 8$ is $\sim 18\,300$ K (Table 2). When the temperature of the inner parts of the disk decreases, so does the size of the central part of the disk giving rise to the bulk of the flux (the average radius of the radiating region in cycle $N = 8$ is $\sim 0.16a_0$, while it is $0.21a_0$ and $0.23a_0$ in cycles 7 and 9, respectively). Consequently, the residual flux from the disk during its eclipse by the red dwarf also decreases. This is precisely the reason for the substantial increase of the depth of the eclipse in the primary minimum in the $N = 8$ light curve.

Figures 3a–3f display the dependences between the observed maximum ($\varphi \sim 0.83$) and minimum ($\varphi \sim 0.0$) fluxes from the study of Schoembs *et al.* [17] and the calculated fluxes from the disk (Figs. 3a, 3d), the hot line (Figs. 3b, 3e) and their sum (Figs. 3c, 3f) at the corresponding phases. The theoretical fluxes F are given in arbitrary units. The squares mark light curves whose shapes are distorted by small flares.

These figures show that the height of the orbital peak depends on the combined contribution of the radiation from the disk and the hot line (Fig. 3c). The scatter of the dependences between the fluxes observed at the light-curve maxima and the calculated fluxes from the disk or hot line (Figs. 3a, 3b) is rather

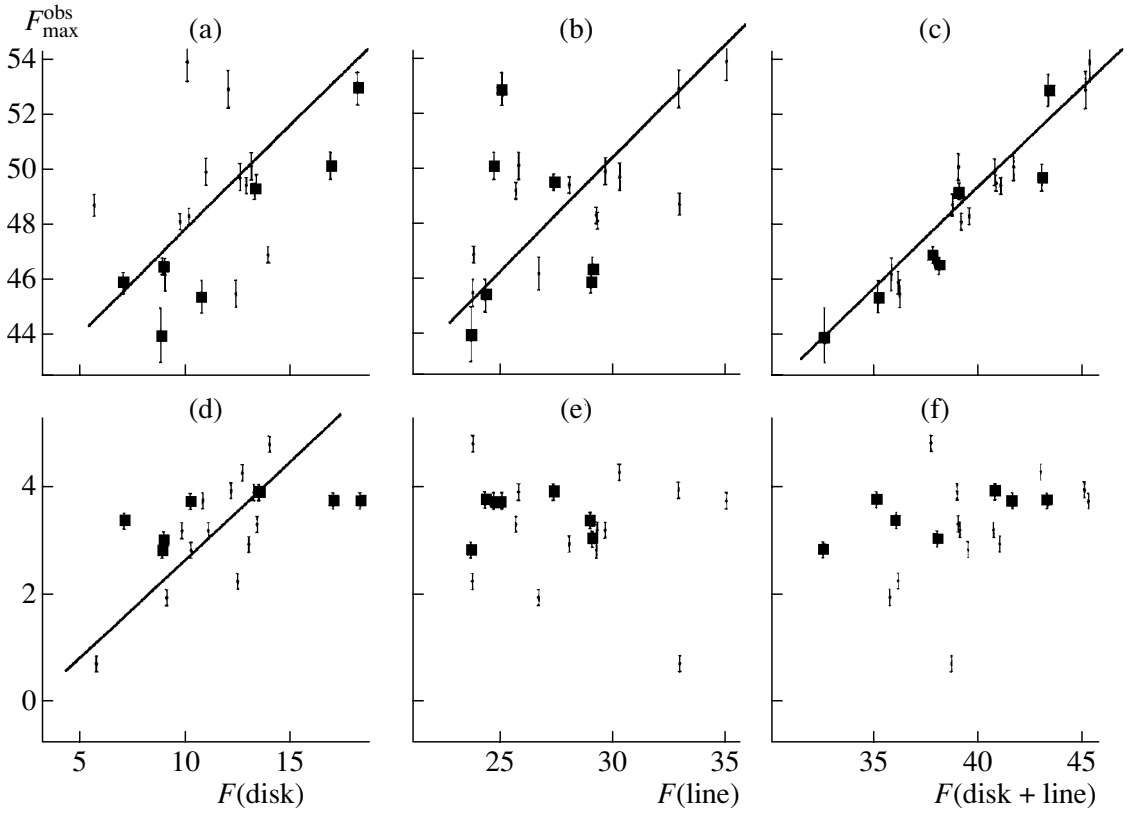

Fig. 3. (a–c) Relationships between the observed flux (in arbitrary units) at phases 0.80–0.86 (the orbital peak) and the theoretical fluxes (in arbitrary units) at phase $\varphi = 0.83$ from (a) the disk, (b) the hot line, and (c) the sum of these two components, calculated with the parameters from Table 2; (d–f) the same dependences for the fluxes observed in the primary minimum ($\varphi \sim 0.99$–1.01) and calculated for phase $\varphi = 0.0$.

large; nevertheless, some correlation can be seen. The flux in the primary minimum is specified only by the flux from the disk (Fig. 3d). There is no relationship between the observed flux in the primary minimum and the flux from the hot line (Figs. 3e, 3f). This is apparently due to the fact that the fairly extended accretion disk is partially eclipsed in the minimum (Fig. 2), whereas the eclipse is almost total for the relatively small hot portion of the shock.

Attempts to fit the orbital light curves of Schoembs *et al.* [17] with models with a hot spot on the side of a circular disk [33] were not successful. For each curve $N = 1$–20, the minimum residual is $\chi^2 \geq 700$. The shapes of the light curves in this model are similar to those in Fig. 4. It is evident that the hot-spot model can adequately reproduce the shape of the eclipse; however, it is unable to fit the out-of-eclipse parts of the orbital light curves with sufficient accuracy. The orbital light curves $N = 1$–20 from [17] are described considerably better using the hot-line model: the residual χ^2 does not exceed $\chi^2 \sim 270$ for light curves $N = 1$–20; it is lower than the critical χ^2 level for the $N = 14$ curve, and is comparable to the corresponding $\chi^2_{0.001,n}$ for the $N = 1$, $N = 11$, and $N = 17$ curves.

Table 3 presents the parameters of the disk and hot-line models derived from the U, B, R ($\lambda_{\text{eff}} =$ 6517 Å), and white light ($\lambda_{\text{eff}} = 4960$ Å, W) OY Car light curves of Wood *et al.* [29], which were averaged over several dozen orbital cycles. When the calculated parameters for the B curve (Tables 2 and 3) and the shape of the average B light curve [29] are compared to the individual orbital curves [17], it is obvious that the average light curve is close to the least perturbed individual orbital curves in this filter, for example, to the $N = 13$ curve. The upper part of Table 3 presents the results for the average light curves of OY Car using the hot-line model; the lower part presents the parameters obtained for the hot-spot model [33]. The errors of the last decimal places of the corresponding parameters calculated for an arbitrary residual level exceeding the minimum residual by 10% are given in parentheses. The minimum residual in the hot-spot model is more than a factor of 1.5 higher than in the hot-line model.

Figure 4a presents the averaged U, B, W, and R light curves from Wood *et al.* [29]. The solid curves

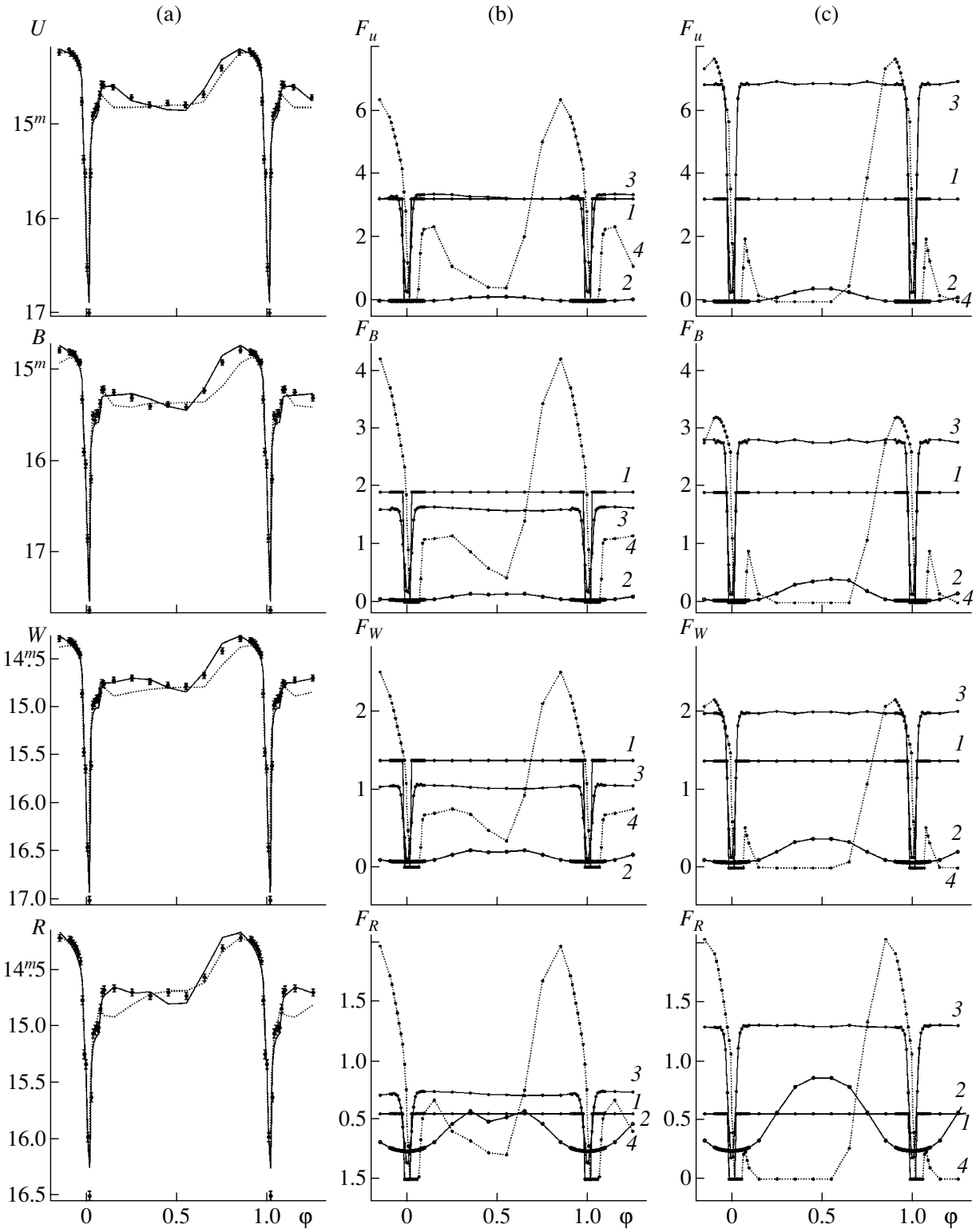

Fig. 4. Interpretation of the U, B, R, and white light (W) light curves of OY Car in the inactive state averaged over several orbital cycles, according to Wood *et al.* [29]. (a) Observations of [29] (points) and theoretical light curves synthesized for the hot-line (solid curves) and hot-spot (dashed curves) models. (b, c) Contributions to the total flux from the white dwarf (*1*), donor star (*2*), elliptical disk (*3*), and region of energy release (*4*) (hot line (b) or hot spot (c)). The flux is given in arbitrary units.

Table 3. Theoretical parameters of OY Car in its inactive state, derived from the U, B, W, R light curves of [29] averaged over several orbital cycles in the hot-line and hot-spot models

Parameter	U	B	W	R
Hot-line model				
Disk				
a/a_0	0.367(1)	0.361(1)	0.348(1)	0.350(1)
$a_{\max}/\xi$	0.596(1)	0.593(1)	0.577(1)	0.578(1)
e	0.164(2)	0.178(1)	0.188(1)	0.181(1)
α_e, deg	119(2)	129(2)	147(2)	136(3)
α_g	0.70(3)	0.68(3)	0.73(2)	0.74(1)
T_b, K	27 320(1000)	22 960(1200)	22 465(1100)	23 150(1050)
Hot line				
a_v/a_0	0.090(4)	0.055(3)	0.054(3)	0.069(4)
b_v/a_0	0.349(1)	0.326(1)	0.356(1)	0.384(2)
c_v/a_0	0.0276(1)	0.0192(1)	0.0182(1)	0.0214(1)
$T^{(1)}_{\max}$, K	13 543(2400)	16 680(2500)	15 615(2340)	15 140(2230)
$T^{(2)}_{\max}$, K	11 285(450)	12 655(400)	10 895(480)	11 375(540)
$\langle T^{(1)}\rangle$, K	7460	7615	6750	8090
$\langle T^{(2)}\rangle$, K	7245	6900	6235	7465
χ^2	168	207	186	204
Hot-spot model				
Disk				
r_d/a_0	0.278(1)	0.394(1)	0.284(1)	0.249(1)
r_d/ξ	0.388(1)	0.550(1)	0.397(1)	0.348(1)
T_b, K	30 740(1250)	26 380(1100)	24 940(1000)	25 825(1540)
Hot spot				
r_{sp}/a_0	0.095(5)	0.038(2)	0.057(4)	0.049(3)
α_{sp}, deg	40(6)	30(5)	43(6)	54(6)
T_{sp}	7130(220)	9300(150)	7510(200)	14 670(500)
χ^2	320	353	290	308

Note: The W light curve was obtained in white light ($\lambda_{\text{eff}} = 4960$ Å). The parameters of the disk and the region of energy release (hot line or hot spot) were obtained for fixed $q = M_1/M_2 = 9.8$, $i = 82°$, $T_2 = 3000$ K, $T_1 = 15\,000$ K, $R_1 = 0.0182a_0$. The maximum and minimum radii of the disk for the known e are determined from the formulas $a_{\max} = a(1+e)$ and $a_{\min} = a(1-e)$, where a is the semimajor axis of the disk. For all curves, the flaring angle of the outer edge of the disk is roughly the same in both models, $\beta_d = 3°.8–4°.1$, the parameter $y_{\min} = 0.28(2)a_0$, and the shift of the center of the hot region on the windward side of the line $\Delta y = 0.03(1)a_0$. In the hot-line model, $\alpha_g = 0.74(1)$ for all light curves.

show theoretical light curves synthesized for the hot-line model using the parameters from Table 3. Figure 4b presents the contributions of the white and red dwarfs, the disk, and the region of energy release (i.e., the hot line) to the total flux in the hot-line model in arbitrary units. It is clear that the red dwarf's contribution to the total flux in the blue (U and B) is negligible in this model ($< 2\%$). The contribution of the secondary increases to 3.5% in white light (W), and to 13.7% in R. The contribution from the

white dwarf is $\sim$24–25% in the blue and $\sim$30% in white light, decreasing to $\sim$16% in R. The maximum contribution from the disk is reached in U ($\sim$25%); in the other filters, it is $\sim$21–22% of the maximum flux from the system. The variations of the system's brightness at orbital phases $\varphi \sim 0.15$–0.85 are primarily determined by variations in the flux from the hot-line surface. It follows from Table 3 that the longitude of the disk periastron increases (by $\sim 30°$) in the transition from blue to red wavelengths. It is also possible that the different α_e in the red and blue are related to different contributions from components that were not taken into account in the model, such as the stream flowing out from the red dwarf, whose contribution increases in the red.

The lower part of Table 3 contains the results for the averaged light curves of OY Car obtained with the hot-spot model. Figure 4a (dashed curves) presents theoretical light curves synthesized in four filters for the best-fit parameters of the hot-spot model. Comparison of the theoretical curves indicates that the shape of the eclipse is described in a similar way in both models. The differences between out-of-eclipse portions of the light curves, particularly the shapes of the peak, are appreciably larger (Fig. 4a). In the hot-spot model, the contributions from the disk and white dwarf (Fig. 4c) are constant at phases $\varphi \sim 0.22$–0.67, the hot spot is not visible, and the model is unable to fit the observed light curves accurately. The contribution from the red dwarf is insignificant in the blue due to the low temperature and relatively small size of the star; as a result, the light curves display a flat portion at orbital phases $\varphi \sim 0.1$–0.6. In white light and R, the flux from the red dwarf becomes comparable to that from the white dwarf and disk, and determines the shape of the W and R light curves at phases $\varphi \sim 0.1$–0.6.

In the hot-line model, fluctuations of the out-of-eclipse flux are specified primarily by variations of the contribution from the shock. In all four filters, the contribution to the total flux from the shock front is fairly substantial (at the maximum, it is 25–35% of the radiation of the leeward side of the line), and it never becomes zero. Therefore, individual portions of the region of energy release are also visible at phases at which the hot spot cannot be seen. Due to the small eccentricity of the disk, the flux from the disk is constant at orbital phases at which it is not eclipsed by the red dwarf. The hot region at the edge of the stream in the vicinity of the accretion disk is not totally eclipsed in any of the considered portions of the light curve ($\varphi \sim 0.2$–0.7). At phases $\varphi \sim 0.1$–0.3, we see the radiation from the windward side of the hot line, from peripheral portions of the compact region heated by the shock. The hottest region is screened from the observer by the edge of the disk. Starting with phase $\varphi \sim 0.55$, we begin to see the radiation from the leeward side of the line in the hot-line model. Since the region of interaction is rather extended in this model, its projection onto the plane of the sky varies with orbital phase more smoothly than in the case of a quasiflat hot-spot surface, thus leading to the larger width of the orbital peak (cf. Figs. 4b, 4c).

5. INFRARED LIGHT CURVES OF OY Car

Sherrington *et al.* [21] obtained J (1.25 micron) observations of OY Car on April 25, 1980 and J and K (2.2 micron) observations on January 26, 1981. On April 25, 1980, OY Car was in its inactive state, while the system underwent a small flare in the J filter by $\sim 0\overset{m}{.}35$ on January 26, 1981. All the IR light curves display two pronounced minima during the orbital cycle, the shallower secondary minimum being at phase $\varphi \sim 0.5$. The depths of the primary minimum in the J light curves were $\sim 0\overset{m}{.}8$ in April 1980 and $\sim 1\overset{m}{.}0$ in January 1981 (they were $\sim 0\overset{m}{.}7$ in the K filter in the same period of time).

After removing the ellipsoidal curve for the variability of the secondary from the observed J light curves, Sherrington *et al.* [21] discovered that the secondary minimum essentially disappeared in the April J light curve, whereas it remained in the January J light curve (at the maximum of the small flare). The $J-K$ color index in the inactive state was $J-K = 0\overset{m}{.}93 \pm 0\overset{m}{.}15$; during the flare, it decreased to $J-K = 0\overset{m}{.}35 \pm 0\overset{m}{.}15$. The first value corresponds to a disk with a cool outer edge, while the second corresponds to a substantially hotter edge. The outer ring of the disk and the secondary make a substantial contribution to the system's flux at wavelengths $\lambda > 8000$ Å. The secondary alone contributes from 30 to 60% of the total IR flux, according to the estimates of [21].

We considered all three OY Car light curves presented by Sherrington *et al.* [21] in both the hot-line and hot-spot model. The observational data were taken from the plots presented in [21]. The April 25, 1980 J curve contains 330 individual observations, and the averaged curve 24 points; the January 26, 1981 J and K curves contain 405 and 108 observations, respectively, and the averaged curves 28 and 17 points. The rms errors of the averaged J curves are roughly equal: $\sigma \simeq 0\overset{m}{.}01$–$0\overset{m}{.}02$.

The K curve contains fewer observations and their scatter is higher; as a result, $\sigma \simeq 0\overset{m}{.}02$–$0\overset{m}{.}03$. A drift due to the small flare was subtracted from the J data for January 26, 1981 (no drift is seen in the K curve). The upper parts of Figs. 5 and 6 present the light curves used to derive the system parameters at IR wavelengths. The bars to the right of each plot

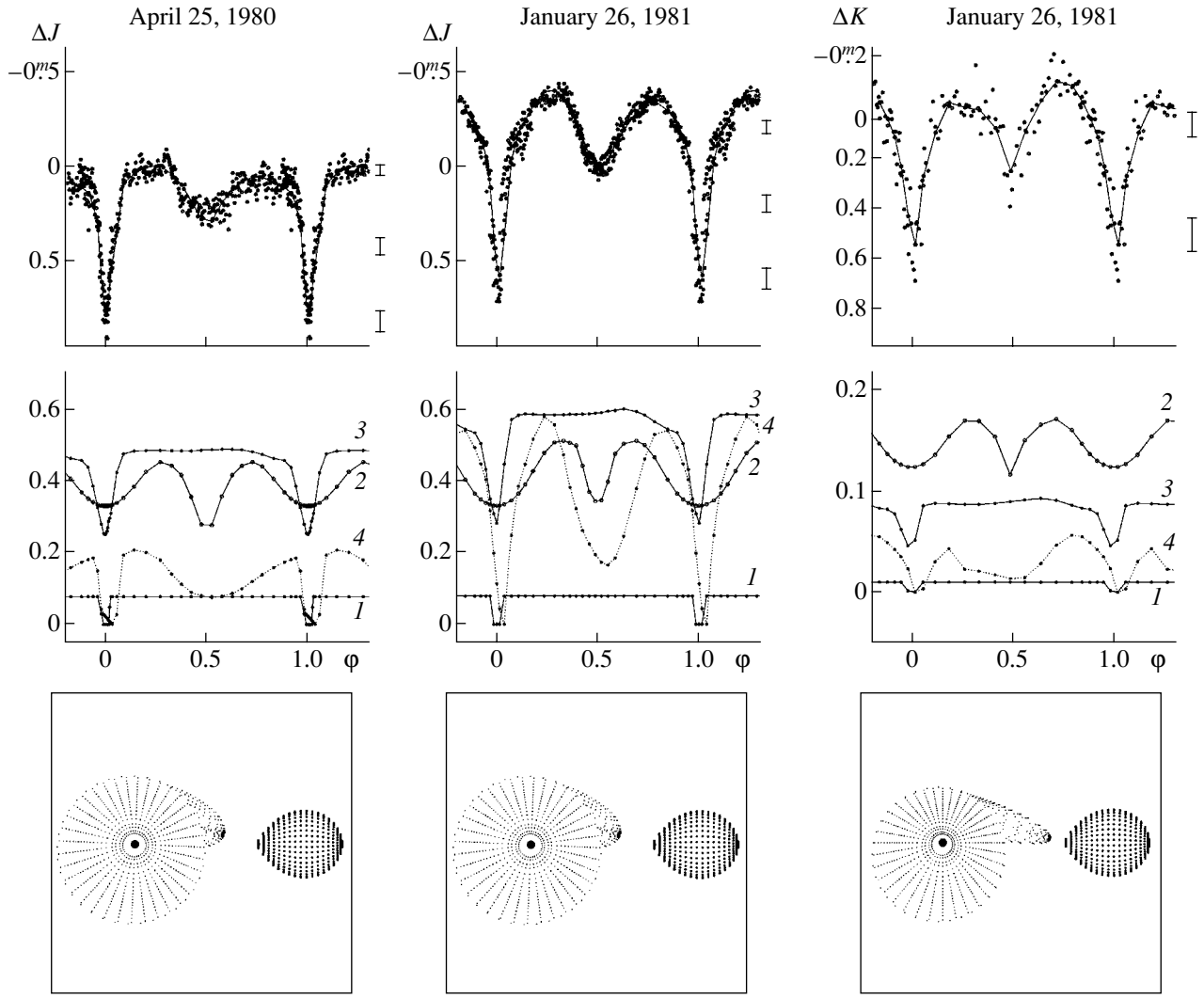

Fig. 5. Upper plots: the J and K observations of OY Car from Sherrington *et al.* [21] in the inactive state of the system on April 25, 1980 and during the small flare on January 26, 1981. The solid curves indicate the light curves synthesized in the hot-line model. The bars to the right of the plots indicate the mean errors of individual observations in the corresponding magnitude interval. The averaged plots present the contributions from various components to the total flux (in arbitrary units): the white dwarf (*1*), donor star (*2*), elliptical disk (*3*), and hot line (*4*). Lower plots: simulated images of OY Car (viewed from above) in the hot-line model, calculated with the parameters from Table 4.

indicate the mean error of the individual observations in the corresponding magnitude interval.

Both J light curves display a peculiar shape—the flux from the system before the ingress into the primary eclipse is slightly lower than immediately after the egress from the eclipse. In the hot-spot model, an additional source of radiation must be invoked to explain this.

To restrict the range of allowed system parameters in the IR, we took into account the homogeneity of both the J light curves. Both observed curves were shifted by $\delta J = 14\overset{m}{.}4$, which is the first-quadrature J flux obtained on April 25, 1980. Accordingly, we used the first-quadrature intensity corresponding to the best-fit parameters obtained for the J light curve of April 25, 1980 to translate the fluxes into magnitudes in the calculated trial theoretical light curves for both J light curves.

As for the B light curves of OY Car, the main system parameters were fixed using the values in Table 1. Table 4 presents the derived parameters of the disk and hot line. The maximum radius of the disk at near-IR wavelengths is roughly the same in the inactive state and during the weak flare ($a_{\max}/\xi \sim 0.67$–0.69). In the unperturbed state, the disk is almost circular, and the region of energy release is close to the edge of the disk and spans almost 60° in azimuth. The main contribution to the total flux (see the middle part of Fig. 5) is from the red dwarf,

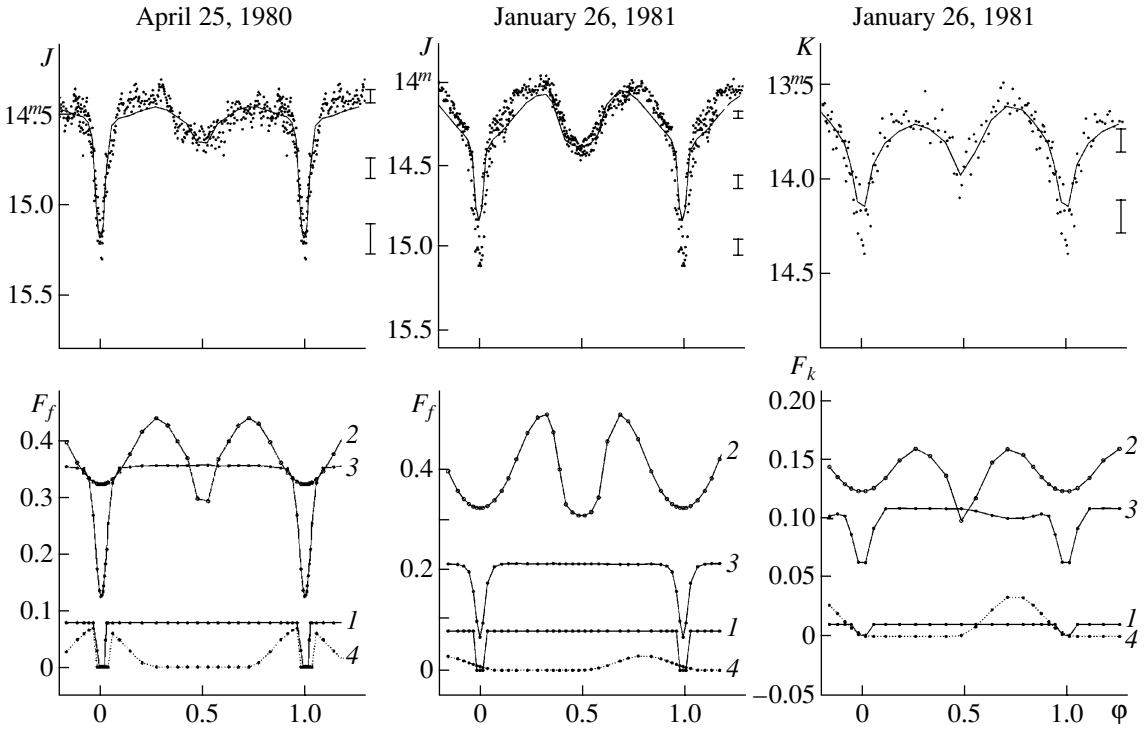

Fig. 6. Upper plots: the J and K observations of OY Car from Sherrington *et al.* [21] in the inactive state of the system on April 25, 1980 and during the small flare on January 26, 1981. The solid curves indicate the light curves synthesized with the best-fit parameters (Table 4) from the hot-spot model. Lower plots: the contributions from various components to the total flux (in arbitrary units): the white dwarf (*1*), donor star (*2*), elliptical disk (*3*), and hot spot (*4*).

whose polar areas are heated by hot radiation from the inner regions of the disk (from ∼30% to ∼54% of the total flux), and the disk (∼40% of the maximum total flux). The contribution of the white dwarf to the total flux is insignificant (about 6–8%). The contribution from the windward side of the hot line is slightly higher than from the leeward side—∼18% and ∼15%, respectively—resulting in the anomalous shape of the light curve. The brightness temperature of the hot line at the shock front reaches ∼40 000 K, which is not surprising, since the radiation has a recombination rather than blackbody origin. However, the size of this region is small, and the temperature falls very quickly to ∼3200 K with distance from the disk edge. As a result, the flux from this region is only 3% higher than the flux from the leeward side of the line, where the matter is heated on average to 3600 K, but the energy-release region spans almost 60° in azimuth. Since our assumption that the hot line emits a Planck spectrum is rather crude, the brightness temperature of the line should be considered a formal parameter.

During the small flare (see the bottom part of Fig. 5, where the comparative sizes of the disk and hot line are presented), a condensation is observed in the region of the disk close to the trajectory of the gaseous stream (formally, this is shown by the fact that the disk acquires the eccentricity $e \simeq 0.18$). In addition, the contribution from the hot line increases substantially (to 34% of the maximum flux), basically due to the increase in the size of the region of energy release. As in the inactive state, the contribution from the windward side of the line in the J filter is slightly higher (by ∼2%) than that from the leeward side, resulting in a slight asymmetry of the brightness maxima in the J light curve. Despite the fact that the absolute flux from the disk increases by ∼10% in this observational period, its relative contribution to the total flux decreases by ∼5–6% due to the increase of the flux from the hot line.

The parameters of the disk and hot line derived from the K light curve of OY Car (Table 4) are roughly the same. The increase of the brightness temperature of the hot line in the transition from the J to the K filter is apparently due to the deviation of the radiation from blackbody in this region and the contribution of free–free transitions to the observed radiation. As was noted in [12], where we analyzed light curves of the cataclysmic variable IP Peg, the hot-line radiation includes a substantial contribution from thermal bremsstrahlung and recombination radiation, whose fraction appreciably increases with increasing wavelength compared to the blackbody contribution.

Table 4. Theoretical parameters of OY Car in the IR derived from the light curves of [21]

Parameter	J	J	K
	April 25, 1980	January 26, 1981	January 26, 1981
Hot-line model			
a/a_0	0.440	0.401	0.374
$a_{\max}/\xi$	0.673	0.662	0.689
e	0.094	0.183	0.320
α_e, deg	57.46	70.00	82.00
α_g	0.508	0.586	0.629
T_b, K	16 265	21 395	20 945
a_v/a_0	0.183	0.111	0.064
b_v/a_0	0.424	0.562	0.515
c_v/a_0	0.013	0.022	0.015
$T^{(1)}_{\max}$, K	40 090	26 775	41 415
$T^{(2)}_{\max}$, K	4180	9635	12775
$\langle T^{(1)} \rangle$, K	19 290	13 575	13 100
$\langle T^{(2)} \rangle$, K	3660	6280	6175
$y_{\min}/a_0$	0.385	0.446	0.343
χ^2	197	205	10.8
Hot-spot model			
r_d/a_0	0.402	0.643	0.398
r_d/ξ	0.288	0.898	0.556
α_g	0.504	0.75	0.50
T_b, K	15 155	21 215	15 740
r_{sp}/a_0	0.025	0.365	0.134
α_{sp}, deg	4.79	69.30	87.01
T_{sp}, K	6750	4415	5300
χ^2	350	824	84.5

Note: The parameters of the disk and hot line (hot spot) were derived for fixed $q = M_1/M_2 = 9.8$, $i = 82°$, $T_2 = 3000$ K, $T_1 = 15\,000$ K, $R_1 = 0.0182a_0$. The flaring angle of the outer edge of the disk for all curves in both models is $\beta_d = 2°.5–3°.7$.

In the hot-spot model, the resulting residual for the J and K light curves ($\chi^2 \sim 350$, ~ 824 and 84.5 for the two J light curves and the K light curve, respectively; see Fig. 6, Table 4) is substantially higher than in the hot-line model ($\chi^2 \sim 194$, ~ 139 and 9.58, respectively). This is primarily due to the inconsistency between the observations and the theoretical depth of the primary minimum (for light curves obtained during the flare), as well as the flux near quadrature. In our model, the J light curves were analyzed independently in order to obtain the minimum residual. However, even in this approach, the derived azimuth of the hot spot does not coincide with the values calculated assuming the gaseous stream follows the ballistic trajectory for a particle ejected from the inner Lagrange point [29] for $q \simeq 10.0$ and that the hot spot should be located at the point where the ballistic trajectory intersects the edge of the disk ($\alpha_{sp} \sim 32°–36°$). Finally, as expected, this model is unable to describe the anomalous shape of the J light curves, in both the inactive state and during the flare.

6. CONCLUSION

Our interpretation of eclipsing light curves of the cataclysmic variable OY Car using two alternative models indicates that the hot-line model describes the observed light curves in the inactive state of the system substantially better than the hot-spot model. The hot-line model better reproduces the width of the peaks in the light curves, the shape of the eclipse, and the details of out-of-eclipse brightness variations. The hot-spot model for a system with a very high component mass ratio is unable to describe the out-of-eclipse brightness variations in the optical orbital curves. In this case, the contribution from the radiation of the red dwarf is negligible, the out-of-eclipse fluxes from the disk and the white dwarf are constant, and the only source of out-of-eclipse variations is the hot spot at phases 0.7–0.9. Due to the possibility of varying the parameters of the shock—the temperature and size of the region of energy release—and also due to the location of the energy-release region outside the disk, the hot-line model is able to reproduce the shape of out-of-eclipse portions of the light curves for this SU UMa-type system, which can vary in the transition from one orbital cycle to another. Unlike the hot spot, relatively bright regions of the hot line can also be observed at phases $\varphi \sim 0.5$–0.6, when the hot spot at the point of contact between the stream from L_1 and the disk is not visible. Finally, with an appropriate orientation of the elliptical accretion disk, an increase of the flux from the system at phases $\varphi \sim 0.1$–0.2 will be observed due to the radiation from the windward side of the hot line, which is completely ruled out in terms of the standard model.

The advantages of the hot-line model over the hot-spot model are manifest in each of the 20 individual B light curves of OY Car in the quiescent state, in spite of the substantial variations of these light curves from period to period. In all 20 individual curves, we can see the trend for an increase of the flux in the primary minimum with increasing luminosity of the accretion disk. The flux at the maximum of the orbital peak increases linearly with the increase of the total contribution from the disk and hot line.

Our analysis of IR light curves of OY Car confirms the advantages of the hot-line model, which can explain the anomalous IR light curves of this system in a natural way.

7. ACKNOWLEDGMENTS

This work was supported by the Russian Foundation for Basic Research (project nos. 02-02-16462, 02-02-17524, 02-02-16088), the INTAS Foundation (grant no. 00-491), the State Science and Technology Project "Astronomy," Presidential Grants of the Russian Federation (00-15-96722, 00-15-99311), and the State Science and Technology Project "Universities of Russia" (grant 5558).

REFERENCES

1. V. G. Gorbatskiĭ, Astrofizika **3**, 245 (1967).
2. J. Smak, Acta Astron. **20**, 312 (1970).
3. B. Warner, *Cataclysmic Variable Stars* (Cambridge Univ. Press, Cambridge, 1995).
4. D. V. Bisikalo, A. A. Boyarchuk, O. A. Kuznetsov, and B. M. Chechetkin, Astron. Zh. **74**, 880 (1997) [Astron. Rep. **41**, 786 (1997)].
5. D. V. Bisikalo, A. A. Boyarchuk, O. A. Kuznetsov, and B. M. Chechetkin, Astron. Zh. **74**, 889 (1997) [Astron. Rep. **41**, 794 (1997)].
6. D. V. Bisikalo, A. A. Boyarchuk, V. M. Chechetkin, *et al.*, Mon. Not. R. Astron. Soc. **300**, 39 (1998).
7. D. V. Bisikalo, A. A. Boyarchuk, O. A. Kuznetsov, *et al.*, Astron. Zh. **75**, 706 (1998) [Astron. Rep. **42**, 621 (1998)].
8. D. V. Bisikalo, A. A. Boyarchuk, B. M. Chechetkin, *et al.*, Astron. Zh. **76**, 905 (1999) [Astron. Rep. **43**, 797 (1999)].
9. D. V. Bisikalo, A. A. Boyarchuk, B. M. Chechetkin, and O. A. Kuznetsov, Astron. Zh. **77**, 31 (2000) [Astron. Rep. **44**, 26 (2000)].
10. M. Makita, K. Miyawaki, and T. Matsuda, Mon. Not. R. Astron. Soc. **316**, 906 (2000).
11. D. V. Bisikalo, A. A. Boyarchuk, O. A. Kuznetsov, *et al.*, Astron. Zh. **75**, 40 (1998) [Astron. Rep. **42**, 33 (1998)].
12. T. S. Khruzina, A. M. Cherepashchuk, D. V. Bisikalo, *et al.*, Astron. Zh. **78**, 625 (2001) [Astron. Rep. **45**, 538 (2001)].
13. C. Hoffmeister, Veroff. Sternwarte Sonneberg **6** (1), 5 (1963).
14. N. Vogt, R. Schoembs, W. Krzeminski, and H. Pedersen, Astron. Astrophys. **94**, L29 (1981).
15. N. Vogt, Astron. Astrophys. **128**, 29 (1983).
16. R. Schoembs and K. Hartmann, Astron. Astrophys. **128**, 37 (1983).
17. R. Schoembs, H. Dreier, and H. Barwig, Astron. Astrophys. **181**, 50 (1987).
18. M. C. Cook, Mon. Not. R. Astron. Soc. **215**, 211 (1985).
19. G. Berriman, Mon. Not. R. Astron. Soc. **207**, 783 (1984).
20. G. Berriman, Mon. Not. R. Astron. Soc. **210**, 223 (1984).
21. M. R. Sherrington, R. F. Jameson, J. Bailey, and A. B. Giles, Mon. Not. R. Astron. Soc. **200**, 861 (1982).
22. J. Bailey and M. Ward, Mon. Not. R. Astron. Soc. **194**, 17P (1981).
23. K. V. Hessman, D. Koester, R. Schoembs, and H. Barwig, Astron. Astrophys. **213**, 167 (1989).
24. E. T. Harlaftis and T. R. Marsh, Astron. Astrophys. **308**, 97 (1996).
25. W. Krzeminski and N. Vogt, Astron. Astrophys. **144**, 124 (1985).
26. R. Schoembs, Astron. Astrophys. **158**, 233 (1986).
27. A. Bruch, D. Beele, and R. Baptista, Astron. Astrophys. **306**, 151 (1996).
28. G. Berriman, Mon. Not. R. Astron. Soc. **228**, 729 (1987).

29. J. H. Wood, K. Horne, G. Berriman, and R. A. Wade, Astrophys. J. **341**, 974 (1989).
30. T. Hamada and E. E. Salpeter, Astrophys. J. **134**, 683 (1961).
31. J. Smak, Acta Astron. **34**, 317 (1985).
32. T. S. Khruzina, Astron. Zh. **78**, 298 (2001) [Astron. Rep. **45**, 255 (2001)].
33. T. S. Khruzina, Astron. Zh. **75**, 209 (1998) [Astron. Rep. **42**, 180 (1998)].
34. K. V. Hessman, K.-H. Mantel, H. Barwig, and R. Schoembs, Astron. Astrophys. **263**, 147 (1992).
35. O. A. Kuznetsov, D. V. Bisikalo, A. A. Boyarchuk, *et al.*, Astron. Zh. **78**, 997 (2001) [Astron. Rep. **45**, 872 (2001)].

Translated by K. Maslennikov

Astronomy Reports, Vol. 47, No. 3, 2003, pp. 232–239. Translated from Astronomicheskiĭ Zhurnal, Vol. 80, No. 3, 2003, pp. 258–265.

A New Model of a Magnetar

I. F. Malov[1], G. Z. Machabeli[2], and V. M. Malofeev[1]

[1] *Astro Space Center, Lebedev Physical Institute, Russian Academy of Sciences, Leninskiĭ pr. 53, Moscow, 117924 Russia*

[2] *Abastumani Astrophysical Observatory, Academy of Sciences of Georgia, Gora Kanobili, Abastumani, 383762 Georgia*

Received May 25, 2002; in final form, October 10, 2002

Abstract—A new model is put forward to explain the observed features of anomalous X-ray pulsars (AXPs) and soft gamma-ray repeaters (SGRs). It is shown that drift waves can be excited in the magnetosphere of a neutron star with a rotational period of $P \sim 0.1$ s, surface magnetic field $B_s \sim 10^{12}$ G, and angle between the rotational axis and magnetic moment $\beta < 10°$. These waves lead to the formation of radiation pulses with a period of $P_{dr} \sim 10$ s. The rate of loss of rotational energy by such a star ($\sim 10^{37}$ erg/s) is sufficient to produce the observed increase in the period ($\dot{P} \sim 10^{-10}$), the X-ray luminosities of AXPs and SGRs ($\sim 10^{34}$–10^{36} erg/s), and an injection of relativistic particles into the surrounding supernova remnant. A modulation of the constant component of the radiation with a period of $P \sim 0.1$ s is predicted. In order for SGRs to produce gamma-ray bursts, an additional source of energy must be invoked. Radio pulsars with periods of $P_{\rm obs} > 5$ s can be described by the proposed model; in this case, their rotational periods are considerably less than $P_{\rm obs}$ and the observed pulses are due to the drift waves.

1. INTRODUCTION

Anomalous X-ray pulsars (AXPs) [1] and soft gamma-ray repeaters (SGRs) [2] were discovered in recent years, and their nature remains unclear. The presence of a periodic pulsed component in their radiation with a period of a few seconds suggests that the central object is most probably a single neutron star, since no signs of a companion were found. The table shows that the group of AXPs includes five reliably-identified objects and several candidates. These data were taken from the reviews and original papers [1–7]. The main difference of AXPs from other X-ray pulsars is the persistent deceleration of the rotational period by values 10^{-11}–10^{-13} s/s. In addition, AXPs are characterized by the following features:

(1) a fairly narrow range of periods (6–12 s);

(2) localization near the Galactic plane ($\langle|b|\rangle = 0.35°$);

(3) association with supernova remnants, in the case of three objects;

(4) more stable X-ray fluxes than in pulsars belonging to binary systems, and a range of X-ray luminosities (10^{34}–10^{36} erg/s) that is substantially less than for normal X-ray pulsars (10^{34}–10^{38} erg/s);

(5) a considerably softer spectrum than for other objects, which can usually be described by the sum of a blackbody component with energy $kT \approx$ 0.35–0.6 keV and a power-law component at higher energies with exponent 2.5–4.0.

The second group (SGRs) currently includes only four objects and one candidate (see the table). Their periods of rotation are in the same interval (5–8 s). In contrast to the AXPs, only SGR1900+14 has a persistent component of its X-ray emission. In the other objects, X-ray emission is observed either only in the quiescent state (SGR1627–41 and SGR1806–20) or, on the contrary, in periods of active gamma-ray emission (SGR0525–66). The rate of deceleration of SGRs is usually greater than for AXPs, and their ages seem lower. For example, the ages of two SGRs (SGR1806–20 and SGR1900+14) were estimated to be 1400 and 780 yr. All SGRs seem to be associated with supernova remnants, but, in contrast to AXPs, they are shifted from the centers, and the average velocities of SGRs are greater than those of AXPs (100 km/s for SGR1806–20 to > 1000 km/s for SGR1900+14). The most important peculiarity of SGRs is the presence of sporadic bursts of gamma radiation with flare energies up to 10^{44} erg [4]. Another important feature of the radiation of AXPs and SGRs is the presence of a constant (non-pulsed) component [4].

The magnetic fields of these objects estimated by assuming that their deceleration is due to magnetic-dipole radiation are $\sim 10^{14}$–10^{15} G, two orders of

1063-7729/03/4703-0232$24.00

Table

No.	Source	P, s	$\dot{P}$	$\log L_x \left(\frac{\text{erg}}{\text{s}}\right)$	$\log \dot{E} \left(\frac{\text{erg}}{\text{s}}\right)$
			AXP		
1	1E1048.1−5937	6.45	12.2×10^{-11}	34.30	33.51
2	1E2259+586	6.98	7.3×10^{-13}	34.90	31.93
3	4U0142+61	8.69	3×10^{-12}	34.90	32.26
4	RXSJ170849−4009	11.00	3×10^{-11}	35.95	32.95
5	1E1841−045	11.77	4.7×10^{-11}	35.48	33.06
7	1RXSJ130848.6+212708	5.16	$(0.7–2.0) \times 10^{-11}$	32.61	33.30–33.76
8	AXJ1845.0−0258	6.97		34.70	
9	0720−3125	8.39		31.48	
			SGR		
1	SGR0526−66	8.1		36–37	
2	SGR1806−20	7.48	8.3×10^{-13}	35.30	33.79
3	SGR1900+14	5.16	1.1×10^{-10}	34.48	34.50
4	SGR1627−41	6.4?		~ 35	
5	SGR1801−23				

magnitude greater than the fields in radio pulsars. In principle, such fields can exist inside a neutron star [3], and play an important part in the energetics of emission processes. Adopting the idea that the magnetic fields played the determining role in these objects, they were assigned to a special group of neutron stars—the so-called "magnetars" [3]. However, there are alternative mechanisms that can result in the loss of angular momentum of a neutron star and deceleration of its rotation (see, for example, [8]). Therefore, the accuracy of the derived magnetic-field estimates is not evident. Moreover, if such fields are present near the neutron-star surface, it is quite difficult to produce electron–positron pairs [5, 7], which are now commonly believed to be an obligatory intermediate stage in the generation of the observed emission of radio pulsars. This made it necessary to propose the existence of radio-quiet neutron stars (for example, [9]). Magnetars were included in this group. However, the pulsed radiation from SGR1900+14 [10] and AXP1E2259+586 [11] detected in 1999–2001, again raised the question of the nature of these objects. The problem can be formulated as follows: either we do not understand the basic processes for the formation of radiation in radio pulsars, or estimates of the extremely strong magnetic fields in the magnetars are incorrect. Note that, along with the concept of magnetars, a number of authors (see, for example, [12] and references therein) have tried to explain the observed features of AXPs and SGRs in models with accretion of matter from the surrounding medium onto a neutron star with a surface magnetic field typical of pulsars ($B_s \sim 10^{12}$ G).

Here, we propose a new model describing the magnetar phenomenon using magnetic fields of $B \sim 10^{12}$ G. Our models will be compared with observational data at the end of the paper.

2. BASIC FEATURES OF THE MODEL

According to the theory [13–19], transverse electromagnetic waves can be generated in a relativistic electron–positron plasma, filling the magnetosphere of a neutron star. These waves easily escape the magnetosphere and reach the observer. Their frequency depends on the pulsar period and can be both in the radio and at higher frequencies [13, 14]. The radiation generated in the magnetosphere must be separated into two parts—the eigenmodes and radiation in a one-particle approximation. The eigenmodes result from interference of the radiation by an ensemble of particles. In the second case, each particle of the ensemble is an independent source of radiation. In the first case, the wavelength λ is greater than the mean distance between the particles of the plasma with density n ($\lambda > n^{-1/3}$), and, in the second case, $\lambda < n^{-1/3}$.

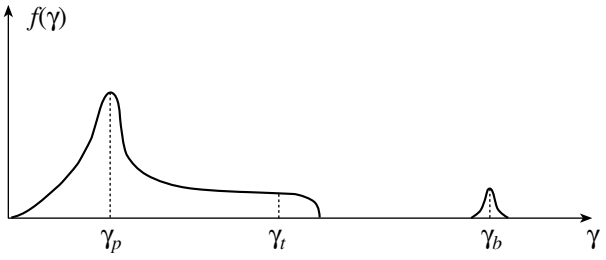

Fig. 1. Lorentz factor distribution for electrons in the magnetosphere of a neutron star.

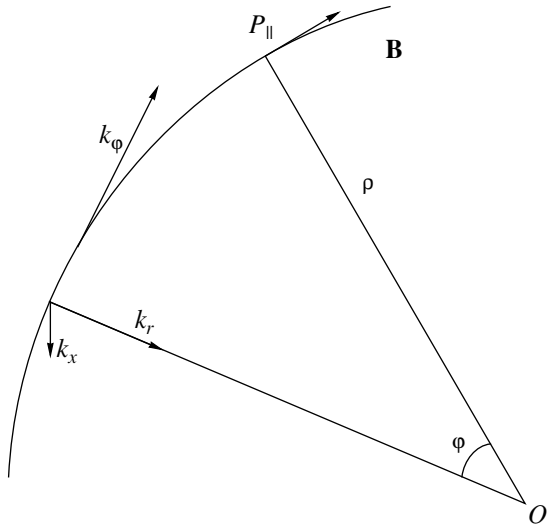

Fig. 2. Cylindrical coordinate system used.

As was already mentioned above, a necessary stage of the magnetospheric processes is the formation of an electron–positron plasma near the neutron-star surface. When $B_s \sim 10^{12}$ G, the particles lose their transverse momenta almost instantly (over times $< 10^{-15}$ s), so that their distribution function becomes one-dimensional and has the form shown in Fig. 1. The plasma is composed of three components: (1) the bulk of the plasma with density n_p and Lorentz factor γ_p, (2) a long tail with n_t and γ_t, and (3) the primary beam with n_b and γ_b. The general features of such a plasma are described, for example, in [20, 21].

Since this plasma is not gyrotropic, there are three branches that propagate approximately along the magnetic field. We shall be interested only in the purely transverse t mode, with the spectrum

$$\omega_t = kc(1-\delta), \tag{1}$$

where

$$\delta = \frac{\omega_p^2}{4\omega_B^2\gamma_p^3}, \tag{2}$$

$$\omega_p^2 = \frac{4\pi n e^2}{m}, \tag{3}$$

$$\omega_B = \frac{eB}{mc}, \tag{4}$$

and the mixed potential–nonpotential lt mode, with the spectrum

$$\omega_{lt} = k_\varphi c\left(1-\delta-\frac{k_\perp^2 c^2}{16\omega_p^2\gamma_p}\right). \tag{5}$$

There are two basic mechanisms for the generation of the t and lt eigenmodes: the resonance associated with the anomalous Doppler effect

$$\omega - k_\varphi v_\varphi - k_x u_x + \frac{\omega_B}{\gamma_r} = 0, \tag{6}$$

and the drift–Cherenkov resonance

$$\omega - k_\varphi v_\varphi - k_x u_x = 0. \tag{7}$$

The resonance conditions (6)–(7) and spectrum (5) are written in cylindrical coordinates (Fig. 2). Here,

$$u_x = \frac{cv_\varphi\gamma_r}{\rho\omega_B}, \tag{8}$$

where ρ is the radius of curvature of the field line and γ_r is the Lorentz factor of the resonant particles. These modes are generated within a small angle ($\frac{k_\perp}{k_\varphi} \ll 1$) near the tangent to a curved field line in the outer part of the magnetosphere, where the field lines are distorted by the rotation. The waves propagate along the tangents to the field lines, enter a region between the closed and open field lines, and leave the magnetosphere [22].

The generated t and lt waves affect the resonant particles and transfer some of the energy to them. The wave field changes the particle distribution function. In particular, the beam and tail particles acquire nonzero pitch angles due to quasilinear diffusion. Since the motion of the particles is relativistic, synchrotron radiation is generated in the X-ray and gamma-ray [13, 14, 19, 23, 24]. The frequency of this radiation is

$$\nu \approx \nu_0\frac{\sqrt{1-\frac{v^2}{c^2}}}{1-\frac{v}{c}\cos\alpha}; \tag{9}$$

and its power is

$$p_\nu = p_{\nu_0}\frac{1}{1-\frac{v}{c}\cos\alpha}; \tag{10}$$

where ν_0 is the frequency and p_{ν_0} the power of the radiation in the rest frame of the particles ($v_\parallel = 0$), and α is the angle between the magnetic field in the region of wave generation and the line of sight to the observer. When $\alpha = 0$,

$$\nu \approx 2\gamma_r\nu_0, \qquad p_\nu \approx 2p_{\nu_0}\gamma_r^2. \tag{11}$$

3. MECHANISM FOR CHANGING THE FIELD-LINE CURVATURE

As was shown in [25–27], along with t and lt waves, transverse electromagnetic drift waves can be generated in the magnetosphere. These propagate almost perpendicular to the magnetic field ($\frac{k_\varphi}{k_x} \ll 1$). Using the smallness of the parameters $\gamma\frac{\omega}{\omega_B} \ll 1$ and $\frac{u_{dr}^2}{c^2} \ll 1$ and assuming $k_r = 0$, we can obtain the following dispersion relation for these waves:

$$\epsilon_{\varphi\varphi} = \frac{k_x^2 c^2}{\omega^2 - k_\varphi^2 c^2}, \tag{12}$$

where

$$\epsilon_{\varphi\varphi} = 1 + \sum_i \frac{\omega_{p_i}^2}{\omega}\int \frac{v_\varphi/c}{\omega - k_\varphi v_\varphi - k_x u_{x_i}}\frac{\partial f}{\partial\gamma}d\left(\frac{p_\varphi}{mc}\right) \tag{13}$$

is the longitudinal–longitudinal component of the dielectric permittivity and $\omega_{p_i}^2 = \frac{4\pi n_p e^2}{m_i}$. The summation over i in (13) is carried out over the kinds of particles (electrons and positrons of the secondary plasma and electrons of the beam).

Let us assume that

$$\omega = k_x u_x^b + k_\varphi v_\varphi + a. \tag{14}$$

Here, u_x^b is the beam drift velocity, which can be fairly large for large γ_b. Partial integration of $\epsilon_{\varphi\varphi}$ and summation over i taking into account (14) results in the expression [25]

$$1 - \frac{3}{2\gamma_p^3}\frac{\omega_p^2}{\omega^2} - \frac{1}{2}\frac{\omega_p^2}{\omega^3}\frac{k_x u_x^p}{\gamma_p} - \frac{\omega_b^2}{\omega a}\frac{1}{\gamma_b^3} - \frac{\omega_b^2}{\omega a}\frac{k_x u_x^b}{\gamma_b} = \frac{k_\perp^2 c^2}{\omega^2}. \tag{15}$$

It can easily be shown that the third and fourth terms on the left-hand side of (15) are small. When $\frac{u_x^b}{c} \gg \frac{k_\varphi}{k_x}$, it follows from (14) that

$$\omega_0 \equiv \mathrm{Re}\omega = k_x u_x^b; \tag{16}$$

and, when $k_x^2 \ll \frac{\omega_p^2}{c^2\gamma_p^3}$, the increment will be

$$\Gamma = \mathrm{Im}\omega = \mathrm{Im}a \approx \left(\frac{n_b}{n_p}\right)^{1/2}\frac{\gamma_p^{3/2}}{\gamma_b^{1/2}}k_x u_x^b. \tag{17}$$

This increment is quite small: when $\gamma_b \sim 10^6$ and $\gamma_p \sim 10$, we obtain $\Gamma \sim 10^{-4}\omega_0$. However, since the wave is almost perpendicular to the magnetic field, it propagates around the magnetosphere and is located in the generation region for a long time. As a result, the amplitude of the drift waves can increase to large values [25] via the kinetic energy of the particles moving along the magnetic field with velocity v_φ. These particles cross the generation region in a short time ($< 10^{-2}$ s), but other particles enter the region, while the wave remains in nearly the same place. Its amplitude increases until nonlinear processes (in particular, induced scattering by the particles) begin to transfer wave energy to the region with the minimum wavenumber k (i.e., the maximum wavelength $\lambda_{\max}$). The value of $\lambda_{\max}$ depends on the transverse size of the magnetosphere, which can be identified with the radius of the light cylinder $r_{LC} = \frac{cP}{2\pi}$.

The electric vector of the low-frequency drift wave propagating across the magnetic field is directed along the magnetic field of the pulsar $E(E_\varphi, 0, 0)$, while its magnetic-field vector is directed along the r axis, $\mathbf{B}(0, 0, B_r)$. As follows from Maxwell's equation,

$$B_r = E_\varphi\frac{kc}{\omega}. \tag{18}$$

Since $\frac{kc}{\omega} \approx \frac{kc}{k_x u_x} \gg 1$, $B_r \gg E_\varphi$. The appearance of a B_r component results in bending of the field line. In a Cartesian coordinate system,

$$\frac{dy}{dx} = \frac{B_y}{B_x}, \tag{19}$$

and the curvature of the field line is determined by the expression

$$K = \frac{1}{\rho} = \left[1 + \left(\frac{dy}{dx}\right)^2\right]^{-3/2}\frac{d^2y}{dx^2}. \tag{20}$$

Using the equation $div\mathbf{B} = 0$ and the condition $k_r = 0$ in cylindrical coordinates, this curvature can be rewritten

$$K = \frac{B_{0\varphi}}{B}\frac{1}{r} - \frac{B_{0\varphi}^2}{B^2}\frac{1}{r}\frac{1}{B}\frac{\partial B}{\partial\varphi}. \tag{21}$$

Substituting $B = (B_{0\varphi}^2 + B_r^2)^{1/2} \simeq B_{0\varphi}(1 + \frac{B_r^2}{2B_{0\varphi}^2})$, we can derive from (21) the relation

$$K = \frac{1}{r}\left(1 - \frac{k_\varphi r B_r}{B_{0\varphi}}\right). \tag{22}$$

Consequently, the distortion of the field line can be substantial when $k_\varphi r \gg 1$. Since radiation is emitted tangent to the local magnetic-field line, changes in the curvature of this line result in changes in the direction of the radiation.

Let us consider the case when the angle β between the rotational axis of the neutron star and its magnetic moment is so small that radiation directed along the line of sight is always observed. If the field lines are bent, there is additional radiation, which initially

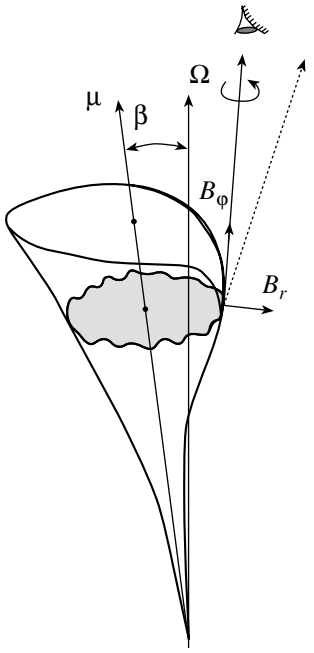

Fig. 3. Schematic of the model.

passed beyond the line of sight (the dashed line in Fig. 3) but now arrives at the observer (solid line). This additional radiation is pulsed with the period $2\pi/\omega_{\rm dr}$, and can explain the peculiarities observed in the radiation of magnetars (Fig. 3).

Note that thermal emission by the neutron-star surface or polar cap can also contribute to the persistent component of the radiation. The main part of the radiation depends strongly on the region in which it is generated. If this region is located in the most distant part of the magnetosphere (as is assumed in our model), an observer could see only this radiation, only radiation modulated by the drift waves, or a combination of the two. We shall consider below only radiation associated with the drift waves.

4. ESTIMATES OF THE MAGNETAR PARAMETERS

Let us first calculate the drift-wave period corresponding to the time interval between the observed pulses:

$$P_{dr} = \frac{2\pi}{\omega_{dr}} = \frac{2\pi}{k_x u_x^b} = \frac{\lambda}{u_x^b}. \qquad (23)$$

As was noted above, the maximum wavelength can be defined to be $\lambda_{\max} = \frac{cP}{2\pi}$. Then, assuming $\rho = \frac{cP}{2\pi}$ and taking into account (4) and (8), we find from (16) that

$$P_{\rm dr\,max} = \frac{e}{4\pi^2 mc}\frac{BP^2}{\gamma_b}. \qquad (24)$$

If we assume that $\gamma_b = 10^6$, then $P_{dr_{\max}} = 10$ s if

$$BP^2 = 22.45\ {\rm Gs}^2. \qquad (25)$$

If the magnetic field on the neutron-star surface is $B_s \sim 10^{12}$ G, then, assuming a dipole field structure, $B_s \sim 10^3$ G at the distance $\sim 10^3 R_*$. As follows from (25), the period of rotation of such a star should be $P = 0.15$ s. Consequently, even if the surface magnetic field is "normal," the formation of drift waves near the light cylinder and distortion of the magnetic-field lines in this region can explain the observed periods of magnetars, ~ 10 s. As follows from (24) with $P \sim 1$ s and $B_s \sim 10^{12}$ G, $P_{\rm dr}$ turns out to be comparable with the rotational period P. In this case, we can observe a subpulse drift, as is described in detail in [25].

The estimates in (24) were done for the maximum period. The spectral energy carried by drift waves with smaller periods will be substantially less than in the mode with period $P_{dr_{\max}}$.

Expression (24) enables us to find a relation between the observed period derivative $\dot{P}_{\rm dr}$ and the actual rate of deceleration of the neutron star's rotation $\dot{P}$:

$$\dot{P}_{\rm dr} = \frac{eB}{2\pi^2 mc\gamma_b} P\dot{P}. \qquad (26)$$

For the parameter values indicated above,

$$\dot{P} = 7.48 \times 10^{-3}\dot{P}_{\rm dr}. \qquad (27)$$

Therefore, when $\dot{P}_{\rm dr} \sim 10^{-10}$, we obtain $\dot{P} = 7.48 \times 10^{-13}$, close to the values measured in several young radio pulsars, such as the Crab and Vela pulsars (PSRB0531+21 and PSRB0833−45).

Let us now estimate the rate of loss of the neutron star's rotational energy:

$$\dot{E} = \frac{4\pi^2 \dot{P} I}{P^3}. \qquad (28)$$

The calculated values of P and $\dot{P}$ for $I = 10^{45}$ g cm^2 lead to the value $\dot{E} \sim 10^{37}$ erg/s, which is sufficient to explain the X-ray luminosities of magnetars L_x (see the table). In addition, we emphasize that this luminosity was derived assuming isotropic radiation, so that the actual values of L_x should be lower in the case of directed radiation.

5. COMPARISON OF THE PROPOSED MODEL WITH OTHER MAGNETAR MODELS

The most popular model currently used to describe the observed features of AXPs and SGRs is the magnetar model, i.e., a single neutron star with an internal magnetic field $\sim 10^{14}$–10^{15} G. The basic source of energy for the emission is supposed to

be associated precisely with this magnetic field [28]. We consider the mechanism for the transformation of the magnetic energy to radiation to be unclear. In particular, as was already noted, it is difficult to explain the cascade formation of an electron–positron plasma (which is a main component of all models for radio emission by neutron stars) at these field values. Consequently, it is not clear whether AXPs and SGRs should emit in the radio; however, the detection of 111 MHz radio emission from SGR1900+14 [10] and AXP1E2259+58 [11] has already forced revision of the limits on the radio emission possible in models with strong magnetic fields [5, 7], at least at low frequencies [29]. In addition, the problem of the prolonged existence of magnetic fields with strengths $\sim 10^{15}$ G remains unsolved. Some obstacles of the magnetar model were discussed in [30]. In particular, it is difficult to explain the observed jumps of $\dot{P}$. For example, $\dot{P}$ in SGR1900+14 increased from 6×10^{-11} to 1.3×10^{-10} during the flare of August 27, 1998 [31, 34]. Similar jumps of $\dot{P}$ have been observed in AXP1E1048.1–5937 and 1E2259+58. How can we explain the huge implied change in the magnetic field in such very short time? Moreover, when magnetic energy is lost and the magnetic field decreases, the rate of deceleration of the rotation should be less, whereas the observations revealed an increase in this quantity.

We shall discuss here in more detail only an estimate of the efficiency of the energy reservoir associated with such fields. The total energy of this reservoir is

$$E = \frac{B^2}{8\pi}\frac{4}{3}\pi R_*^3 = 1.7 \times 10^{45} - 1.7 \times 10^{47} \text{ erg}. \quad (29)$$

The X-ray luminosity of SGR1806–20 at 2–10 keV is $L_x \approx 2 \times 10^{35}$ erg/s [33]. Such luminosities can be produced for a period $\sim 10^4$ yr by the reservoir of magnetic energy $\sim 10^{47}$ erg available in the neutron star. If we assume that the ages of ordinary radio pulsars are $\sim 10^7$ yr, then we should see only one magnetar per thousand radio pulsars. This estimate is an order of magnitude less than the number of AXPs and SGRs detected thus far. The energetic problems become even greater if we take into account the fact that SGR1806–20 feeds relativistic particles to the surrounding supernova remnant, with the power of this process being $L_p \sim 10^{37}$ erg/s [33]. As a result, the energetic reservoir of the magnetar should be exhausted within 360 yr. At the same time, as was noted above, the age of this object is estimated to be 1400 yr. Since some magnetars are not associated with observed supernova remnants, their ages appear to be well above 10^4 yr. If this conclusion is correct, the energetic problems of the magnetar model become even more difficult. As a result, still higher magnetic fields ($\sim 10^{16}$ G) must be postulated [30]. We emphasize that the estimate $\dot{E} \sim 10^{37}$ erg/s for a typical magnetar, obtained in Section 4, can also produce the above supply of relativistic particles.

The accretion of surrounding plasma onto the neutron star represents an alternative explanation for the observed features of AXPs and SGRs [12]. This accretion provides an extra source of energy (at fields $\sim 10^{12}$ G), so that it is not necessary to suppose the existence of superstrong magnetic fields. Moreover, this model provides a mechanism for decreasing the angular momentum, so that large values of $\dot{P}$ can be explained without introducing magneto-dipole deceleration. In this case, the so-called breaking index characterizing the deceleration must be different from $n = 3$, characteristic of the magneto-dipole mechanism (see, for example, [34]). Observations of SGR1900+14 give $n = 0.19 \pm 0.48$ [10]. Unfortunately, the accretion model encounters a number of its own difficulties. Accretion associated with the interstellar medium is able to produce luminosities $L \sim 10^{32}$ erg/s [1], considerably lower than the observed X-ray luminosities L_x of AXPs and SGRs (see the table). In addition, if the accretion occurs from a relic disk, its age turns out to be very small (less than one year), and the accretion cannot bring about the observed deceleration of AXPs on its own [35]. The plasma associated with a second component in a system is able to explain the observed luminosities at moderate accretion rates ($\sim 10^{-11} M_\odot$/yr) [1], but no AXP or SGR has been detected as a member of a binary system. Since matter is always present around a neutron star, accretion processes should play some role in its evolution; however, as is shown above, the accretion models encounter considerable problems when invoked as the main mechanism to explain the observed features of magnetars.

It was proposed in [30] to consider the gravitational collapse of a pulsar into a strange or quark star. The energy released during such a collapse turns out to be sufficient to explain short gamma-ray bursts, the peculiar form of the supernova remnants around SGRs and AXPs, and the extremely large velocities of these objects. Here, we will not discuss the nature of gamma-ray bursts, and consider only the "quiescent" radiation of AXPs and SGRs. In our view, some additional effects must be taken into account in any model to explain the bursts. For example, along with the secondary collapse of a neutron star [30], the emission by the quark surface of a strange star heated by collisions with massive cometary-like bodies has been used to describe the huge bursts observed in SGR0526–66 and SGR1900+14 [36]. Discussion of such models is beyond the scope of the present paper.

It is unnecessary in our model to assume the existence of superstrong magnetic fields inside the neutron star, a high-density surrounding medium, or exotic strange and quark stars. The observed parameters of AXPs and SGRs can be interpreted in the framework of usual concepts of pulsar magnetospheres.

6. CONCLUSIONS

(1) We have investigated explanations of the observed features of AXPs and SGRs that do not require the assumption of superstrong magnetic fields in neutron stars or accretion from a surrounding medium onto the neutron stars.

(2) Drift waves can exist in outer parts of the magnetosphere, whose periods are in the range of the observed periods of AXPs and SGRs. An amplitude of the magnetic field on the neutron-star surface of $\sim 10^{12}$ G proves to be sufficient. The period of the rotation should be ~ 0.1 s, with $\dot{P} \sim 10^{-13}$.

(3) The rate of loss of rotational energy ($\sim 10^{37}$ erg/s) is sufficient to produce the X-ray luminosities of AXPs and SGRs, as well as to feed relativistic particles to the supernova remnants associated with these objects.

(4) Our model allows radio emission by AXPs and SGRs, which can be formed near the source of X-ray emission. For example, the peculiar features of the radio pulsar J2144-3983 with a period of 8.5 s [37] can be explained using our model. The observed period is the "fictitious" (drift) period $P_{\rm dr}$, while the period of rotation of the neutron star is $P \ll P_{\rm dr}$. The pulses are also formed by the drift processes described in this paper, and their width is not directly related to the angle of the cone of open field lines or to the small angle β.

(5) A good confirmation of the proposed model would be the detection of modulation with a period equal to the rotational period of the pulsar ($P \sim 0.1$ s) in the persistent components of AXPs and SGRs. The presence of such a persistent pedestal is explained in a natural way when $\beta < 10^\circ$.

(6) The smallness of the angle β ($< 10^\circ$) in our model can explain the small number of objects (~ 10) with long periods (> 5 s). From a statistical point of view, only $\sim 1\%$ of the ~ 1000 pulsars discovered until the present can satisfy the conditions of applicability of our model, ($\beta < 10$ and $P < 0.1$ s).

(7) Only specific features of the "quiescent" radiation from AXPs and SGRs were considered here. The origin of the gamma-ray bursts remains unclear. The presence of additional sources of energy must be postulated to explain the generation of these bursts. They may be associated with a short-term release of energy through cracks in the core of the neutron star, as is described by Thompson and Duncan [28].

ACKNOWLEDGMENTS

This work was supported by the Russian Foundation for Basic Research (project no. 00-02-17850) and by grants from the National Science Foundation (NSF-00-098685) and INTAS (INTAS-00-849). One of the authors (GZM) was supported by the Georgian Foundation for Basic Research. We are grateful to L.B. Potapova for preparation of the manuscript.

REFERENCES

1. S. Mereghetti, astro-ph/9911252.
2. K. Hurley, AIP Conf. Proc. **526**, 763 (2000).
3. R. C. Duncan and C. Thompson, Astrophys. J. **392**, L9 (1992).
4. S. Mereghetti, in *Frontier Objects in Astrophysics and Particle Physics*, Ed. by F. Giovannelli and G. Mannocchi (Italian Physical Society, 2001), p. 239.
5. M. G. Baring and A. K. Harding, Astrophys. J. **547**, 929 (2001).
6. V. Hambarian, G. Hasinger, A. D. Schwope, and N. S. Schulz, Astron. Astrophys. **381**, 98 (2002).
7. M. G. Baring and A. K. Harding, Astrophys. J. **507**, L55 (1998).
8. I. F. Malov, Astron. Zh. **78**, 452 (2001) [Astron. Rep. **45**, 389 (2001)].
9. M. G. Baring and A. K. Harding, astro-ph/9711211.
10. Yu. P. Shitov, V. D. Pugachev, and S. M. Kutuzov, in *IAU Colloq. 177: Pulsar Astronomy—2000 and Beyond*, Ed. by M. Kramer, N. Wex, and N. Wielebinski, Astron. Soc. Pac. Conf. Ser. **202**, 685 (2000).
11. V. M. Malofeev and O. I. Malov, astro-ph/010643531.
12. D. Marsden, R. E. Lingenfelter, R. E. Rotschild, and J. C. Higdon, Astrophys. J. **550**, 397 (2001).
13. G. Z. Machabeli and V. V. Usov, Pis'ma Astron. Zh. **5**, 445 (1979) [Sov. Astron. Lett. **5**, 238 (1979)].
14. D. G. Lominadze, G. Z. Machabeli, and A. B. Mihailovskii, Fiz. Plazmy **5**, 1337 (1979).
15. A. Z. Kazbegi, G. Z. Machabeli, G. I. Melikidze, and V. V. Usov, *Joint Varenna-Abastumani International School and Workshop on Plasma Astrophysics ESA, Paris* (1989), Vol. 1, p. 271.
16. A. Z. Kazbegi, G. Z. Machabeli, and G. I. Melikidze, *IAU Colloq. 128: Magnetospheric Structure and Emission Mechanics of Radio Pulsars*, Ed. by T. H. Hankins, J. M. Rankin, and J. A. Gil (Pedagogical Univ. Press, 1992), p. 232.
17. M. Lyutikov, G. Z. Machabeli, and R. Blandford, Astrophys. J. **512**, 804 (1999).
18. M. Lyutikov, R. Blandford, and G. Z. Machabeli, Mon. Not. R. Astron. Soc. **305**, 358 (1999).
19. I. F. Malov and G. Z. Machabeli, Astrophys. J. **554**, 587 (2001).
20. A. S. Volokitin, V. V. Krasnosel'skikh, and G. Z. Machabeli, Fiz. Plazmy **11**, 310 (1985).
21. J. Arons and J. J. Barnard, Astrophys. J. **302**, 120 (1986).

22. A. Z. Kazbegi, G. Z. Machabeli, G. I. Melikidze, and C. Shukree, Astron. Astrophys. **309**, 515 (1996).
23. G. Z. Machabeli, Q. Luo, D. Melrose, and S. Vladimirov, Mon. Not. R. Astron. Soc. **312**, 51 (2000).
24. G. Z. Machabeli, Q. Luo, S. Vladimirov, and D. Melrose, Phys. Rev. E **65**, 036408 (2002).
25. A. Z. Kazbegi, G. Z. Machabeli, and G. I. Melikidze, Aust. J. Phys. **44**, 573 (1987).
26. O. Chedia, J. Lominadze, G. Machabeli, *et al.*, Astrophys. J. **479**, 313 (1997).
27. G. Z. Machabeli, D. Khechinashvili, G. I. Melikidze, and D. Shaparidze, Mon. Not. R. Astron. Soc. **327**, 984 (2001).
28. C. Thompson and R. C. Duncan, Astrophys. J. **473**, 322 (1996).
29. B. Zhang, Astrophys. J. **562**, L59 (2001).
30. A. Dar and A. De Rujula, astro-ph/0002014.
31. P. M. Wood, P. M. Wools, C. Kouveliotou, *et al.*, Astrophys. J. **524**, L55 (1999).
32. D. Marsden, R. E. Rothschild, and R. E. Lingefelter, Astrophys. J. **520**, L107 (1999).
33. C. Kouveliotou, S. Dieters, T. Strohmayer, *et al.*, Nature **393**, 235 (1998).
34. I. F. Malov, Astron. Zh. (in press).
35. X.-D. Li, Astrophys. J. **520**, 271 (1999).
36. V. V. Usov, Phys. Rev. Lett. **87**, 021101 (2001).
37. M. D. Young, R. N. Manchester, and S. Johnston, Nature **400**, 848 (1999).

Translated by Yu. Dumin

Astronomy Reports, Vol. 47, No. 3, 2003, pp. 240–247. Translated from Astronomicheskiĭ Zhurnal, Vol. 80, No. 3, 2003, pp. 266–273.

On the Atomic Constants of ReI

Yu. M. Smirnov

Moscow Power Engineering Institute, ul. Krasnokazarmennaya 17, Moscow, 111250 Russia

Received September 24, 2002; in final form, October 10, 2002

Abstract—We have experimentally studied the excitation of the rhenium atom by collisions with slow monoenergetic electrons and measured 47 excitational cross sections for lines of ReI at an electron energy of 50 eV. Previously published information about the probabilities of radiative transitions of ReI is analyzed. The data for two experimental studies of the ratios $I\lambda/gA$ for transitions with a common upper level differ by three orders of magnitude. © *2003 MAIK "Nauka/Interperiodica".*

1. INTRODUCTION

The atomic constants of heavy metals with high melting temperatures are studied quite seldom. The main problem in theoretical investigations of these substances is the absence of sufficiently detailed information on the structure of terms, classification of energy levels, and transitions. Even the low energy levels are often not classified or are classified based on their LS coupling, which is obviously inadequate for descriptions of complex electron shells. The main difficulty with experimental studies has been the need to heat the substances to high temperatures (required for their evaporation) and has not been overcome until recently. This obstacle can be partially removed by using electrical discharges of various kinds: atoms and ions of high-melting metals are formed in an arc discharge, hollow-cathode discharge, and so on.

The use of electrical discharges enables one to successfully study the radiative characteristics of atoms and ions, such as their transition probabilities, oscillator strengths, radiative lifetimes, and branching ratios. On the other hand, it is very difficult to obtain reliable information on collisional characteristics—the cross sections for excitation, ionization, and so on—from gas-discharge experiments. A substantially more reliable and informative approach to studying collisional cross sections is the crossing-beam method, which makes it possible to spatially separate the preparation of the object (i.e., an atomic or ionic beam) from the interaction between the colliding particles.

Unfortunately, there are many technical difficulties in the implementation of the crossing-beam method for elements whose evaporation temperatures exceed 2000 K. As a result, experiments with such elements have not been carried out. Gadolinium possessed the highest evaporation temperature among elements studied earlier, 1900 K [1]. As was emphasized by Shimon *et al.* [1], studies of the electron-impact excitation of free gadolinium atoms require overcoming considerable experimental difficulties. On the other hand, when [1] was published, we had already proposed the extended crossing-beam method and constructed an installation [2] that enabled us to study electron–atom collisions for any atoms of any element, without restrictions on their evaporation temperature. This method was used to study inelastic collisions of electrons with atoms of boron (2400 K) [3], hafnium (2700 K) [4], and niobium (2900 K) [5]. (The evaporation temperatures of the elements are given in parentheses.)

The aim of the present work is an experimental investigation of the excitation of rhenium atoms colliding with slow monoenergetic electrons. Since temperatures exceeding 3000 K are necessary to evaporate rhenium, there is currently no alternative to using the extended crossing-beam method.

Rhenium belongs to the VIIB group of elements, along with manganese and promethium. The experimental study of manganese and determination of its atomic constants are not difficult. In contrast, prospects for studying the characteristics of promethium under laboratory conditions are slim, at least in the nearest future. One way to obtain information about the atomic constants of promethium may be to perform an interpolation of the corresponding characteristics of manganese and rhenium.

About 6000 spectral lines in the optical spectrum of rhenium are currently known [6]. About 4200 of these have been attributed to the spectrum of ReI, but only one third of these lines were classified [7]. Moreover, the available classification does not provide full information on the energy levels of ReI, since only the energy, parity, and inner quantum number J have been found for most of the levels. Other quantum numbers and configurations were determined only in a few cases (usually for low energy levels).

1063-7729/03/4703-0240$24.00

Analysis of the system of terms of ReI was carried out in [7] on the basis of LS coupling, which is obviously inadequate for an atom with a complex electron shell, such as rhenium. A theoretical treatment of the low energy levels of rhenium was later presented in [8] using a generalized parametric analysis. The even levels related to the $5d^56s^2 + 5d^66s + 5d^7$ configurations were treated taking into account configuration mixing. It was found that mixing effects play an important role for these levels. As a result, the classifications of many even levels (primarily those located above 20 000 cm^{-1}) were considerably modified compared to those of [7].

The atomic constants of ReI have been studied in a number of experimental works. A classification of eight odd sextet levels of the $5d^46s^26p$ configuration was considered in [9] taking into account the isotopic shift, and the A and B constants for these levels were determined. Over 800 experimental values of transition probabilities in ReI were obtained in the well-known monograph [10], and the radiative lifetimes of nine energy levels of rhenium and the oscillator strengths for five rhenium lines were measured in [11]. On the other hand, the collisional constants of ReI have not been studied either experimentally or theoretically.

2. EXPERIMENT

Our rhenium experiment is based on the extended crossing-beam method, which has been used recently to study the excitation of tantalum atoms [12]. The atomic beam was produced by evaporating a TU 48-19-92-74 rhenium sample with a total impurity abundance of 0.005% from an autocrucible (the concentrations of the main impurities Fe, Si, and K were 0.001% each). Seven short strips of rhenium ($6 \times 6 \times 25$ mm) were put in a pile, and the beam of an electron gun focused at its center. The pile of strips was mounted on a graphite substrate, responsible for thermal decoupling between the metal and experimental setup. A relatively small portion of the metal (a spot with a diameter of about 12 mm) was melted. The melt zone did not come in contact with the graphite substrate or any other element of the setup, enabling us to avoid contamination of the atomic beam.

In the basic evaporation regime, the temperature of the melt surface reached 3600 K, and the concentration of atoms in the beam was 1.4×10^9 cm^{-3}. Reabsorption in resonant lines of ReI was small at such concentrations, despite the considerable length of the atomic beam (200 mm) along the line of sight of the optical system. The small amount of reabsorption was due to the fan-shaped divergence of the atomic beam [13], so that spectral lines emitted by the atoms in one small volume element of the beam were not absorbed by atoms in other, spatially separated, volume elements due to the Doppler effect. In addition, the transition probabilities for the resonant lines of atomic rhenium are not very large [10].

The distribution of atoms over low levels in the atomic beam before the collisions with the electrons is an important factor that must be taken into account when comparing the experimental and theoretical cross sections. Low levels can be populated by thermal excitation during the evaporation of the atoms. Fortunately, the intervals between the ground level of the rhenium atom $5d^56s^2\ a^6S_{5/2}$ and the lowest excited levels are fairly large. The lowest even excited levels of ReI are $5d^56s^2\ a^4P_{5/2}$ (11 586.96 cm^{-1}) and $5d^6(^5D)6s\ a^6D_{9/2}$ (11 754.52 cm^{-1}). Estimates based on a Boltzmann distribution give populations of these levels of 1.00% and 1.57% of the population of the ground level. Due to the inverse order of the levels in both these terms, the populations of other levels of these terms ($a^4P_{3/2,1/2}$ and $a^6D_{7/2,5/2,3/2,1/2}$) decrease sharply, since their statistical weights decrease with increasing energy. The $5d^56s(a^7S)6p\ z^8P^\circ_{5/2}$ octet (18 950.1 cm^{-1}) is the lowest odd level of ReI, and its population is only 0.054% of the ground-level population. Therefore, the effect of thermal excitation of the rhenium can be neglected, and the initial level can be taken to be purely the ground level when considering the electron-impact excitation.

As was noted in [12], the bright background radiation with a continuous spectrum emitted by the surface of the melted metal leads to considerable difficulties in studies of the excitation of elements with high melting points, and appreciably limits the spectral range accessible to investigation from the long-wavelength side. When the power of the radiation by the molten surface is of the order of a few kW, no diaphragm can completely exclude the arrival of scattered radiation to a photodetector, especially when using extended beams. The boundary of the range accessible to study in the case of rhenium was at 351 nm. Along with this background radiation, the structure of the spectrum of the object studied also affects the position of this boundary.

An electron beam with a specified energy was produced by a low-voltage electron gun with an indirect-heating flat cathode coated with an oxide emitting layer. The current density of the beam in the rhenium experiment was below 0.9 mA/cm^2 in the entire operational energy range of 0–250 eV. The width of the electron-energy distribution was no greater than 1.0 eV for electron energies of 20–200 eV (for 90% of the electrons in the beam). The beam current in electron guns usually decreases considerably at low

energies ($E < 15$–20 eV) due to the effect of the negative volume charge, but we took special measures against this, described in detail in [14]. Their efficiency was quite high: the electron-beam current (and corresponding optical signal) increased by one to two orders of magnitude at $E < 10$ eV, and the potential relief of the space in which the electrons move was substantially smoothed.

Although all our measurements were carried out in the ultraviolet, the optical system did not require special adjustment due to its achromatism. Apart from the output quartz window of the vacuum chamber, all other elements of the optical system (mirrors, diffraction grating) are reflective. The effective spectral resolution, which is determined both by the characteristics of the optical system and by the ratio of the operational speed of the detectors and the rate at which the spectrum is scanned, was approximately 0.1 nm. The extended crossing-beam technique and the experimental procedures used are discussed in more detail in [2, 13–15].

3. RESULTS AND DISCUSSION

We studied the excitation of spectral lines of atomic rhenium by a beam of monoenergetic electrons with an energy of 50 eV at 209–351 nm. The results related to resonant lines of ReI are discussed in [16]. The results concerning the excitation of nonresonant transitions are given in the present paper.

The experimental data supplemented by spectroscopic information on the transitions under investigation are compiled in the Table. The wavelength λ, transition, inner quantum number J, energies of the lower $E_{\rm low}$ and upper $E_{\rm up}$ levels, and excitational cross section for an electron energy of 50 eV, Q_{50}, are given. The values in the last column are explained and discussed in the next section.

We can see in the Table that all the low levels of the transitions studied are even, while all the upper levels are odd. This seems quite natural since, as was noted in the previous section, the excitation of atomic rhenium occurs only from the even ground level $5d^5 6s^2\ a^6S_{5/2}$. Although a combination of states with the same parity is not strictly forbidden during electron-impact excitation, the probability of such processes is usually considerably less than the probability for transitions between pairs of states with different parities.

The wavelengths, transitions, J values, and level energies in the Table are primarily given in accordance with [7]. Although, as was noted in the Introduction, the classification of ReI transitions of [7] was substantially modified in [8], the notation of [7] is more compact and convenient. In addition, there is little sense in insisting on a rigorous designation for even, low levels given the current state of analysis of the higher odd levels, transitions from which we have not studied. The Table shows that configurations and terms have been established only for six of the 52 presented transitions. Moreover, two of these correspond to resonant transitions that could not be separated from nonresonant transitions from higher levels.

The measured cross sections are in the range 8×10^{-18}–1.7×10^{-16} cm^2. As is mentioned above, the forbidden nature of spontaneous radiative transitions between certain pairs of levels in the dipole approximation does not apply rigorously to the case of electron-impact excitation. Nevertheless, to first approximation, the probabilities of the collisional transitions observe the quantum selection rules. We can see in the Table that, among the levels studied here, the odd levels with $J = 7/2$ are excited most frequently (17 cases). This behavior follows the $\Delta J = +1$ selection rule for excitation from the ground level $5d^5 6s^2\ a^6S_{5/2}$ quite naturally. Transitions from levels with $J = 5/2$, for which $\Delta J = 0$, and with $J = 9/2$, for which $\Delta J = +2$, are slightly less frequent (13 and 10 cases, respectively). These are followed by transitions from levels with $J = 3/2$ ($\Delta J = -1$, 4 cases) and $J = 11/2$ ($\Delta J = +3$, 5 cases). The level with $J = 1/2$ ($\Delta J = -2$) appears only once, and no excitation of levels with $J = 13/2$ was detected. Therefore, we obtain an almost symmetric bell-shaped distribution with its maximum approximately at $J = 7/2$.

The quantities measured in experiments based on excitation with the subsequent detection of optical emission by the excited atoms are the excitational cross sections of the spectral lines Q_{ki}. On the other hand, the basic quantity of theoretical interest is the excitational cross section of the energy level q_k (as in other problems of plasma kinetics). The relationship between these quantities is given by the balance equation

$$q_k = \sum_i Q_{ki} - \sum_l Q_{lk}. \qquad (1)$$

The left-hand sum represents the total excitational cross section of energy level k, including both the contribution from direct excitation of this level from the initial state by electron collisions and the contribution from cascade population of the level k by spontaneous radiative transitions from higher levels l. The latter contribution is represented by the right-hand sum.

In general, the terms of both sums can be determined in experiments on atomic electron-impact excitation without any supplementary information. Unfortunately, the accuracy of the results depends substantially on the completeness and uniformity of the

Excitational cross sections of the rhenium atom

λ, nm	Transition	J	E_{low}, cm^{-1}	E_{up}, cm^{-1}	Q_{50}, 10^{-18} cm^2	$I\lambda/gA$
211.387	$5d^56s^2a^4G-$	7/2–7/2	15 058	62 350	95.0	–
216.310	$5d^56s^2a^4G-$	5/2–5/2	14 621	60 837	35.4	–
218.372	$5d^56s^2a^4G-$	7/2–5/2	15 058	60 837	169.	–
223.860	$5d^66sa^6D-$	9/2–9/2	11 754	56 411	105.	–
231.297	$5d^56s^2a^4G-$	7/2–9/2	15 058	58 279	91.5	0.825
234.528	$5d^56s^2a^4P-$	3/2–1/2	13 826	56 451	109.	2.23
235.207	$5d^56s^2a^4P-$	5/2–7/2	11 583	54 086	166.	2.70
240.506	$5d^66sa^6D-$	9/2–9/2	11 754	53 320	73.0	2.33
240.560	$5d^56s^2a^6S-5d^56s6py^6D^\circ$	5/2–3/2	0	41 557		43.7
241.940	$5d^66sa^6D-$	5/2–7/2	15 770	57 090	137.	2.20
241.981	$5d^56s^2a^6S-5d^56s6py^6D^\circ$	5/2–5/2	0	41 313		12.1
242.350	$5d^56s^2a^4G-$	7/2–9/2	15 058	56 307	69.8	3.30
244.494	$5d^56s^2a^4P-$	5/2–5/2	11 583	52 472	135.	2.09
244.698	$5d^56s^2a^4G-$	7/2–9/2	15 058	55 912	106.	0.245
245.089	$5d^56s^2a^4P-$	5/2–7/2	11 583	52 373	16.8	2.63
246.024	$5d^56s^2a^4P-$	5/2–5/2	11 583	52 218	67.3	1.76
246.120	$5d^66sa^6D-$	9/2–7/2	11 754	52 373	63.0	3.78
247.628	$5d^56s^2a^4P-$	5/2–7/2	11 583	51 955	8.6	5.40
248.082	$5d^66sa^6D-$	7/2–7/2	14 216	54 513	73.3	6.20
248.392	$5d^66sa^6D-$	9/2–9/2	11 754	52 001	47.0	1.27
248.733	$5d^66sa^6D-$	9/2–11/2	11 754	51 945	61.2	1.60
249.886	$5d^56s^2a^4P-$	5/2–5/2	11 583	51 590	33.7	1.52
255.651	$5d^66sa^6D-$	7/2–9/2	14 216	53 320	24.2	0.498
258.031	$5d^66sa^6D-$	5/2–7/2	15 770	54 513	32.6	0.411
260.794	$5d^56s^2a^4G-$	5/2–3/2	14 621	52 954	13.7	–
264.275	$5d^66sa^6D-$	9/2–9/2	11 754	49 582	35.6	2.37
266.363	$5d^66sa^6D-$	9/2–11/2	11 754	49 286	39.3	2.51
268.853	$5d^66sa^6D-$	5/2–3/2	15 770	52 954	30.2	2.80
269.025	$5d^56s^2a^4G-$	11/2–11/2	16 307	53 467	42.3	1.05
271.675	$5d^66sa^6D-$	3/2–3/2	16 327	53 125	31.9	1.36
273.221	$5d^56s^2a^4G-$	7/2–7/2	15 058	51 647	38.0	1.69
274.286	$5d^66sa^6D-$	5/2–5/2	15 770	52 218	32.4	–
275.285	$5d^56s^2a^4P-$	5/2–5/2	11 583	47 899	38.4	2.95
275.305	$5d^56s^2a^4G-$	5/2–5/2	14 621	50 934		1.88
276.329	$5d^66sa^6D-5d^66py^6F^\circ$	9/2–7/2	11 754	47 932	37.5	7.16
276.379	$5d^56s^2a^4G-$	7/2–7/2	15 058	51 229		1.57
278.143	$5d^66sa^6D-$	7/2–5/2	14 216	50 158	44.5	1.60
279.094	$5d^66sa^6D-$	5/2–5/2	15 770	51 590	54.4	1.58
284.300	$5d^66sa^6D-$	5/2–5/2	15 770	50 934	50.5	2.25
286.007	$5d^66sa^6D-$	7/2–9/2	14 216	49 170	33.2	4.08
286.553	$5d^56s^2a^4D-$	7/2–5/2	17 330	52 218	10.3	–
292.742	$5d^66sa^6D-$	9/2–11/2	11 754	45 904	33.2	1.23
294.909	$5d^56s^2a^4D-$	7/2–7/2	17 330	51 229	16.0	0.983
296.511	$5d^66sa^6D-5d^66py^6F^\circ$	7/2–7/2	14 216	47 932	82.0	1.69
296.576	$5d^66sa^6D-$	9/2–7/2	11 754	45 462		2.78
303.045	$5d^66sa^6D-$	7/2–9/2	14 216	47 205	26.3	1.26
304.100	$5d^56s^2a^4G-5d^66py^6F^\circ$	7/2–7/2	15 058	47 932	21.6	1.32
339.025	$5d^56s^2a^2G-$	9/2–7/2	22 160	51 647	31.5	1.02
342.851	$5d^56s^2a^2F-$	7/2–5/2	21 775	50 934	18.1	–
348.223	$5d^56s^2a^2G-$	9/2–7/2	22 160	50 869	27.6	1.26
349.086	$5d^66sa^6D-$	1/2–3/2	17 238	45 876	30.9	2.05
351.228	$5d^56s^2a^4G-5d^66py^6F^\circ$	9/2–11/2	16 619	45 082	29.7	5.85

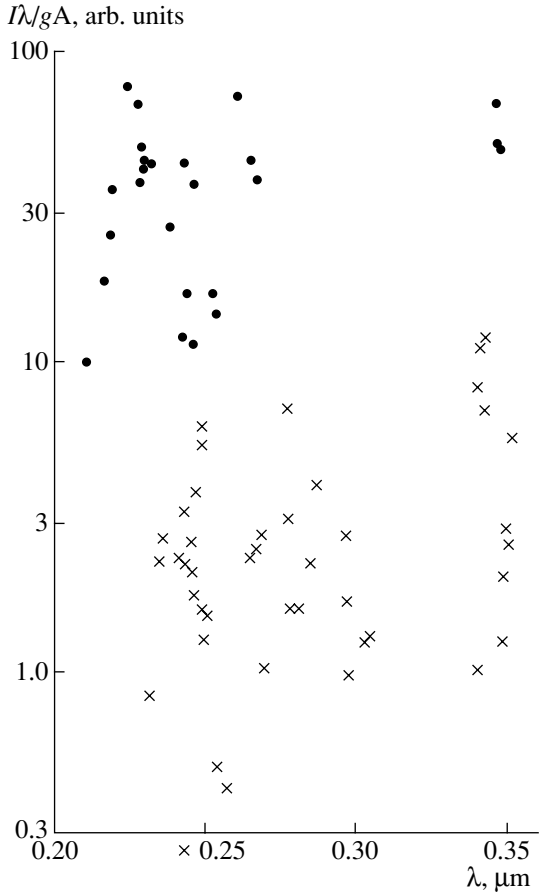

Fig. 1. Dependence of the ratio $I\lambda/gA$ on the wavelength for the data of [7, 10] for the transitions studied here and in [16]. The resonant transitions are marked by circles, and nonresonant transitions by crosses.

experimental data. There are two main limitations to the completeness of the information obtained in real experiments: (1) difficulties in detecting weak optical signals, which prevent the detection of many low-intensity transitions (primarily between high levels); and (2) difficulties in detecting optical signals within a rather broad spectral interval. The second factor is less important in the ultraviolet or vacuum ultraviolet, since the spectrum of any atom is obviously limited from the short-wavelength side by the ionization energy (if radiative transitions from autoionization states are not taken into account). In contrast, there is no such limitation in the infrared, and the comparatively intense transitions can occur with quite large probabilities. Note that the cross sections are proportional not to the intensity (or brightness) of the line on its own, but to the number of photons emitted per unit volume per unit time under the fixed excitation conditions. Since each infrared photon carries a small energy, the excitational cross sections for infrared transitions can be quite large, even when the line intensities are small. Therefore, most difficulties in using relation (1) occur in the determination of the contribution from the cascade population, since cascade transitions are substantially shifted toward the long-wavelength side compared to resonant transitions.

Both problems discussed above can be partially overcome by utilizing the fact that

$$Q_{ki}/Q_{km} = A_{ki}/A_{km}, \qquad (2)$$

where A_{ki} and A_{km} are the probabilities of transitions $k \to i$ and $k \to m$, respectively. Then, by directly measuring the excitational cross section Q_{ki} for transition $k \to i$, we can determine the excitational cross section of any other transition from level k:

$$Q_{km} = Q_{ki}\frac{A_{km}}{A_{ki}}. \qquad (3)$$

As was noted in the Introduction, various kinds of gas discharges can be efficiently used to study radiative transition probabilities. Since the amplitudes of the optical signals from gas-discharge sources are several orders of magnitude greater than the allowed (and actually achievable) signals from crossing beams, the transition probabilities can be investigated substantially more accurately and comprehensively than the excitational cross sections. In particular, the accessible spectral range can be extended toward the infrared, since the relatively low sensitivity of infrared detectors becomes a less restrictive factor when the intensity of the source radiation becomes sufficiently high. The optical spectra of atoms have been studied experimentally up to a wavelength of 100 μm (see, for example, compilation [17]). Unfortunately, the available information on the spectrum of atomic rhenium and the transition probabilities of ReI is far from complete.

4. THE TRANSITION PROBABILITIES OF ATOMIC RHENIUM

Before using (3) [and, consequently, (1)], we should analyze the completeness and accuracy of the available data on the transition probabilities of atomic rhenium. This analysis is appreciably limited by the fact that reasonably detailed data on the transition probabilities of ReI have only been obtained in the single work [10]. The technique and methods of [10] and the processing of the experimental data were considered in [12].

The following relation was used in [10] to calculate the transition probabilities using the experimental data:

$$gA_{\rm abs} = 0.667 \times 10^{16} \times C\frac{u}{np}I\lambda e^{E/kT}, \qquad (4)$$

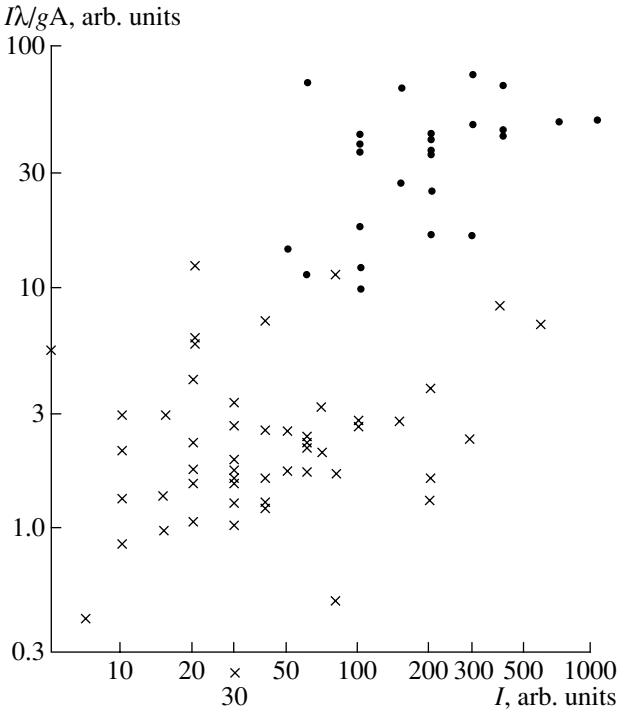

Fig. 2. Dependence of the ratio $I\lambda/gA$ on the line intensity for the data of [7, 10].

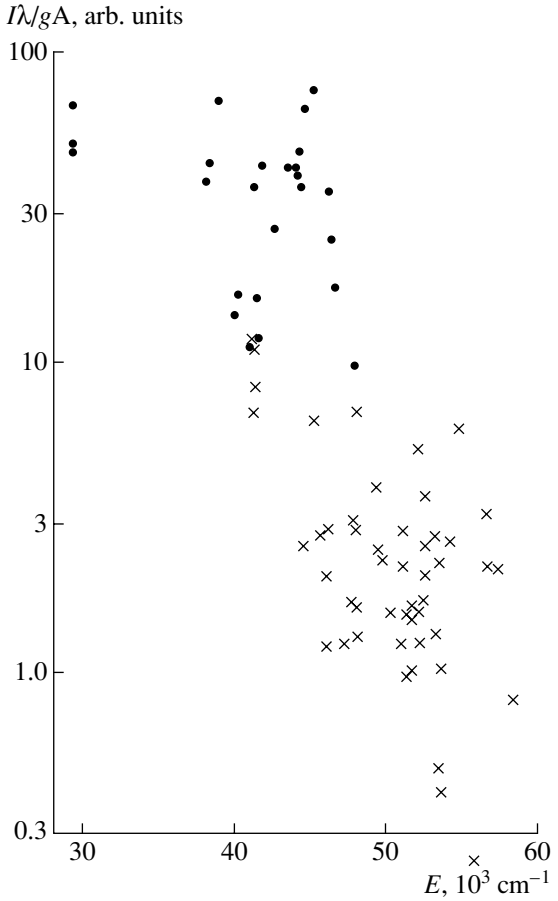

Fig. 3. Dependence of the ratio $I\lambda/gA$ on the energy of levels for the data of [7, 10].

where g is the statistical weight of the upper level, C is a normalization factor, u is the sum over states, p is the residence time of the atoms in the discharge region relative to the residence time of copper atoms, I is the intensity of the spectral line, E is the energy of the upper level, k is the Boltzmann constant, and T is the absolute temperature. Since $E = \text{const}$ for lines with a common upper level,

$$I\lambda/gA = \text{const} \sim e^{-E/kT}. \qquad (5)$$

To compare with the data of [10], it is reasonable to use the values of I and λ presented in [7], since this is the most recent work devoted to the spectrum of ReI, and includes a critical analysis of previous experimental studies of the spectrum of atomic rhenium. The ratios $I\lambda/gA$ for all the lines studied are shown in the last column of the Table. In addition, we used the corresponding information from [16] for the resonant and competing transitions of ReI.

The results of the comparison are presented in Figs. 1–3, which show the dependences of the ratio $I\lambda/gA$ on the wavelength and line intensity for the data of [7], as well as on the energy of the upper level. The resonant lines are marked by circles, and nonresonant lines by crosses. As follows from (5), the $I\lambda/gA = f(\lambda)$ and $I\lambda/gA = f(I)$ dependences should be sets of horizontal lines, each of which corresponds to a specific value of E, i.e., to a particular energy level. In the dependence $I\lambda/gA = f(E)$, each line should be reduced to a point.

Figure 1 shows that the $I\lambda/gA = f(\lambda)$ dependence covers the entire plot almost uniformly. At the same time, the resonant and nonresonant transitions are completely separated. A tendency for the separation of resonant and nonresonant transitions was found previously when considering the same dependence for atomic tantalum [12]. In the case of rhenium, we obtained a complete rather than partial separation.

The distribution of circles and crosses in Fig. 2 also covers nearly the entire plot, but some structure can be seen: in general, $I\lambda/gA$ increases with the line intensity. As in Fig. 1, there are no horizontal lines, whose presence is a natural consequence of relation (5). However, there is still a separation of resonant and nonresonant transitions. The most probable origin of this behavior is the presence of strong reabsorption of resonant lines in [10], as in the case of the tantalum atom.

The distribution in Fig. 3 becomes more compact. However, there is no degeneracy to a set of points,

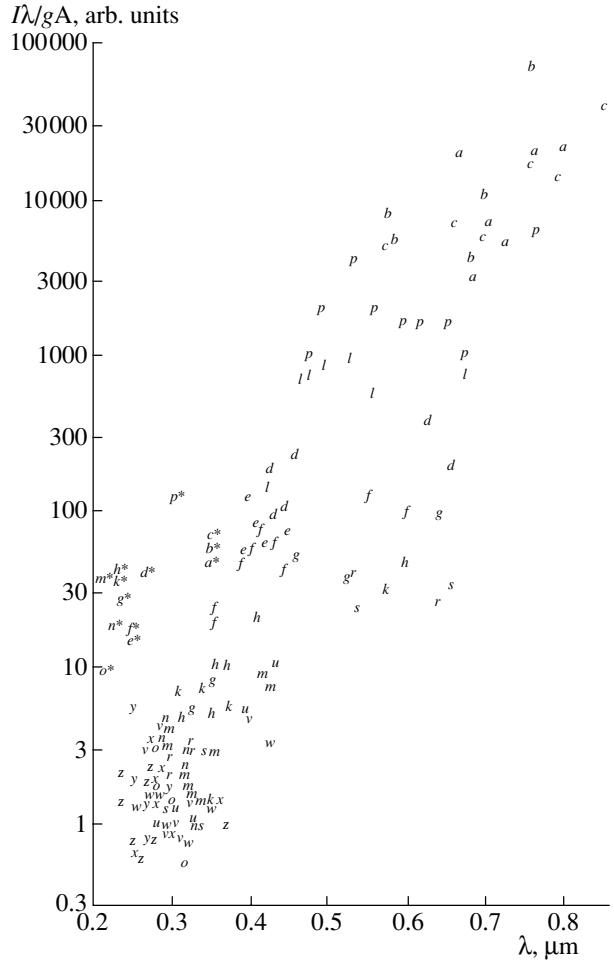

Fig. 4. $I\lambda/gA = f(\lambda)$ at $\lambda = 0.20$–0.85 μm for transitions from the levels studied here and in [16]: (a) 28 854 cm^{-1},(b) 28 889 cm^{-1},(c) 28 961 cm^{-1}, (d) 37 967 cm^{-1},(e) 39 670 cm^{-1},(f) 39 844 cm^{-1}, (g) 42 254 cm^{-1},(h) 43 815 cm^{-1},(k) 44 148 cm^{-1}, (l) 35 267 cm^{-1},(m) 45 937 cm^{-1},(n) 46 352 cm^{-1}, (o) 47 669 cm^{-1},(p) 32 592 cm^{-1},(r) 45 462 cm^{-1}, (s) 45 904 cm^{-1},(u) 47 205 cm^{-1},(v) 49 170 cm^{-1}, (w) 50 869 cm^{-1},(x) 50 205 cm^{-1},(v) 49 170 cm^{-1}, (w) 50 869 cm^{-1},(x) 50 934 cm^{-1},(y) 51 955 cm^{-1}, and (z) 54 177 cm^{-1}.

each of which corresponds to a particular energy level. Not a single point depicting a resonant transition for any of the levels coincides with any of the crosses depicting nonresonant transitions; likewise, there is no superposition of crosses.

Unfortunately, the information presented in Figs. 1–3 does not fully characterize the situation, since it refers only to transitions whose excitational cross sections were measured here and in [16]. In other words, these figures cover a relatively narrow spectral interval due to the technical problems mentioned in Section 2. The studies [7, 10] were carried

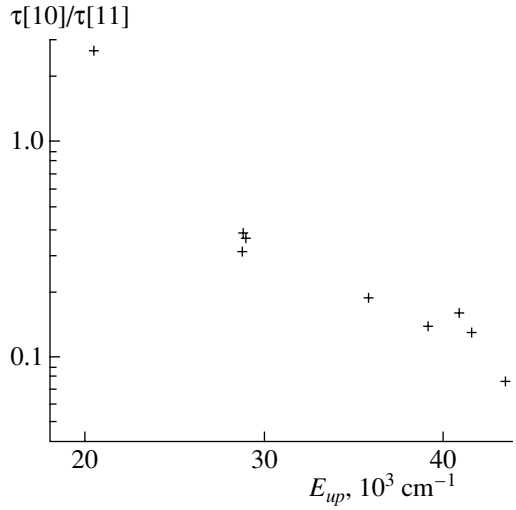

Fig. 5. Ratio $\tau[10]/\tau[11]$ for the data of [11].

out in a wider wavelength range and included less intensive lines. Therefore, these data represent supplementary material for our analysis. Figure 4 shows the $I\lambda/gA$ dependence in the extended wavelength range 0.20–0.85 μm. The transition from each level has an individual letter designation, and resonant lines are marked by asterisks. Along with the levels studied here and in [16], we included the 32 592 cm^{-1} level, which partially fills an extremely large gap between the 28 961 and 35 267 cm^{-1} levels.

We can see that the dependence decreases sharply in the interval 0.2–0.3 μm (which corresponds to the h, k, m, n, and o levels) then increases considerably in the interval 0.3–0.85 μm. The scatter of $I\lambda/gA$ values for transitions from the same upper level can reach three orders of magnitude or more (levels a, b, and c). Since this behavior is similar to that observed earlier for atomic tantalum [12], its most probable origin is systematic errors in [10]; in particular, there was a considerable error in the absolute temperature adopted in [10].

A similar analysis (based on a much smaller amount of experimental data) was undertaken previously in [11]: the radiative lifetimes τ for the energy levels of rhenium measured in [11] and calculated using A_{ki} values taken from [10] were compared. The result is shown in Fig. 5, which we have taken from [11]. The ratio $\tau[10]/\tau[11]$ decreases monotonically and appreciably (by one and a half orders of magnitude) as the energy of the level increases. As was pointed out by Duquette *et al.* [11], using the oscillator strengths calculated using their experimental values of τ considerably improved the agreement between the solar and meteoritic data on the abundance of rhenium.

5. CONCLUSIONS

We have experimentally studied the excitation of atomic rhenium, which has an evaporation temperature of 3600 K. We measured 47 excitational cross sections of nonresonant spectral lines of ReI for an energy of the exciting electrons of 50 eV. Analysis of the available data on the radiative transition probabilities for rhenium show that the range of ratios $I\lambda/gA$ for transitions with a common upper level can reach over three orders of magnitude. As a result, the available values of A_{ki} are not suitable for determining the branching ratios and calculating the excitational cross sections for transitions possessing the same upper levels as those under investigation. Our analysis confirms the conclusions derived previously in studies of the atomic constants of TaI.

REFERENCES

1. L. L. Shimon, I. V. Kurt, and I. I. Garga, Opt. Spektrosk. **56**, 601 (1984) [Opt. Spectrosc. **56**, 368 (1984)].
2. Yu. M. Smirnov, *Physics of Electronic and Atomic Collisions* [in Russian] (FTI AN SSSR, Leningrad, 1985), p. 183.
3. A. N. Kuchenev and Yu. M. Smirnov, Opt. Spektrosk. **51**, 210 (1981) [Opt. Spectrosc. **51**, 116 (1981)].
4. A. N. Kuchenev and Yu. M. Smirnov, Zh. Prikl. Spektrosk. **43**, 1004 (1985).
5. A. N. Kuchenev and Yu. M. Smirnov, Zh. Prikl. Spektrosk. **36**, 188 (1982).
6. W. F. Meggers, J. Res. Natl. Bur. Stand. **49**, 187 (1952).
7. P. F. A. Klinkenberg, W. F. Meggers, R. Velasco, and M. A. Catalan, J. Res. Natl. Bur. Stand. **59**, 319 (1957).
8. J. F. Wyart, Phys. Scr. **18**, 87 (1978).
9. B. Buchholz, H.-D. Kronfeldt, and R. Winkler, Physica C **96**, 297 (1979).
10. C. H. Corliss and W. R. Bozeman, *Experimental Transition Probabilities for Spectral Lines of Seventy Elements* (U.S. Government Printing Office, Washington, D.C., 1962; Mir, Moscow, 1968), p. 305.
11. D. W. Duquette, S. Salih, and J. E. Lawler, J. Phys. B **15**, L897 (1982).
12. Yu. M. Smirnov, Astron. Zh. **79**, 932 (2002) [Astron. Rep. **46**, 840 (2002)].
13. Yu. M. Smirnov, Opt. Spektrosk. **78**, 557 (1995) [Opt. Spectrosc. **78**, 498 (1995)].
14. A. N. Kuchenev, E. A. Samsonova, and Yu. M. Smirnov, Avtometriya **5**, 109 (1990).
15. Yu. M. Smirnov, J. Phys. II (France) **4**, 23 (1994).
16. Yu. M. Smirnov, J. Phys. B (in press).
17. A. G. Gasalinadze, *The System of Energy Levels and Wavelengths of 26 757 Lines of Neutral Iron FeI* [in Russian] (Shemahinskaya Astrofiz. Obs., Baku, 1987).

Translated by Yu. Dumin

Astronomy Reports, Vol. 47, No. 3, 2003, pp. 248–253. Translated from Astronomicheskiĭ Zhurnal, Vol. 80, No. 3, 2003, pp. 274–279.

The Chemical Composition of Stars in the Globular Clusters M 10, M 12, and M 71

T. V. Mishenina[1], V. E. Panchuk[2], and N. N. Samus'[3]

[1]*Astronomical Observatory, Odessa National University, Shevchenko Park, Odessa, 65014 Ukraine*

[2]*Special Astrophysical Observatory, Russian Academy of Sciences, Nizhnii Arkhyz, Karachai-Cherkessian Republic, 357147 Russia*

[3]*Institute of Astronomy, Russian Academy of Sciences, ul. Pyatnitskaya 48, Moscow, 119017 Russia and Sternberg Astronomical Institute, Moscow State University, Universitetskiĭ pr. 13, Moscow, 119992 Russia*

Received June 4, 2002; in final form, October 10, 2002

Abstract—The abundances of 19 chemical elements in the atmospheres of five stars belonging to three globular clusters have been determined by applying the model-atmosphere method to 430.0–790.0 nm spectra obtained with the échelle spectrometer of the 6-m telescope of the Special Astrophysical Observatory. The abundances of silicon, calcium, iron-peak elements, copper, zinc, and neutron-capture elements follow the abundance patterns for halo stars. The abundance of sodium in M 10 giants provides evidence that different mixing mechanisms operate in halo and cluster stars or that light elements are enriched in different ways in the pre-stellar matter from which some globular clusters and halo stars were formed. © *2003 MAIK "Nauka/Interperiodica".*

1. INTRODUCTION

According to our current understanding of the Galaxy's formation and chemical evolution, the stars of each globular cluster share a common origin, i.e. as a rule, we can assume they have approximately the same age and chemical composition. Studies of variations of stellar chemical abundances within a cluster or of chemical composition differences from cluster to cluster provide tests for theories of stellar evolution and of the early stages of Galactic evolution. Recent progress in such studies is considerable. It was found that globular-cluster stars with similar atmospheric temperatures exhibited different intensities of CN, CH, and other molecular bands. Abundance variations within a cluster are shown by CNO-group elements as well as by Na, Mg, Al, and neutron-capture elements [1–7]. A metallicity scatter was noted among stars in some clusters (usually, this means a scatter in [Fe/H], whose bimodal distribution is well known, for example, in the case of the giant cluster ω Cen [8]). Anti-correlations of the oxygen and sodium and of the magnesium and aluminum abundances were found for giant-branch stars, while the sum of the C, N, and O abundances remained constant.

Abundance studies for magnesium isotopes showed that the isotopes ^{26}Mg and ^{25}Mg were missing in aluminum-rich stars [9]; in addition, a deficiency of atomic magnesium was found, even for low-luminosity giants [5]. Applying evolutionary models with deep mixing to globular-cluster giants makes it possible to explain these anomalies [10–13]. Variations of band intensities and anti-correlations between elemental abundances were also noted for main-sequence stars [4, 7, 14]. There is a tendency to explain such effects by invoking inhomogeneity (incomplete mixing) of the pre-stellar matter from which the cluster was formed, or via self-enrichment of the cluster's volume in elements formed inside its stars. It has also been suggested that the presence of CN-strong and CN-weak stars could be due to differences in the temperature structure of their atmospheres, due to differences in molecular blanketing. Drake *et al.* [15] showed that including the effects of blanketing and of the atmosphere's geometric structure led to abundance effects below 0.1 dex. Individual spectral features for stars of similar masses have also been explained using nucleosynthesis on the giant branch [16, 17], accretion of enriched stellar wind material from nearby asymptotic giant-branch (AGB) stars, and the clusters' dynamic properties or masses [7]. In some cases, the hypothesis of different degrees of mixing in the envelopes has been put forward, making information on the abundance of lithium very important for testing models, since this element is rapidly disrupted during the evolution of the convective envelope, but can also be synthesized during shell burning of hydrogen. This information can be deciphered using data on the abundances of CNO-group elements, Na, Mg, Al, and *s*-process

1063-7729/03/4703-0248$24.00

Table 1. Basic data on the program stars

Cluster	Star	Reference	V	$B-V$	Observation date, July 2000	α_{2000}	δ_{2000}	Spectrum no.
M 10[1]	II-105	[24] ($m_{\rm pv}$ and CI)	12.79	1.37	5/6	$16^{\rm h}56^{\rm m}59.4^{s}$	$-04°05'44''$	s28305
M 10[1]	I-70	[24] ($m_{\rm pv}$ and CI)	13.87	1.20	9/10	16 57 17.4	−04 02 42	s28608
M 12[2,3]	K118	[25, 26]	13.11	0.89	12/13	16 47 08.5	−02 01 36	s27602
M 71[4]	I-9	[27]	13.29	1.27	9/10	19 53 49.1	+18 46 00	s28611
M 71[4,5]	I-30	[27, 28]	12.09	1.74	10/11	19 53 53.7	+18 47 04	s28708
					12/13			s28801

elements, which appear in stellar atmospheres at late evolutionary stages.

This paper continues studies of elemental abundances in the atmospheres of stars in globular clusters having different metallicities and differently populated blue sides of the horizontal branch, compared to analogous field stars [18–20]. Our study is based on high-resolution spectra with high signal-to-noise ratios.

2. OBSERVATIONS AND THEIR REDUCTION

Spectrograms of the program stars were acquired with the PFES échelle spectrograph of the 6 m telescope of the Special Astrophysical Observatory (Russian Academy of Sciences). The spectral resolution was $R = 15\,000$, and wavelengths from 430.0 to 790.0 nm were studied. Each spectrogram results from the joint reduction of two consecutive échelle images. In this way, we excluded interference from cosmic-ray traces. We reduced the images and spectrograms using the MIDAS [22] and DECH20 [23] packages.

A list of our program stars together with their V (or m_{pv}) magnitudes, B–V color indices (CI), observation dates, and coordinates are presented in Table 1. This table also contains references for the designations of the stars used and the photometric data [24–28].

3. CHOICE OF MODEL-ATMOSPHERE PARAMETERS

All three globular clusters studies suffer considerable interstellar reddening. For example, the reddening values $E(B-V)$ in the literature for the globular cluster M 71, which is located nearly in the Galactic plane (at a Galactic latitude of about $-5°$) range from 0.21 to 0.32. This is a serious obstacle when using color indices to determine the effective temperature, $T_{\rm eff}$. If we adopt $E(B-V) = 0.25$ [29], the estimates of $T_{\rm eff}$ for the stars I-9 and I-30 derived using the calibration of Alonso *et al.* [30] and their $(B-V)$ color indices taking into account their metallicities are 4350 K and 3600 K, respectively. However, the value obtained in [31] for I-30 using the infrared flux method and $E(B-V) = 0.25$ was $T_{\rm eff} = 3900$ K. There is also considerable uncertainty in the interstellar reddening for the globular cluster M 10: estimates range from 0.27 [32] to 0.17 [33]. According to Kraft *et al.* [33], this difference leads to errors $\Delta T_{\rm eff} = 125$ K, $\Delta \log g = 0.4$, and Δ[Fe/H] = 0.06 dex. Interstellar reddening is also appreciable for M 12: 0.17 [34].

There exist methods to determine $T_{\rm eff}$ directly from spectroscopic material that do not depend on allowing for interstellar reddening. These use the profiles of Hα lines, whose far wings are sensitive to changes of the effective temperature and, for metal-poor stars, are virtually independent of the surface gravity, $\log g$, and metallicity, [Fe/H] [35]. Unfortunately, the wings become less sensitive for $T_{\rm eff} < 4800$ K (the uncertainty increases to ± 200 K). In this temperature domain, as a rule, the $T_{\rm eff}$ values derived from Hα lines are too high, and this method can be used only as an additional check. In some cases, the core of the Hα line is known to be distorted by an emission component.

Another spectroscopic method is to determine $T_{\rm eff}$ from the condition that the abundance of an element (usually iron) derived from a particular line not depend on the potential of the lower level of this line, $E_{\rm low}$. Figure 1 shows an example of the relation between the iron abundance, log$A$(FeI), and $E_{\rm low}$ for the star M 10 II-105.

We determined the surface gravity, $\log g$, from the condition of ionization equilibrium for atoms and ions of iron, and derived the microturbulence velocity, V_t, from the condition that the iron abundance derived from a particular line not depend on its equivalent width. The resulting parameters are given in Table 2.

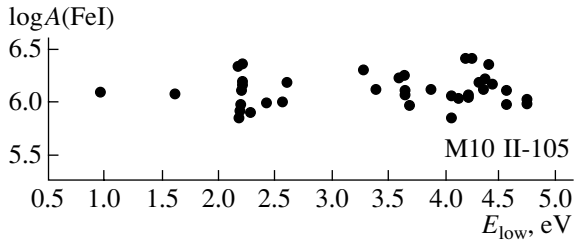

Fig. 1. Relation between the iron abundance, $\log A(\mathrm{FeI})$, derived from a line on the potential of the lower level of this line, E_{low}, for the star M 10 II-105.

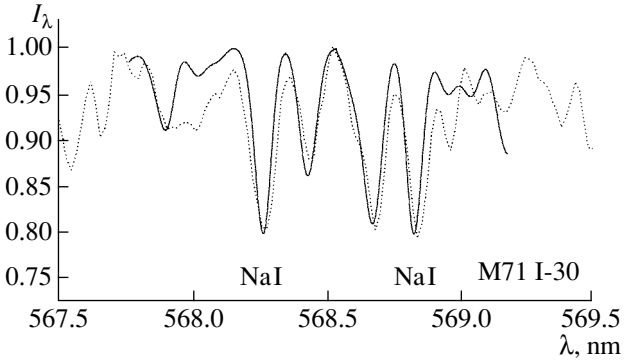

Fig. 2. Comparison between the synthetic spectrum (solid curve) and observed spectrum (dashed curve) in the region of the sodium 568.0 nm line for the star M 10 I-30. The synthetic spectrum was computed for the sodium abundance $\log A(\mathrm{Na}) = 5.62$ on a scale with $\log A(\mathrm{H}) = 12$.

The mean errors of the parameters are: $\Delta T_{\mathrm{eff}} = \pm 100$ K, $\Delta \log g = \pm 0.3$, and $\Delta V_t = \pm 0.2$ km/s. We also estimated the radial velocities of the program stars, V_r, from their Hα lines. The results in Table 2 are in good agreement with the mean radial velocities of the corresponding clusters' member stars [36], with the exception of the star K118 in M 12. The discrepancy may be due to distortion of the Hα-line core by weak emission, as is observed for stars at the tip of the red-giant branch or on the AGB. Note that K118 has a high probability of membership in M 12 (93%) according to the estimate of [26] based on proper motions.

4. DETERMINATION OF THE CHEMICAL COMPOSITION

We computed the abundances of the program stars using the WIDTH9 code of Kurucz. We selected the model atmospheres via a standard interpolation in Kurucz's grid of model atmospheres [37]. The list of lines was compiled using a synthetic spectrum computed by the STARSP routine [38] for the studied range of temperatures and metallicities. The oscillator strengths, $\log gf$, were taken from Gurtovenko and Kostyk [39]. We derived the abundances of sodium and magnesium using the synthetic spectrum technique in the region of the NaI 568.2, 568.8 nm and 615.4, 616.0 nm lines and of the MgI 571.1 nm line. An example of a comparison between a synthetic spectrum (solid curve) and observed spectrum (dashed curve) in the region of the sodium 568.0–569.0 nm lines for the star I-30 in the globular cluster M 71 is shown in Fig. 2. We also determined the abundances of copper using the synthetic-spectrum method, from the CuI 510.5, 521.8, 578.2 nm lines; data on the components of the hyperfine structure were taken from [40]. The errors of the synthetic spectrum fitting were ± 0.05 dex.

Table 2. Atmospheric parameters of the program stars

Cluster	Star	T_{eff}, K	$\log g$	V_t, km/s	V_r, km/s
M 10	II-105	4400	1.1	1.6	72.5
M 10	I-70	4600	1.3	1.5	71.8
M 12	K118	4800	1.8	1.6	44.6
M 71	I-9	4500	1.75	1.6	−22.6
M 71	I-30	4000	1.0	1.6	−40.7

In the spectra of all the program stars, the 630.03 nm oxygen line is distorted by the ionospheric oxygen emission line, so that we were unable to determine the oxygen abundances. The resultant [A/H] values relative to the solar abundances [39] are given in Table 3, where σ is the rms error of an individual determination and n is the number of lines used for the analysis.

5. MAIN RESULTS AND CONCLUSIONS

(1) The metallicities of stars in the studied clusters coincide within a cluster and are in a good agreement with earlier results for these clusters (M 10: [33]; M 71: [41, 42]).

(2) For the stars of M 71, the Na abundance agrees well with the iron abundance, so that the [Na/Fe] ratio is practically solar. The two stars of M 10 show considerably different sodium abundances (by approximately 0.3 dex). Taking into account non-LTE effects does not remove this discrepancy. The non-LTE corrections for the two stars (which have similar parameters) are close to each other and do not exceed 0.15 dex. This estimate is based on the model of the sodium atom from [43]. Not-LTE effects are actually even less significant: they were implicitly taken into account in the oscillator strengths we used [39].

A similar difference in the behavior of sodium was noted earlier for stars in the clusters M 10 and M 71

Table 3. Abundances, [A/H], in the atmospheres of the program stars

Ion	M 10 II-105			M 10 I-70			M 12 K118			M 71 I-9			M 71 I-30		
	[A/H]	σ	n	[A/H]	σ	n	[A/H]	σ	n	[A/H]	σ	n	[A/H]	σ	n
FeI	−1.51	0.14	40	−1.51	0.22	27	−1.31	0.22	38	−0.78	0.15	39	−0.81	0.23	23
FeII	−1.56	0.11	5	−1.53	0.19	5	−1.40	0.06	3	−0.81	0.15	5	−0.79	0.12	2
NaI	−1.40	–	4	−1.12	–	2	−1.22	–	4	−0.80	–	2	−0.75	–	4
MgI	−1.44	–	1	–	–	–	−1.07	–	1	−0.86	–	1	−0.71	–	1
SiI	−1.21	0.07	3	−1.16	0.06	3	−0.96	0.18	4	−0.56	0.16	7	−0.61	0.09	4
CaI	−1.12	0.23	2	−1.28	0.09	2	−1.03	0.00	1	−0.54	0.02	3	–	–	–
ScII	−1.41	0.12	5	−1.43	0.01	2	−1.34	0.00	1	−0.74	0.41	3	−0.83	0.03	2
TiI	−1.22	0.21	13	−1.19	0.36	13	−0.93	0.22	17	−0.63	0.18	10	−0.66	0.11	11
TiII	−1.31	0.21	5	−1.32	0.36	6	−1.06	0.20	4	−0.70	0.01	2	–	–	–
VI	−1.46	0.05	6	−1.51	0.00	1	−1.38	0.17	6	−0.83	0.19	2	−0.78	0.00	1
CrI	−1.55	0.05	5	−1.44	0.24	7	−1.37	0.17	6	−0.86	0.16	6	−0.81	0.00	1
CrII	−1.61	0.00	1	−1.51	0.01	2	−1.36	0.07	3	−0.79	0.17	3	–	–	–
MnI	−1.52	0.19	5	−1.57	0.20	5	−1.31	0.18	4	−0.87	0.11	4	−0.87	0.10	2
CoI	−1.51	0.06	2	−1.50	0.08	2	−1.42	0.00	1	–	–	–	−0.84	0.00	1
NiI	−1.56	0.13	16	−1.48	0.07	7	−1.32	0.15	7	−0.85	0.18	13	−0.79	0.05	4
CuI	−2.10	–	2	–	–	–	−1.80	–	1	−1.15	–	2	−1.10	–	3
ZnI	–	–	–	−1.49	0.00	1	−1.45	0.00	1	−0.89	0.00	1	–	–	–
YII	−1.51	0.31	3	−1.47	0.00	1	−1.28	0.01	2	−0.60	0.05	2	−0.73	0.00	1
BaII	−1.39	0.09	2	−1.34	0.10	2	−1.44	0.19	2	−0.69	0.00	1	−0.78	0.00	1
LaII	−1.40	0.00	1	–	–	–	–	–	–	–	–	–	−0.64	0.21	2
CeII	–	–	–	–	–	–	−1.46	0.21	2	–	–	–	−0.82	0.00	1
NdII	−1.49	0.12	2	−1.40	0.00	1	–	–	–	–	–	–	–	–	–

(M 10: [33]). In the papers on halo stars [5, 35], it was shown that the abundance of sodium relative to iron followed the solar ratio, and the stars in M 71 behave in this way. However, some clusters, in particular M 13 and M 3 [44, 45], display considerable scatters in their sodium (and oxygen) abundances, and M 10 is now added to this list. This result may represent evidence for differences in the evolution of different groups of globular clusters, as well as for halo stars, which are not described adequately in a unified chemical-evolution scenario.

(3) The magnesium-to-iron ratios demonstrated by the program stars are virtually solar; this ratio is somewhat higher for the star M 12 K118. The [Mg/Fe] ratios for halo stars exhibit excesses (by about 0.3–0.4 dex), similar to the ratios for other α elements [20]. Taking into account non-LTE effects for the magnesium lines confirms the presence of a [Mg/Fe] excess for the halo stars [46].

(4) Our abundances of α elements (silicon, calcium) relative to iron are, on average, 0.2–0.3 dex higher than the solar ratios, and also demonstrate good agreement with earlier results for the clusters studied (M 10: [33]; M 71: [41]), as well as for halo stars in general [20].

(5) The abundance of copper relative to iron, [Cu/Fe], is reduced compared to the solar value, while the abundance of zinc corresponds to the solar [Zn/Fe] ratio. This agrees well with the behavior of copper and zinc for halo stars [47].

(6) The neutron-capture elements characterize the course of the s-process during the late stages of stellar evolution and the presence of mixing.

Generally, all the studied stars demonstrate near-solar abundances of yttrium, barium, lanthanum, and cerium (relative to iron), although one of the stars (M 71 I-9) has been classified as an AGB star, and the star M 12 K118 can also be identified as a AGB star based on its color index and position in the color–luminosity diagram [34].

(7) Globular-cluster giants do not display considerable amounts of lithium. As for halo giants [48], their atmospheric lithium is depleted in the course of their evolution. However, the presence of lithium was revealed for three giants in three globular clusters, one of which is a W Vir star [49]. The suspected mechanism leading to the presence of lithium is Li production in the hydrogen-burning shell during the AGB stage, with subsequent transport to the surface layers due to deep mixing. In the spectra of our program stars, a lithium line is observed only for the star M 12 K118. Using this line, we determined the lithium abundance, $\log A(\mathrm{Li}) = 1.0$ on a scale with $\log A(\mathrm{H}) = 12$. This value is in a good agreement with the predicted lithium depletion during the star's evolution.

Our study leads us to conclude that the abundances of silicon, calcium, iron-peak elements, copper, zinc, and neutron-capture elements for the program globular-cluster stars correspond to these elements' abundances in halo stars of the same metallicity. The sodium abundance derived by us for giants of the globular cluster M 10 provides evidence for either different efficiencies of the mixing mechanisms in cluster and halo stars or different schemes for enrichment of the pre-stellar matter in light elements in some globular clusters and the halo.

ACKNOWLEDGMENTS

T. V. Mishenina thanks S. A. Korotin for his assistance during the non-LTE computations. V. E. Panchuk's studies were supported by the Russian Foundation for Basic Research (project no. 01-02-16093a). Thanks are due to the referee for valuable suggestions for the improvement for the text of this paper.

REFERENCES

1. J. A. Brown and G. Wallerstein, Astron. J. **104**, 1818 (1992).
2. R. P. Kraft, Publ. Astron. Soc. Pac. **106**, 553 (1994).
3. J. Norris and G. S. Costa, Astrophys. J. **441**, L81 (1995).
4. J. J. Cohen, Astron. J. **117**, 2434 (1999).
5. C. A. Pilachowski, C. Sneden, R. P. Kraft, and G. E. Langer, Astron. J. **112**, 545 (1996).
6. I. I. Ivans, C. Sneden, R. P. Kraft, *et al.*, Astron. J. **118**, 1273 (1999).
7. R. G. Gratton, P. Bonifacio, A. Bragaglia, *et al.*, Astron. Astrophys. **369**, 87 (2001).
8. G. Cayrel de Strobel and C. Soubiran, *The Galactic Halo: From Globular Clusters to Field Stars*, Ed. by A. Noels, P. Magaine, D. Caro *et al.* (Inst. d'Astrophysique et de Geophysique, Liège, 2000), p. 191.
9. M. D. Shetron, Astron. J. **112**, 2639 (1996).
10. G. E. Langer, R. Hoffman, and C. Sneden, Publ. Astron. Soc. Pac. **105**, 301 (1993).
11. P. A. Denissenkov, G. S. Da Costa, J. E. Norris, and A. Weiss, Astron. Astrophys. **333**, 926 (1998).
12. M. Y. Fujimoto, M. Aikawa, and K. Kato, Astrophys. J. **519**, 733 (1999).
13. M. Aikawa, M. Y. Fujimoto, and K. Kato, Astrophys. J. **560**, 937 (2001).
14. M. M. Briley and J. G. Cohen, Astron. J. **122**, 242 (2001).
15. J. J. Drake, B. Plez, and V. V. Smith, Astrophys. J. **412**, 612 (1993).
16. N. Suntzeff, *The Globular Clusters–Galaxy Connection*, Ed. by G. H. Smith and J. P. Brodie; Astron. Soc. Pac. Conf. Ser. **48**, 167 (1993).
17. R. H. Cavallo, A. V. Sweigart, and R. A. Bell, Astrophys. J. **492**, 575 (1998).
18. V. G. Klochkova, T. V. Mishenina, and V. E. Panchuk, Astron. Astrophys. **287**, 881 (1994).
19. V. G. Klochkova and T. V. Mishenina, Astron. Zh. **75**, 349 (1998) [Astron. Rep. **42**, 307 (1998)].
20. T. V. Mishenina and A. V. Kovtyukh, Astron. Astrophys. **370**, 951 (2001).
21. V. E. Panchuk, I. D. Najdyenov, V. G. Klochkova, *et al.*, Bull. Spec. Astrophys. Observ. **44**, 127 (1998).
22. *Midas Users Guide* (Data Analysis Group, ESO, 1995).
23. G. A. Galazutdinov, Preprint SAO RAN No. 92 (1992).
24. H. C. Arp, Astron. J. **60**, 317 (1955).
25. F. Küstner, Veröeff. Astron. Inst. Bonn **26**, 1 (1933).
26. M. Geffert, H.-J. Tucholke, Ts. B. Georgiev, and J.-F. LeCampion, Astron. Astrophys., Suppl. Ser. **191** (3), 487 (1991).
27. H. C. Arp and F. D. A. Hartwick, Astrophys. J. **167**, 499 (1971).
28. R. M. Cudworth, Astron. J. **90**, 65 (1985).
29. W. E. Harris, Astron. J. **112**, 1487 (1996).
30. A. Alonso, S. Arribas, and C. Martinez-Roger, Astron. Astrophys., Suppl. Ser. **117**, 227 (1996).
31. A. Alonso, S. Arribas, and C. Martinez-Roger, Astron. Astrophys., Suppl. Ser. **139**, 335 (1999).
32. D. J. C. Hurley, H. B. Richter, and G. G. Faxlman, Astron. J. **98**, 2124 (1989).
33. R. P. Kraft, C. Sneden, G. E. Langer, *et al.*, Astron. J. **109**, 2586 (1995).
34. R. Racine, Astron. J. **76**, 331 (1971).
35. R. G. Gratton, C. Sneden, E. Carretta, and A. Bragaglia, Astron. Astrophys. **354**, 169 (2000).
36. A. S. Rastorguev and N. N. Samus', Pis'ma Astron. Zh. **17**, 915 (1991) [Sov. Astron. Lett. **17**, 388 (1991)].
37. R. Y. Kurucz, CD-ROM No. 13 (1993).

38. V. I. Tsymbal, *Model Atmospheres and Spectrum Synthesis*, Ed. by S. J. Adelman, F. Kupka, and W. W. Weiss; Astron. Soc. Pac. Conf. Ser. **108**, 198 (1996).
39. E. A. Gurtovenko and R. I. Kostyk, *The Fraunhofer Spectrum and the System of Oscillator Strengths for the Sun* [in Russian] (Naukova Dumka, Kiev, 1989), p. 196.
40. M. Steffen, Astron. Astrophys., Suppl. Ser. **59**, 403 (1985).
41. C. Sneden, R. P. Kraft, G. E. Langer, *et al.*, Astron. J. **107**, 1773 (1984).
42. S. V. Ramirez, J. G. Cohen, J. Buss, and M. M. Briley, Astron. J. **122**, 1429 (2001).
43. S. A. Korotin and T. V. Mishenina, Astron. Zh. **76**, 611 (1998) [Astron. Rep. **43**, 533 (1999)].
44. R. P. Kraft, C. Sneden, G. E. Langer, and C. F. Prosser, Astron. J. **104**, 645 (1992).
45. R. P. Kraft, C. Sneden, G. E. Langer, and M. D. Shetron, Astron. J. **106**, 1490 (1993).
46. N. N. Shimanskaya and L. T. Mashonkina, Astron. Zh. **78**, 122 (2001) [Astron. Rep. **45**, 100 (2001)].
47. C. Sneden, R. G. Gratton, and D. A. Crocker, Astron. Astrophys. **246**, 354 (1991).
48. C. A. Pilachowski, C. Sneden, and J. Booth, Astrophys. J. **407**, 699 (1993).
49. R. P. Kraft, *The Galactic Halo: From Globular Clusters to Field Stars*, Ed. by A. Noels, P. Magaine, D. Caro, *et al.* (Inst. d'Astrophysique et de Geophysique, Liège, 1999), p. 177.

Translated by N. Samus'

Astronomy Reports, Vol. 47, No. 3, 2003, pp. 254–262. Translated from Astronomicheskiĭ Zhurnal, Vol. 80, No. 3, 2003, pp. 280–288.

Types of Motions in the Rectilinear Three-Body Problem with Unequal Masses

V. V. Orlov[1], A. V. Petrova[1], and A. I. Martynova[2]

[1] *Astronomical Institute, St. Petersburg State University, St. Petersburg, Russia*

[2] *St. Petersburg Forest Technical Academy, Institutskiĭ per. 5, St. Petersburg, 194022 Russia*

Received June 7, 2002; in final form, August 21, 2002

Abstract—The motions in the rectilinear three-body problem are analyzed for the case of unequal masses. At the initial time, the central body is equidistant from the outer bodies. The initial conditions for a fixed ratio of the body masses are determined by two parameters: the virial coefficient of the triple system and the ratio of the differences in the velocities of the central body and the two outer bodies. The domains of the initial conditions corresponding to the escape of one of the outer bodies after some number $n = \{1, 2, 3, 4, 5\}$ of passes of the central body through the barycenter of the triple system are identified. When $n \leqslant 2$, these domains are continuous manifolds. When $n \geqslant 3$, structures consisting of "scattered" points begin to emerge. The changes in the topological properties and in the areas of the continuous domains are determined by the variation of the ratios of the body masses. The domains of the initial conditions for long-lived triple systems are also found, as well as areas within these corresponding to stable systems with bound motions. © *2003 MAIK "Nauka/Interperiodica"*.

1. INTRODUCTION

The question of motions in the general three-body problem has attracted attention for a long time. A mathematical description of the trajectories of the motion of the bodies in this problem proves to be very complex, despite the simple formulation of the problem itself. To achieve a better understanding of the structure of the set of orbits in this problem, it is of interest to analyze some limiting cases, such as the rectilinear problem, equilateral problem, central configurations, etc.

In this paper, we analyze the rectilinear three-body problem with unequal masses. In this case, the bodies are always located on a straight line along which they move. This problem has been considered in many studies (see [1–9] and references therein).

Chazy [1] has analyzed the possible types of final motions in this problem. Von Schubart [2] found the initial conditions for the central periodic orbit for which the central body undergoes successive collisions with each of the outer bodies at equal time intervals. In this case, the central body passes through the center of mass of the triple system at a certain velocity at intervals equal to half the period. Mc Gehee [3] analyzed the neighborhood of the triple collision and showed that the orbit that ends with a triple collision asymtotically approaches a central configuration in which the outer bodies are at symmetrical points relative to the central body and approach the latter at equal relative velocities. He also showed that there exist certain ratios of the masses of the bodies for which the triple collisions cannot be regularized for any value of the integral of motion.

In his series of papers, Hènon ([3] and references therein) found central periodic orbits similar to the von Schubart orbit and analyzed their stability in a linear approximation for various ratios of the body masses. Broucke and Walker [5] found several families of periodic orbits via numerical simulations. Yoshida [6] analytically analyzed the motions in the rectilinear three-body problem and derived a condition for the escape of one of the outer bodies.

Hietarinta and Mikkola [7] (see also references therein) performed extensive numerical simulations. They showed that the domain of initial conditions contains three manifolds corresponding to (1) the rapid escape of one of the outer bodies ("fast scattering"); (2) long evolution that ends in disruption ("chaotic scattering"), and trajectories with bound motions ("quasiperiodic orbits"). They also showed that the stability of the von Schubart orbit is correlated with the global behavior of the set of bound trajectories with similar patterns of motion. If the von Schubart orbit is unstable, quasiperiodic orbits and some types of orbits with chaotic scattering are virtually absent.

Tanikawa and Mikkola [8, 9] classified the orbits in the rectilinear three-body problem with equal masses using the methods of symbolic dynamics (see, e.g., [10–12] and references therein). Each trajectory is

1063-7729/03/4703-0254$24.00

Fractions of trajectories with various n

ε_1	n	ε_2				
		0.2	0.5	1	2	5
0.2	1	0.164	0.160	0.162	0.161	0.164
	2	0.086	0.078	0.087	0.087	0.143
	3	0.200	0.229	0.227	0.228	0.244
	4	0.048	0.072	0.148	0.239	0.230
	5	0.060	0.042	0.048	0.050	0.038
	1–5	0.558	0.581	0.672	0.765	0.819
	stable	0.016	0.003	0.005	0.001	0
0.5	1	0.160	0.151	0.141	0.140	0.145
	2	0.078	0.048	0.045	0.057	0.088
	3	0.229	0.266	0.207	0.194	0.202
	4	0.072	0.051	0.101	0.235	0.240
	5	0.041	0.032	0.028	0.041	0.042
	1–5	0.580	0.548	0.522	0.667	0.717
	stable	0.003	0.020	0.013	0.007	0.004
1	1	0.162	0.141	0.133	0.122	0.122
	2	0.087	0.045	0.028	0.027	0.050
	3	0.227	0.207	0.091	0.048	0.033
	4	0.148	0.101	0.072	0.166	0.134
	5	0.048	0.029	0.009	0.053	0.049
	1–5	0.672	0.523	0.333	0.416	0.389
	stable	0.005	0.015	0.094	0.061	0.141
2	1	0.161	0.140	0.122	0.110	0.103
	2	0.087	0.057	0.027	0.013	0.023
	3	0.228	0.194	0.048	0.012	0.008
	4	0.239	0.235	0.166	0.133	0.015
	5	0.050	0.041	0.053	0.004	0.140
	1–5	0.765	0.667	0.416	0.272	0.289
	stable	0.001	0.005	0.061	0.624	0.374
5	1	0.164	0.145	0.122	0.103	0.098
	2	0.143	0.088	0.050	0.023	0.007
	3	0.244	0.202	0.033	0.008	0.003
	4	0.230	0.240	0.134	0.015	0.004
	5	0.038	0.042	0.049	0.140	0.006
	1–5	0.819	0.717	0.388	0.289	0.118
	stable	0	0.003	0.145	0.378	0.526

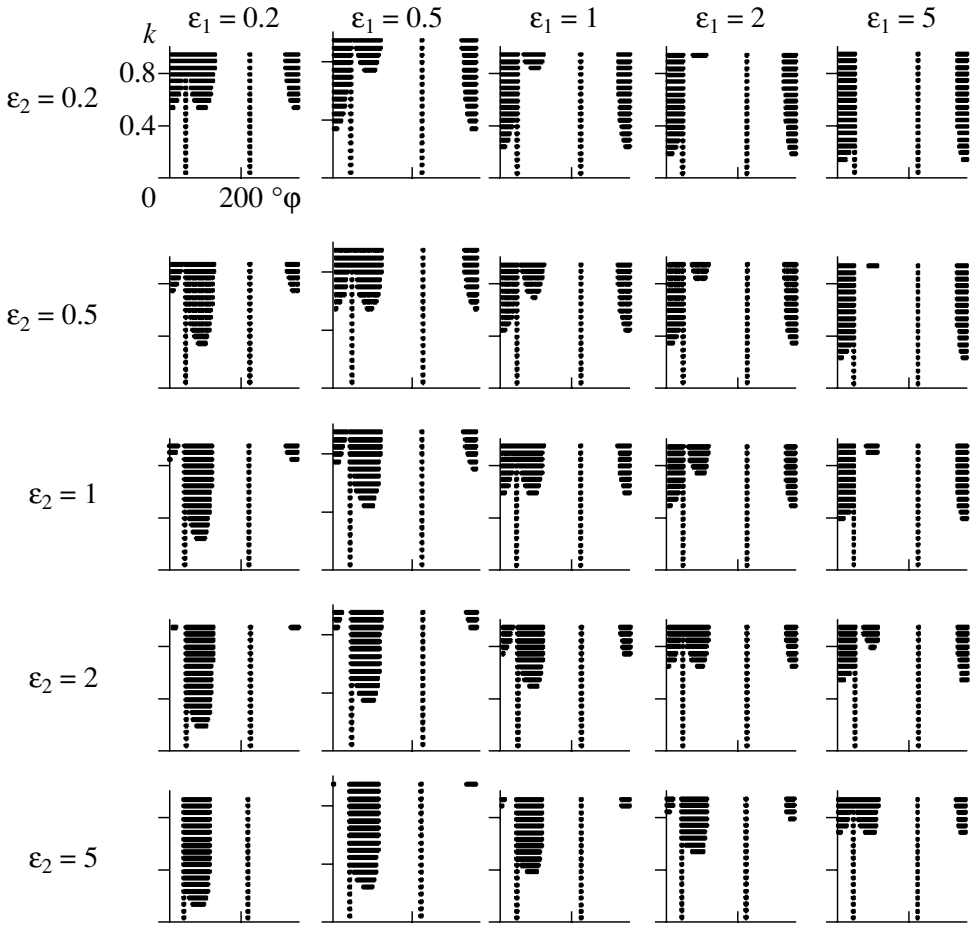

Fig. 1. Regions of escape after the first ($n = 1$) passage of the central body through the barycenter of the triple system for various mass ratios (ε_1, ε_2). The x and y axes plot the parameters φ (in degrees) and k. The vertical lines correspond to $\varphi = 45^\circ$ and $\varphi = 225^\circ$. Initial conditions in the interval $\varphi \in (45^\circ, 225^\circ)$ result in the escape of the left outer body and those in the remaining region in the escape of the right body.

assigned a symbolic sequence of numbers 0, 1, 2 indicating a triple collision and the collision of the central body with each of the outer bodies. Subsets of points in the domain of initial conditions corresponding to different symbolic sequences, i.e., to different scenarios for the dynamic evolution of the system, are identified. These sequences are separated by lines corresponding to triple collisions. Inadmissible symbolic sequences were also found. Along with the domain of quasiperiodic orbits in the vicinity of the von Schubart orbit, these authors identified other periodic orbits and the corresponding periodic symbolic sequences. The set of periodic orbits is infinite. Oscillating orbits were shown to exist and all admissible symbolic sequences were shown to form a Cantor set.

This work continues the research of Hietarinta, Mikkola, and Tanikawa. We analyze the evolution of a triple system as a function of the initial conditions, and find the domains of initial parameters and mass ratios corresponding to various dynamical scenarios, in particular, to various numbers of triple collisions preceding the disruption of the triple system.

2. NUMERICAL SIMULATIONS: EQUATIONS OF MOTION AND INITIAL PARAMETERS

In the rectilinear three-body problem, the central body undergoes a number of double collisions with the outer bodies in the course of the system's evolution. Here, we analyze the motions of the outer bodies relative to the central body. We introduce the following notation:

(1) r is the distance between the left outer body of mass m_1 and the central body of mass m_0;

(2) ρ is the distance between the central body and the right outer body of mass m_2;

(3) $\varepsilon_1 = m_1/m_0, \varepsilon_2 = m_2/m_0, \varepsilon_1$, and $\varepsilon_2 \in [0, \infty)$.

In this paper, we analyze triple systems with negative total energies $E < 0$ and use a system of units

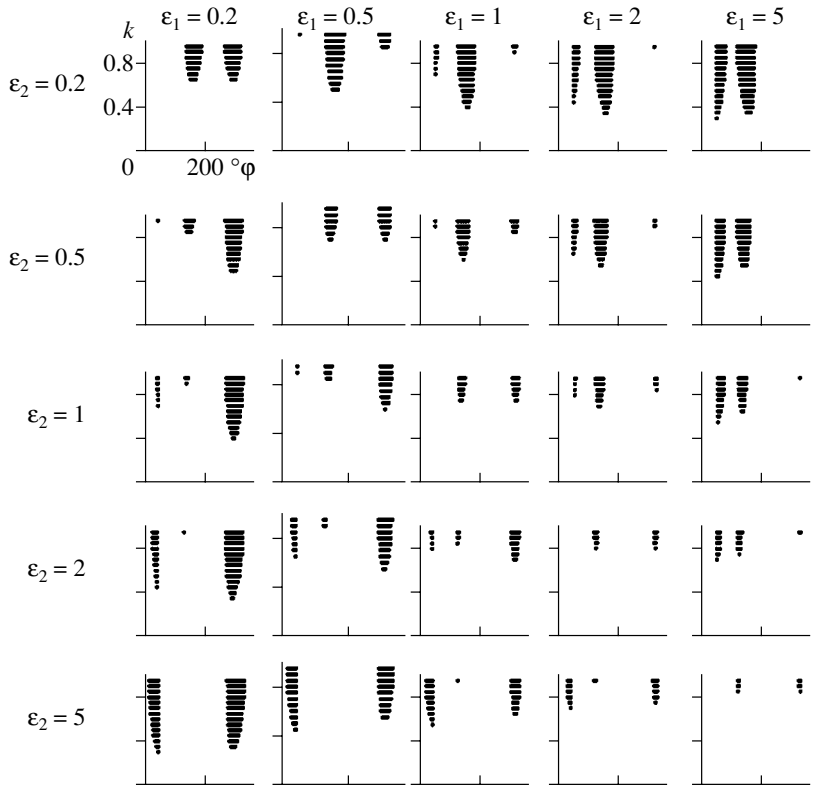

Fig. 2. Same as Fig. 1 for the second passage ($n = 2$).

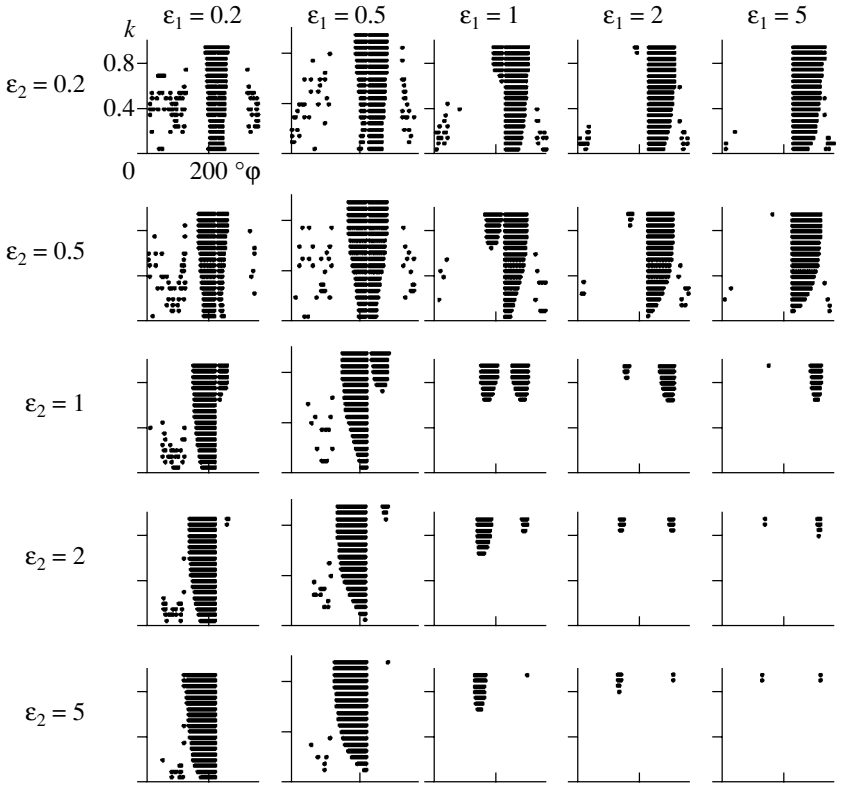

Fig. 3. Same as Fig. 1 for the third passage ($n = 3$).

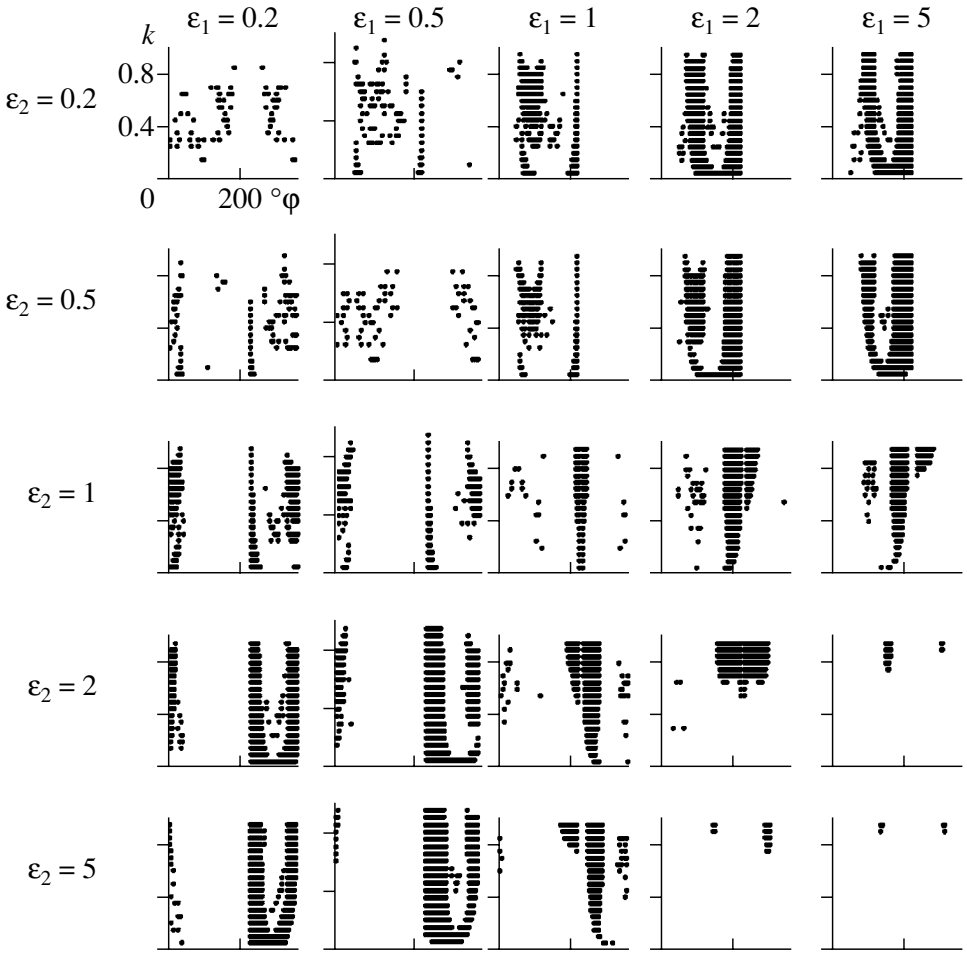

Fig. 4. Same as Fig. 1 for the fourth passage ($n = 4$).

in which $m_0 = 1$, $E = -1$, and the gravitational constant $G = 1$.

The equations of motions have the form

$$\ddot{r} = -\frac{m_0 + m_1}{r^2} + \frac{m_2}{\rho^2} - \frac{m_2}{(r+\rho)^2} \tag{1}$$
$$= -\frac{1+\varepsilon_1}{r^2} + \frac{\varepsilon_2}{\rho^2} - \frac{\varepsilon_2}{(r+\rho)^2},$$

$$\ddot{\rho} = -\frac{m_0 + m_2}{\rho^2} + \frac{m_1}{r^2} - \frac{m_1}{(r+\rho)^2} \tag{2}$$
$$= -\frac{1+\varepsilon_2}{\rho^2} + \frac{\varepsilon_1}{r^2} - \frac{\varepsilon_1}{(r+\rho)^2}.$$

The system of equations (1) and (2) has the energy integral

$$E = T + U = \frac{1}{2}\left[\frac{m_1(m_0+m_1)}{M}\dot{r}^2 + \frac{2m_1m_2}{M}\dot{r}\dot{\rho} + \frac{m_2(m_0+m_1)}{M}\dot{\rho}^2\right] \tag{3}$$
$$- \frac{m_0m_1}{r} - \frac{m_0m_2}{\rho} - \frac{m_1m_2}{(r+\rho)},$$

where $M = m_0 + m_1 + m_2 = 1 + \varepsilon_1 + \varepsilon_2$ is the total mass of the triple system, and T and U are the kinetic and potential energies, respectively. The energy integral then has the form

$$\frac{1}{2M}\left[\varepsilon_1\dot{r}^2 + \varepsilon_2\dot{\rho}^2 + \varepsilon_1\varepsilon_2(\dot{r}+\dot{\rho})^2\right] - \frac{\varepsilon_1}{r} - \frac{\varepsilon_2}{\rho} - \frac{\varepsilon_1\varepsilon_2}{r+\rho} = -1. \tag{4}$$

To smooth the singularities during double encounters, we introduce the change of the time variable t

$$du = (r\rho)^{-3/2}\,dt \tag{5}$$

and the velocities

$$\alpha = \rho(r\rho)^{1/2}\,\dot{r}, \tag{6}$$

$$\beta = r(r\rho)^{1/2}\,\dot{\rho}. \tag{7}$$

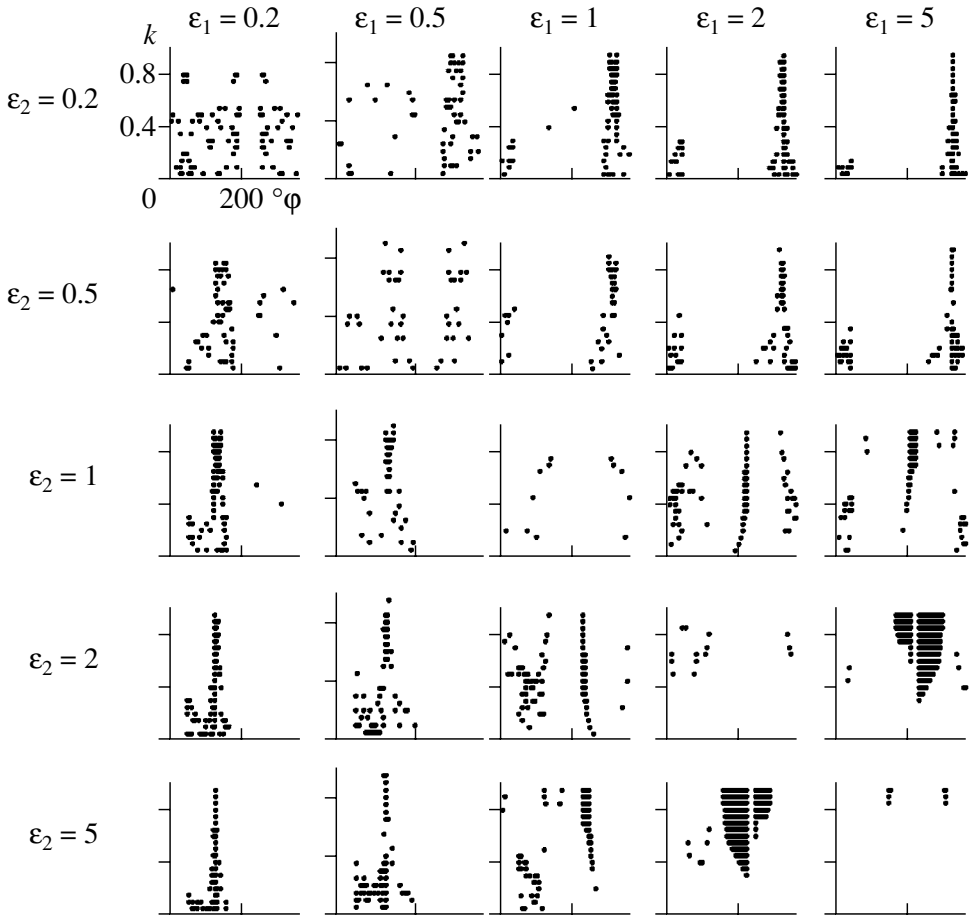

Fig. 5. Same as Fig. 1 for the fifth passage ($n = 5$).

In the case of double collisions $r < \delta = 10^{-6}$ or $\rho < \delta = 10^{-6}$, the colliding bodies rebound elastically in a reference frame fixed to their center of mass.

We choose the initial conditions as follows. We specified the following two parameters at time $t = 0$:

(1) the virial coefficient

$$k = T/|U| \tag{8}$$

and

(2) the velocity ratio

$$\tan\varphi = \dot{r}/\dot{\rho}. \tag{9}$$

The initial positions and velocities are determined in terms of k and φ using the formulas

$$r = \rho = \frac{2m_0(m_1+m_0)+m_1m_2}{2}(1-k) \tag{10}$$
$$= \frac{2(\varepsilon_1+\varepsilon_2)+\varepsilon_1\varepsilon_2}{2}(1-k),$$

$$\dot{r} = q\sin\varphi, \tag{11}$$

$$\dot{\rho} = q\cos\varphi, \tag{12}$$

where

$$q = \sqrt{\frac{2kM}{(1-k)\left[m_1(m_0+m_2)\sin^2\varphi + 2m_1m_2\sin\varphi\cos\varphi + m_2(m_0+m_1)\cos^2\varphi\right]}} \tag{13}$$
$$= \sqrt{\frac{2kM}{(1-k)\left[\varepsilon_1\sin^2\varphi + \varepsilon_2\cos^2\varphi + \varepsilon_1\varepsilon_2(\sin\varphi+\cos\varphi)^2\right]}}.$$

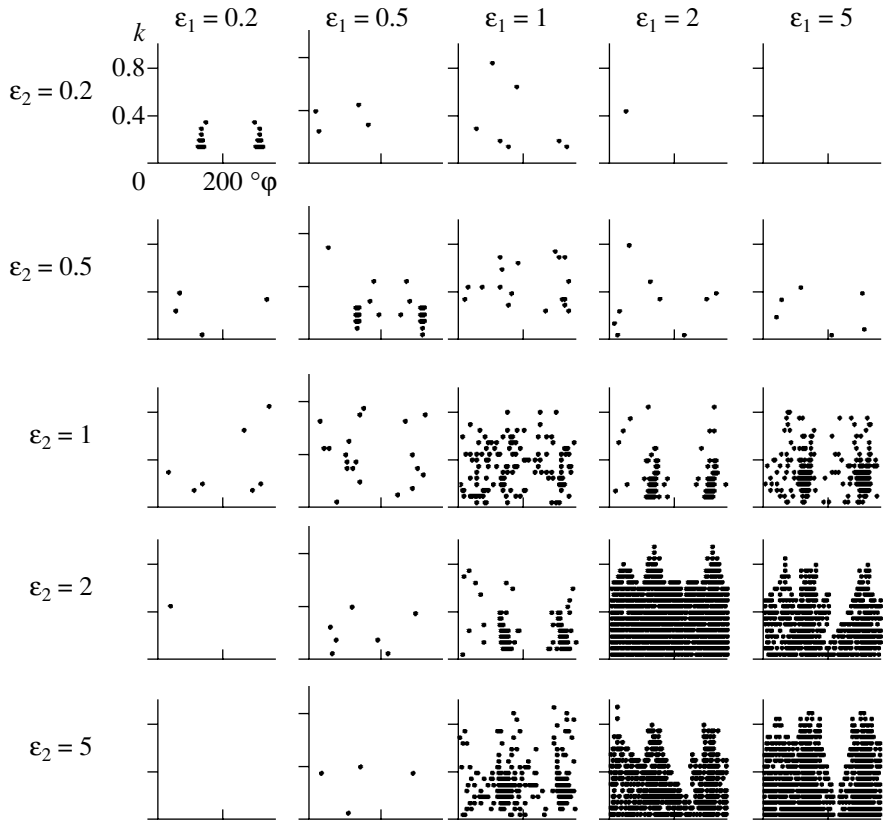

Fig. 6. Initial-condition domains corresponding to long-lived triple systems. The coordinates are the same as in Fig. 1.

The parameters k and φ vary in the intervals $k \in [0, 1]$, $\varphi \in [0, 2\pi]$. We analyze the set of mass ratios

$$\varepsilon_1, \varepsilon_2 = \{0.2, 0.5, 1, 2, 5\}. \quad (14)$$

For each pair $(\varepsilon_1, \varepsilon_2)$, we chose a grid of the parameters k and φ:

$$k = \{0.05(0.05)0.95\}, \quad (15)$$

$$\varphi = \{5^\circ(5^\circ)360^\circ\}. \quad (16)$$

For each version of the initial conditions $(\varepsilon_1, \varepsilon_2, k, \varphi)$, we computed the evolution of the system until one of the following three conditions was satisfied:

(1) one of the outer bodies escaped from the system according to the criterion of Yoshida [13] and Marchal [14];

(2) there was a "conditional" escape—the ejection of one of the outer bodies to a distance $R > 100$ units from the center of mass of the remaining pair;

(3) the system evolves for more than $t > 1000$ time units.

In addition, in the case $\varepsilon_1 = \varepsilon_2$, we fixed the lines of the triple collisions at $\varphi = \{45^\circ, 225^\circ\}$. Note that triple systems with $t > 1000$ can include both stable quasiperiodic orbits and unstable systems that will disrupt at a later time.

3. RESULTS OF STATISTICAL MODELING

The results of the numerical simulations enable us to classify the trajectories according to the number n of passages of the central body through the center of mass of the triple system preceding the disruption or "conditional" disruption of the system. We identified zones corresponding to $n = \{1, 2, 3, 4, 5\}$ in the domain of the initial conditions (φ, k). These zones are shaded black in Figs. 1–5. We can see the "antisymmetry" of the zones about the lines $\varphi = 45^\circ$ and $\varphi = 225^\circ$ if we replace ε_1 with ε_2 and also the symmetry about these same lines if the outer bodies have equal masses. Let us now analyze how the form of these zones changes as a function of ε_1 and ε_2.

When $n = 1$, two zones of initial conditions separated by the $\varphi = 45^\circ$ line can be seen. The first zone is located at the intersection of the two intervals $\varphi \in [0, 45^\circ] \cup [225^\circ, 360^\circ]$, while the second zone is located in the interval $\varphi = [45^\circ, 225^\circ]$. As ε_1 increases, the first zone becomes larger and the second zone smaller. Along the diagonal $\varepsilon_1 = \varepsilon_2$, the area of these zones decreases somewhat as the masses of the outer bodies increase.

When $n = 2$, there are two zones for some values $(\varepsilon_1, \varepsilon_2)$ and three zones for others. There is no third

zone for $\varepsilon_1 = \varepsilon_2$ or for high ratios of the masses of the outer bodies. The size of the zones increases with the ratio of the masses of the outer bodies. The area of the central of the three zones decreases with increasing ε_2, i.e., with increasing mass of the right outer body, while the area of the right-hand zone increases.

When $n \geqslant 3$, sets of "scattered" points emerge along with continuous zones. When $n = 3$, the area of the continuous zones decreases as we move downward along the $\varepsilon_1 = \varepsilon_2$ diagonal, i.e., with increasing masses for both outer bodies. Note that, when $\varepsilon_1 \geqslant 1, \varepsilon_2 \geqslant 1$, the continuous domains are located at $k > 0.5$, whereas they reach $k = 0.05$ for other ε_1 and ε_2 values.

When $n = 4$, the areas of the continuous zones increase as the difference of the masses of the outer bodies increases. Along the main diagonal, the area of the continuous zones is greater when the masses of the bodies are comparable. In the case of small masses for the outer bodies, the fraction of "scattered" points increases.

When $n = 5$, as a rule, the continuous domains extend along approximately vertical structures. Sets of "scattered" points symmetrically placed about the triple-collision line are found predominantly along the main diagonal.

Figure 6 shows the domains of initial conditions (φ, k) corresponding to the trajectories that did not disrupt during 1000 time units. The number of such systems increases with increasing masses of both outer bodies. The evolution of most of these systems will probably end in the escape of one of the outer bodies after some time. The continuous domains placed symmetrically about the $\varphi = 45°$ and $\varphi = 225°$ lines are concentrated toward the limiting points corresponding to stable central periodic orbits.

The results are summarized in table, which gives the fractions of the initial conditions that result in the escape of one of the outer bodies after some number $n = \{1, 2, 3, 4, 5\}$ of passages of the central body through the center of mass of the triple system. Also given are the total fractions of versions with $n = 1$–5 and the fraction of trajectories that did not disrupt during a time $t = 1000$. As expected, the results are symmetric about the $\varepsilon_1 = \varepsilon_2$ diagonal. This symmetry provides an additional verification of the correctness of the results of numerical simulations. On average, the total fraction of systems that disrupt when $n = 1$–5 decreases as the masses of the two outer bodies simultaneously increase and increases as the mass ratio of these bodies increases. Note that the fraction of escapes after one passage ($n = 1$) depends only weakly on $(\varepsilon_1, \varepsilon_2)$ and lies in the interval from 10% to 16%. The maximum fraction of escapes is achieved for $n = 3$ or $n = 4$ passages.

Let us now analyze how the escape fractions depend on ε_2 for fixed $\varepsilon_1 = 1$. The escape fractions after $n = 1$ and $n = 3$ passages decrease monotonically with increasing ε_2. The escape fractions for $n = \{2, 4, 5\}$ passages reach a maximum in the case of equal masses ($\varepsilon_1 = \varepsilon_2 = 1$). The fraction of undisrupted systems increases and the total fraction of systems with $n = 1$–5 decreases with ε_2. This increase is due to two effects:

(1) the increase in the size of the stability domain around the von Schubart orbit (the area of this domain reaches its maximum when $\varepsilon_1 = \varepsilon_2 = 1$);

(2) the increase in the fraction of unstable systems with lifetimes $t > 1000$.

The superposition of these two effects results in the emergence of a second maximum when all three bodies have equal masses.

Let us now consider the analogous dependences for $\varepsilon_1 = 0.2$ and $\varepsilon_1 = 5$. The corresponding fractions depend fairly weakly on ε_2 when $\varepsilon_1 = 0.2$, except for the case of escapes after $n = 4$ passages. When $\varepsilon_1 = 5$, the average fraction of escapes after $n = \{1, 2, 3, 4\}$ passages decreases. This is due to the increase in the fraction of undisrupted systems.

The dependences of the fractions of escapes and undisrupted systems for the case of equal outer masses ($\varepsilon_1 = \varepsilon_2$) are characterized by the decrease, on average, in the escape fractions and the increase in the fraction of undisrupted systems with increasing $\varepsilon_1 = \varepsilon_2$.

Note that our results for the equal-mass and $n = 1$ cases agree with those of Tanikawa and Mikkola [8, 9], taking into account the fact that we used other parameters when specifying the initial conditions. A more detailed comparison of the results is difficult, since Tanikawa and Mikkola analyzed sequences of double collisions and we have described the evolution of triple systems as a function of the number of passages of the central body through the barycenter of the system.

4. CONCLUSIONS

We have analyzed the dynamical evolution of triple systems with components with unequal masses lying along a straight line—the rectilinear three-body problem. We have classified the types of motions as a function of the number of passages through the center of the triple system for various ratios of the masses of the outer bodies to that of the central body.

The set of initial conditions for fixed mass ratios has the form of a two-dimensional bounded manifold. Continuous domains and sets of "scattered" points corresponding to escapes after n passages are identified on this set. Exclusively continuous sets exist

for $n \leqslant 2$, whereas sets of "scattered" points appear along with continuous sets when $n \geqslant 3$.

The topology and areas of continuous domains depend on the ratios of the body masses. It is of interest to determine in the future analytical formulas for the boundaries of the continuous domains identified, and to describe the physical mechanisms determining the classification of the orbits described here.

Note that the rectilinear three-body problem analyzed here is not only of mathematical interest but can also be used in analyses of the dynamics of young non-hierarchical triple star systems whose components move in very elongated orbits. Moreover, long-lived trajectories in the general three-body problem can behave like stable periodic orbits in some time intervals, in particular, they can behave like the von Schubart orbit.

5. ACKNOWLEDGMENTS

We are grateful to V.G. Surdin for a number of valuable comments on the first version of the paper.

REFERENCES

1. J. Chazy, Bull. Soc. Math. Fr. **55**, 222 (1927).
2. J. von Schubart, Astron. Nachr. **283**, 17 (1956).
3. R. Mc Gehee, Invent. Math. **27**, 191 (1974).
4. M. Hènon, Celest. Mech. **15**, 243 (1977).
5. R. Broucke and D. E. Walker, Celest. Mech. **15**, 243 (1980).
6. J. Yoshida, in *The Few Body Problem,* Ed. by M. J. Valtonen (Kluwer, Dordrecht, 1988), p. 77.
7. J. Hietarinta and S. Mikkola, Chaos **3**, 183 (1993).
8. K. Tanikawa and S. Mikkola, Celest. Mech. Dyn. Astron. **76**, 23 (2000).
9. K. Tanikawa and S. Mikkola, Chaos **10**, 649 (2000).
10. V. M. Alekseev, Usp. Mat. Nauk **36**, 161 (1981).
11. C. Robinson, *Dynamical Systems* (CRC Press, Boca Raton, 1995).
12. V. M. Alekseev, *Lectures on Celestial Mechanics* (NITs "Regulyarnaya i Khaoticheskaya Dinamika," Izhevsk, 2001).
13. J. Yoshida, Publ. Astron. Soc. Jpn. **24**, 391 (1972).
14. C. Marchal, Celest. Mech. **9**, 381 (1974).

Translated by A. Dambis